University of Texas Rio Grande Valley

ScholarWorks @ UTRGV

Theses and Dissertations - UTB/UTPA

5-2014

Nanostructured Transition Metal Oxides for Energy Storage and Conversion

Qiang Li
University of Texas-Pan American

Follow this and additional works at: https://scholarworks.utrgv.edu/leg_etd

Part of the Mechanical Engineering Commons

NANOSTRUCTURED TRANSITION METAL OXIDES

FOR ENERGY STORAGE AND CONVERSION

A Thesis

by

QIANG LI

Submitted to the Graduate School of
The University of Texas-Pan American
In partial fulfillment of the requirements for the degree of

MASTER OF SCIENCE

May 2014

Major Subject: Mechanical Engineering

NANOSTRUCTURED TRANSITION METAL OXIDES

FOR ENERGY STORAGE AND CONVERSION

A Thesis
by
QIANG LI

COMMITTEE MEMBERS

Dr. Karen Lozano
Chair of Committee

Dr. Yuanbing Mao
Co-chair of Committee

Dr. Dorina Mihut
Committee Member

Dr. Horacio Vasquez
Committee Member

May 2014

ABSTRACT

Qiang Li, <u>Nanostructured Transition Metal Oxides for Energy Storage and Conversion</u>. Master of Science (MS), May, 2014, 109 pp, 33 figures, references, 196 titles.

The conventional film configuration of electrochemical electrodes hardly fulfills the high energy and efficiency requirements because heavy electroactive material deposition restricts ion diffusion path, and lowers power density and fault tolerance. In this thesis, I demonstrate that novel nanoarchitectured transition metal oxides (TMOs), *e.g.* MnO_2, V_2O_5, and ZnO, and their relevant nanocomposites were designed, fabricated and assembled into devices to deliver superior electrochemical performances such as high energy and power densities, and rate capacity. These improvements could be attributed to the significant enhancement of surface area, shortened ion diffusion distances and facile penetration of electrolyte solution into open structures of networks. The utilization of Forcespinning®, a newly developed nanofiber processing technology, for large-scale energy storage and conversion applications is emphasized. This process facilitates the contradiction between the micro-batch production and the ease of large-scale manufacturing.

Key Words: Transition metal oxides, energy storage and conversion, Forcespinning®, pseudocapacitance domination, high rate capacity

DEDICATION

I dedicate my master thesis to my austere parents, Mr. Yongzhi Li and Ms. Zhisu Wang. I have not words to express my gratitude for their encouragement, motivation, guidance, education as well as their sacrifice of separating from their only son to allow me to pursue my own career. The completion of my master studies would not have been possible without the love and understanding from my family. I also would like to dedicate my thesis to my loving wife, Xing Sun, and I deeply appreciate her company and technical assistance in my research.

ACKNOWLEDGMENTS

TABLE OF CONTENTS

LIST OF FIGURES

CHAPTER I

INTRODUCTION

1.1 Statement of the Problem

It has been a new era since green sources of energy and energy storage have been exploited given that fossil fuels are expected to be depleted soon. The overconsumption of fossil fuels has become the major source of current environmental problems. Also, the ever-increasing developments of portable electronics, hybrid vehicles and large size industrial equipments require the rapid advancement of systems that could supply needed power. Lithium-ion batteries, fuel cells, supercapacitors and photovoltaic devices are heavily being studied. The contradiction of the tradeoff between power and energy densities restrains the commercial advanced energy storage. The challenge derives from the fact that an electrochemical device with a high energy density usually has a relatively low power density, and a device with a high power density usually has a relatively low energy density. For instance, batteries and fuel cells possess low power density, whereas supercapacitors deliver relatively low energy density (Figure 1.1). Among the alternative systems for energy storage/conversion devices, supercapacitors, also known as ultracapacitors, have attracted intensive attention owing to their high power density, long stability and rapid charge-discharge rates.[1-2] The mechanism of traditional electrical double-layer capacitors (EDLCs) counts on high-surface-area carbon-based structures to store energy through electrostatic adsorption of ions.[3-6] However, the energy density of EDLCs is far from satisfactory without the addition of other electrochemically reversible components due to their

limited specific capacitance. In contrast, pseudocapacitors employing rapid and reversible redox reactions on the surface or near surface of electrode materials exhibit much better electrochemical performances, such as higher specific capacitance and larger energy density.[7-10]
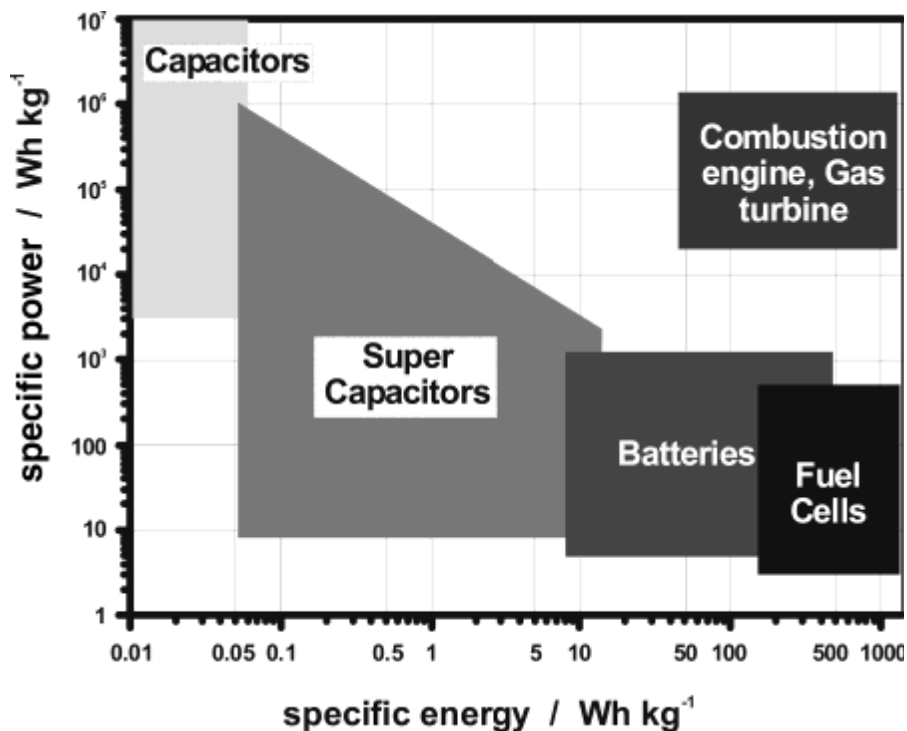
Figure 1.1 Ragone plot of the energy storage domains for the various electrochemical energy conversion systems.[11]

In the past decade, many pseudocapacitive transition metal oxides (TMOs), predominantly MnO_2,[12-14] V_2O_5,[15] Co_3O_4,[10, 16] NiO,[17-18] PbO_2,[19-20] Fe_2O_3,[21-22] RuO_2,[23-24] IrO_2[25-26] and WO_3,[27-29] nanostructures have been deemed to be tunable building blocks for constructing promising pseudocapacitors to fill the gap between lithium-ion batteries and supercapacitors. However, in terms of the pseudocapacitive materials, the poor electrical conductivity has severely prohibited its broad applications in energy storage.[30] Consequently, various hybridization strategies have been exploited to address the aforementioned issues. By

hybridizing with carbon nanotubes (CNTs),[31-33] graphene,[6, 8, 34] carbon paper/cloth[35-38] or graphitic carbon spheres,[39-40] the mechanical stability and ionic, electronic conductivity of the nanocomposites are greatly enhanced. Moreover, these nanostructured hybrids with carbon as backbones establish good charge transport channels to current collectors.
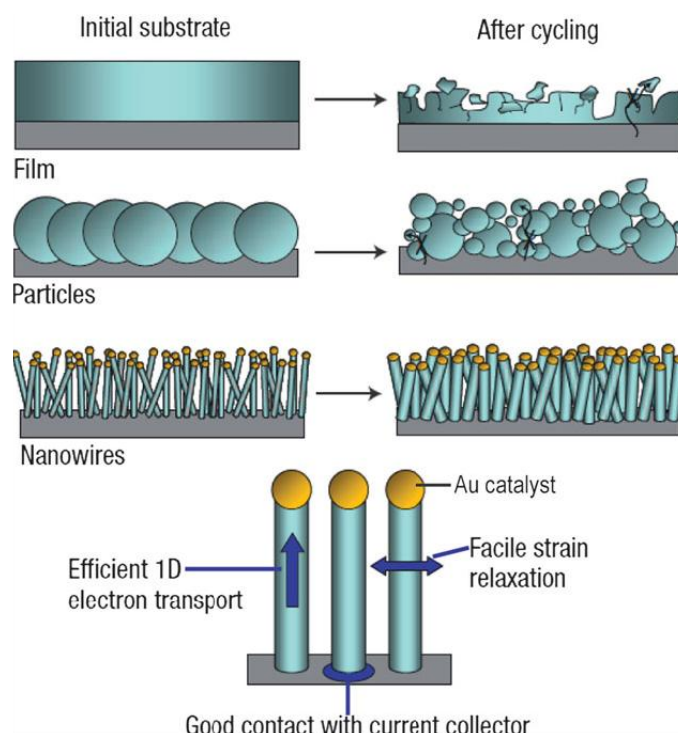
Figure 1.2 Schematic illustration showing the influence of different silicon morphologies on the integrity of electrode during alkali ion intercalation.[41]

To synthesize pseudocapacitive materials into nano-size is effective to shorten electrolyte ion diffusion distances and thus conduct thorough interfacial electrochemistry. In contrast with spherical nanostructures, *i.e.* nanoparticles, one-dimensional (1-D) nanostructures possess endurance on volume expansion and network structure for excellent electrolyte penetration (Figure 1.2), so the development of coaxial nanowires/fibers is of high importance. 1-D MnO_2 nanocomposites are taken as examples: Ye Hou *et al*. hanged MnO_2 nanospheres on

CNTs hierarchically via ultrasonic irradiation;[32] Liangbing Hu *et al*. employed electrodeposition to coat MnO_2 nanoflowers conformally on CNT-enabling conducting textile mats;[35] and Sang-Bok Ma *et al*. grew Birnessite MnO_2 nanoflakes on CNTs through hydrothermal process.[42] However, the electrochemical cyclic stability of these of carbon/MnO_2 hybrids still remains a tremendous challenge: (i) ionic and electronic diffusion are uncontrolled due to large particle sizes of active materials formed from fast growth processes among domains and on the interfaces between active materials and conductive carbon additives; (ii) active materials are exposed to electrolyte, which leads to undesired electrode/electrolyte reactions and fast dissolutions;[12] and (iii) adjacent nanostructures without buffer zones between them are prone to aggregate or pulverize and consequently flake off carbon backbone. Even though MnO_2 nanoparticle-enriched conductive poly(3,4-ethylenedioxythioxythiophene) (PEDOT) polymers have been synthesized recently,[43] these electrodes still suffer from mechanical instability and poor recyclability due to the coherent weakness of conductive polymers.[30, 44] Furthermore, an insulating binder, *i.e.* polyvinylidene fluoride (PVDF) or polytetrafluoroethylene (PTFE), is necessary to fabricate electrodes, and decrease the electrical conductivity and volumetric performance of Li-ion battery and supercapacitor electrodes. Other than the to-be-further-enhanced electrochemical performance, the previous fabrication procedures of nanocomposites are generally tedious and not cost effective. Moreover, the micro-batch production of nano/micro-scale electroactive materials literally contradicts the ease of manufacturing.

In addition to preparations of 1-D nanocomposites for enhancements of electrochemical performance, it has been noticed that the simple utilization of pseudocapacitive materials does not necessarily improve deliveries of the energy and power densities. The corresponding devices, *i.e.* asymmetric supercapacitors, coupled with carbon-based materials, such as activated carbon,

carbon nanotubes, conducting polymers and graphene, as anode materials, are prone to comply with electrical double-layer storage mechanism so that their electrochemical performance could not be optimized to fill the unmet high requirements of energy and power densities. We anticipate that it will be a new field if we allow the devices to be dominated by pseudocapacitance storage mechanism by smartly choosing electrode materials and triggering spontaneous alkali ion intercalation and deintercalation into and out of novel layered structures of pseudocapacitive materials.

1.2 Motivation

To produce 1-D nano/microfibers, electrospinning technology was firstly discovered by Morton and Cooley in 1902 and subsequently Formhals obtained nine US patents. The apparatus is capable of producing polymer or its composites' filament by making use of the electrostatic repulsions between the spinning solution and collector. Even though the electrospinning technology has been developed at breakneck speed after 1990s, which is reflected by a great number of relevant scientific articles and patents, it did not realize the critical application potentials and the goal of manufacturing fibers owing to its intrinsic technical limitations. Recently, Forcespinning® (FS) technology, which was developed by Lozano *et al*, demonstrates the opportunity of high production rate of fine nano/microfibers. The FS adopts high-speed rotational force to drive viscous fluid through orifices and thus produce fine fibers in a large scale, provided that the capillary force is exceeded by the centrifugal force and hydrostatic pressure (Figure 1.3). The operation of FS is free of complex controlling parameters, such as high electrical field strength, intrinsic solution/melt conductivity, electrostatic and ionization

fields, that affect Taylor cone and jet instability of conventional electrospinning processes. Its unique demonstration of capability as a high-yield manufacturing technology of nano/microfiber production will relieve the contradiction of advanced 1-D nanomaterials and industrial demands, eventually benefitting a variety of fields, especially energy storage and conversion.
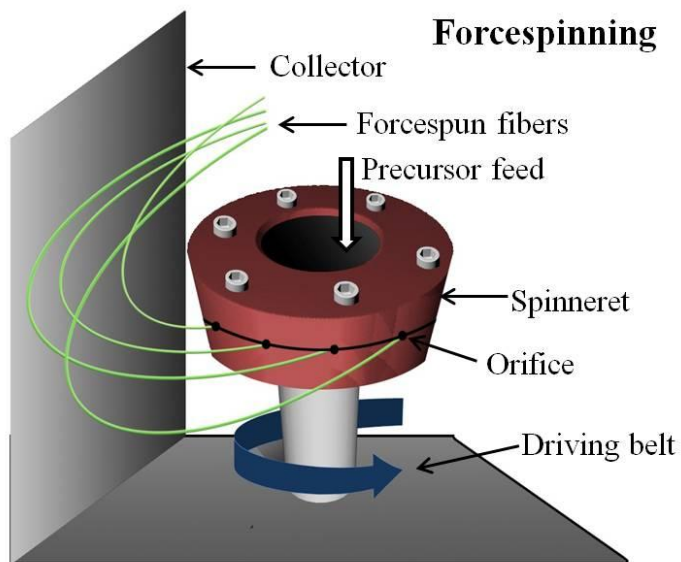
Figure 1.3 Schematic illustration of the Forcespinning setup and process.[45]

Nanocomposite fibers comprised of nanoscale inorganic fillers and polymer carrier can integrate both the merits of the polymers, like lightweight, flexibility and nice moldability, and of the inorganic nanofillers, like semiconducting properties, chemical resistance, thermal stability, high strength. The combination of advantages makes the nanocomposite fibers superior candidates with unpredictable mechanical reinforcement, electrochemical, electrical, optical, magnetic, thermal properties for multifunctional applications, such as multifunctional membranes, photocatalysts, chemical sensors, nanoelectronics, and electrochemical devices. The nanocomposite fibers can be fabricated through either the insertion of inorganic nanoparticles into polymer matrix or the calcination thermal treatment on polymer/metal salt precursor

composite fibers for conversion to functional counterparts. Worth mentioning is that the FS process is capable of spinning highly viscous fluid into fine fibers and consequently the rich polymer carrier results in interesting difference of inward and outward metal ion diffusion rates, which generates desired heterogeneous structures. The facile fabrication of nanocomposite fibers significantly simplifies the conventional tedious hybridization procedures that have been adopted to prepare heterogeneous nanostructures. More importantly, the as-prepared nanocomposite fibers imply other characteristics that favor the overall electrochemical performances and they could be produced in a large scale to meet the demands of markets for advanced electrochemical nanomaterials.

In this thesis, the heterogeneous nanocomposite fibers or other 1-D nanocomposite nanostructures using FS processes followed by thermal treatment or all solution-phase synthesis were prepared and expected to display superior electrochemical performance because of high surface area, heavy electroactive material loading and electrolyte solution penetration with no kinetic limitations. The 1-D nanostructures are expected to be upgraded to three-dimensional (3-D) nanostructures to further increase the accessible surface area and be utilized in different applications besides lithium-ion batteries and pseudocapacitors, *i.e.* photovoltaic devices.

1.3 Research Objectives

The first system presented in this thesis is heterogeneous MnOx-encased carbon nanocomposite fibers. We report the fabrication of heterogeneous MnO nanocrystal (NC)-encased hierarchical carbon nanocomposite fibers (MCNFs) via a novel and large-scale FS followed by low temperature carbonization. Manganese nitrate containing polyvinylpyrrolidone

7

(PVP) polymeric fibers were carbonized at relatively low temperature, *i.e.* 500 ℃, due to oxidant Mn^{2+} cations. Different inward and outward ionic diffusion rates of Mn^{2+} cations concurrently resulted in congregation of MnO NCs near the surface of the nanocomposites during thermolysis. After anodic and cyclic voltammetric electrochemical oxidations, in situ phase transformation from electrochemically inactive MnO NCs to pseudocapacitive MnO_x counterparts occurs. This yields a MnO_x NC/carbon hybrid fiber network with MnO_x NC-enriched functional surface. These NCs are accessible to aqueous electrolyte ions for Faradic redox reactions. Therefore these unique nanocomposites demonstrate a promising potential as pseudocapacitive electrode materials.

The second system presented in this thesis is development of VO_x/polymer nanohybrid fibers. A large-scale production process composed of the FS technology followed by relatively low-temperature calcination (450 ℃) was developed to produce flexible/bendable energy storage materials of heterogeneous vanadium oxide/polyvinylpyrrolidone derivative nanofibers with bark-like topography. This process overcomes the low fabrication-efficiency and cost-performance shortcomings of previous techniques, such as tedious synthesis and high carbonization/growth temperature. The mechanical flexibility from moderately cross-linked polymeric backbones and the mixed valence-induced high electronic conductivity $(4.48 \times 10^4 \, S \, m^{-1})$ from vanadium oxide concurrently endow these nanohybrid fibers as high performance flexible electrode materials for lithium-ion batteries.

The third system presented in this thesis is 3-D $ZnO@MnO_2$ core@shell nanostructures. Three-dimensional (3-D) $ZnO@MnO_2$ core@shell branched nanowire arrays exhibit five times higher areal capacitance, better rate performance and smaller inner resistance than their nanowire

array counterparts. These novel 3-D architectures offer promising designs for powering microelectronics and other autonomous devices on exceptionally small geometric scales.

The fourth system presented in this thesis is development of asymmetric supercapacitors based on MnO_2 nanoflowers. Unique MnO_2 nanoflowers (~25 nm) composed of ultrathin $K_{0.26}MnO_2$ nanoflake assemblies were synthesized by a facile and green process. Prototype MnO_2-NFs//KCl//CNTs asymmetric supercapacitors in neutral aqueous electrolyte demonstrated pseudocapacitive dominance in addition to outstanding energy and power densities and superior cycling performance.

The fifth system presented in this thesis is 3-D caterpillar-like ZnO nanostructures. We report a rational and facile synthesis of hierarchical branched ZnO nanostructures (BZNs) by combining novel FS technology and hydrothermal process on a large-scale. The ZnO nanofibers that derived from forcespun polyvinylpyrrolidone/zinc nitrate hexahydrate composite fibers were first prepared by calcination at 500 ℃ and subsequently disposed on indium tin oxide-coated glass substrates, serving as nonwoven netlike seed sites from which ultra-dense and uniform nanowires (NWs) in an omnidirectional fashion originated hydrothermally. This work is developed, in efforts to replace conventional multistep seeding methods producing upstanding nanostructures, to yield high spatial occupancy of NWs and thus substantially promote the accessible surface area and roughness factor. The relevant BZN photoanodes showed a significant enhancement of photo-to-hydrogen conversion efficiency.

CHAPTER II

HETEROGENEOUS MANGANESE OXIDE/CARBON NANOCOMPOSITE FIBERS FOR

HIGH PERFORMANCE PSEUDOCAPACITORS

2.1 Introduction

The integration of transition metal oxide nanocrystals (TMONCs) and one-dimensional

(1-D) carbon based skeletons has been exploited for various applications, such as chemical

sensors,[46-47] catalysis,[48] nanoelectronics[49] and electrochemical devices.[37, 43, 50] In view of the

united advantages of functionality of oxide nanocrystals and superior physical characteristics

including electrical conductivity, mechanical tolerance, thermal stability and surface area of

carbonaceous nanostructures, rationally constructing TMONC/carbon hybrids is prone to achieve

unprecedented physical and chemical features with respect to single component counterparts.[51-52]

Particularly for supercapacitor applications, two well-established synthetic strategies have been

widely carried out to fabricate 1-D TMONC/carbon hybrids: (1) pseudocapacitive TMONCs are

anchored onto conductive carbon-based backbones, such as single/multiple walled carbon

nanotubes, 1-D conducting polymers and carbon cloth, via a variety of approaches including

hydrothermal method,[42] electrochemical depositions,[37] atomic layer deposition,[53] precursor

hydrolysis,[54] and so forth;[43] and (2) 1-D TMO nanowires/nanoribbons with high aspect ratio are

surface-shielded by conducting polymers through monomer polymerizations.[50, 55] For the first

protocol, hybrid electrodes would suffer from inevitably uncontrolled ionic and electronic

diffusions due to fast growth of active oxides during anchoring, capacitance fading caused by unexpected reactions between electrode materials and electrolytes as well as dissolution of active materials into electrolyte solutions, and pulverization problem because of particle aggregation during charge and discharge cycles. On the other hand, the second protocol is unlikely to offer stable and fast paths for ionic diffusion and electronic transportation due to the intrinsic instability of conductive polymers and relatively large size of active materials. Even though in situ carbonation of electrospun hybrid polymeric fibers can incorporate nanocrystals into conducting carbon frameworks, the pseudocapacitive target oxides would be reduced into electrochemically inactive metal or metal oxides with lower oxidation states of transition metals during high temperature carbonations and the nature of homogeneously dispersed NCs in carbon matrix can deteriorate the rate capacity when limited electrolyte ion penetration depth is taken into consideration. Those are the primary reasons why carbonized hybrids have been explored mostly as anode materials with enhanced stability of lithium ion batteries.[56-58] Therefore, establishing an efficient, facile and productive path to fabricate Faradic TMONCs into carbon frameworks is still a tremendous challenge for excellent recyclability, high rate pseudocapacitors.

In this work, we present a novel strategy for heterogeneous MnO_x NCs/carbon nanocomposite fibers via high-yield FS followed by carbonization in inert atmosphere and combined with electrochemical oxidations by applying three-electrode configuration. Acting as an updated substitution of electrospinning, FS eliminates the necessity of taking solution/melt electrical conductivity, electrical field strength, surface charge and ionization field in account by simply employing high speed centrifugal force and thus significantly simplifies the fabrication process of fine nanofibers.[59-60] Moreover, the high production rate, ~1g/min, affords great

opportunities to introduce nano-scaled 1-D materials into commercial manufacturing in various areas. In this case, $Mn(NO_3)_2$/PVP fibers (MPFs) were spun onto current collectors directly without adding any polymer binder and conductive additive for the first time to form intercross
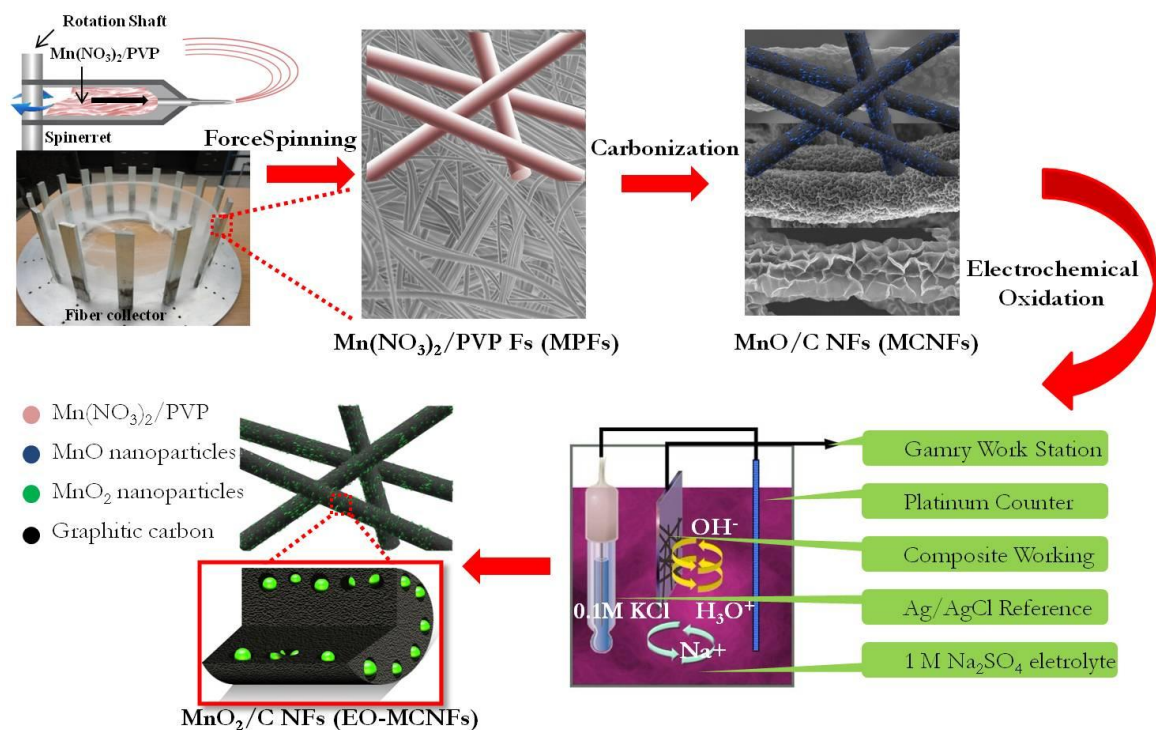
Figure 2.1 Schematic illustration showing the preparation process of MnO_x-encased carbon nanocomposite fibers.

networks for facile electrolyte penetration and boosted gravimetric capacitance. Subsequent calcinations led to chronologically uneven ionic diffusion of Mn^{2+} ions, thermolysis and carbonization for forming hierarchical hybrid fibers. These fibers consist of MnO NCs evenly distributed on the near surface regions but simultaneously shielded by conducting carbon. The MnO NC/carbon hybrid carrying electrodes were further phase transformed into pseudocapacitively promising MnOx NC/carbon hybrid fibers through anodic and cyclic voltammetric electrochemical oxidations (Figure 2.1).

2.2 Experimental

2.2.1 Materials

Polyvinylpyrrolidone (PVP, average MW = 130,000) and $Mn(NO_3)_2 \cdot xH_2O$ (99.99%, x = 4-6) were purchased from Sigma Aldrich. All reagents were of analytical grade and were used without further purification.

2.2.2 Preparation of MnO$_x$-encased carbon nanocomposite fibers

The $Mn(NO_3)_2 \cdot xH_2O$/PVP fibers (MPFs) were prepared as follow. PVP (3.7 g) was gradually dissolved into 8.7 mL of 10, 18.7, and 25.6 wt.% $Mn(NO_3)_2 \cdot xH_2O$ aqueous solution by using both vortex mixing and sonication in 2-hour intervals for at least 48 h for a homogeneous dissolution. The precursor solution was maintained statically in dark in a vacuum oven at room temperature overnight to remove possible trapped air bubbles. To make MPFs, the prepared spinning solutions were fed into proprietary designed spinneret with evenly separated eight needles around its periphery. These needles have 0.29 mm inner orifice size and are 13 mm long. FS was carried out at a rotational speed of 9,000 rpm for 30 s, a 6 cm needle-to-collector distance with aluminum foil as collectors. The production rate in a lab scale unit was >1 g min^{-1}. Moreover, titanium substrates (0.25 mm thick, Aldrich), which were degreased ultrasonically prior to collection in acetone and ethanol for 10 min, respectively, were directly applied as current collectors. To directly deposit MPFs onto Ti substrate, Ti foil cut into 2 × 0.5 cm was fastened onto alumina collectors with polytetrafluoroethylene (PTFE) tape prior to the FS process. The MPFs were then calcined at 500 ℃ for 3 h in argon atmosphere with a heating ramp rate of 2 ℃ min.

2.2.3 Characterization

Morphological and structural analyses of precursor MPFs, and corresponding calcined MnO/carbon nanocomposite fibers (MCNFs) and electrochemically oxidized MCNFs (EO-MCNFs) were carried out by scanning electron microscopy (SEM, Carl Zeiss Sigma VP Field-Emission, at 2-5 KV) equipped with scanning transmission electron microscopy (STEM), and transmission electron microscopy (TEM, JEOL JEM-2010UHR) coupled with selected area electron diffraction (SAED) and energy-dispersive X-ray spectroscopy (EDX). The charging effect during SEM imaging on precursor MPFs was eliminated by coating with an approximately 100 Å thick Au/Pd layer using a Denton Desk II TSC turbo-pumped sputter coater. There was no need to sputter coating of MCNFs and EO-MCNFs for SEM imaging. Fourier transform infrared (FTIR) spectra were recorded from 4000 to 450 cm^{-1} with a 4 cm^{-1} spectral resolution on a Thermal Nicolet Nexus 470 spectrometer with a DTGS detector by signal-averaging 32 scans. Differential scanning calorimetry (DSC) of the MPFs was run between 25 ℃ and 300 ℃ at a heating rate of 5 ℃ min^{-1} on a TA Instruments Q100 DSC in nitrogen environment. To estimate the weight losses and the amounts of manganese oxide for calculating the compositions of nanocomposites, Thermogravimetic Analysis (TGA) was performed from 25 ℃ to 800 ℃ at 5 ℃ min^{-1} on a TA Instruments Q500 Thermogravimetric Analyzer for the MPFs and corresponding calcined MCNFs in nitrogen and air fluxes, respectively. The structural information of the calcined MCNFs were determined by X-ray powder diffraction (XRD) on a Rigaku Miniflex II with Cu Kα radiation (λ = 1.5418 Å) between 5° and 80°. The powder X-ray diffraction analysis of the electrochemically oxidized EO-MCNF sample was carried out with a Bruker AXS D8 QUEST diffractometer with Cu Kα radiation (λ = 1.5406 Å) between 13° and

70°. The X-ray photoelectron spectroscopy (XPS) spectra were collected on a Kratos AXIS-165 XPS/AES instrument using monochromatic Al K radiation.

2.2.4 Electrochemical Evaluation

All the electrochemical measurements were also conducted using the Gamry reference 600 Potentiostat/Galvanostat/ZRA workstation combined with PWR 800 software suit. Cyclic voltammetry (CV) were performed at a potential window of 0 to 1.0 V (*vs.* Ag/AgCl) with scan rates ranging from 2 mV s^{-1} to 100 mV s^{-1}. Galvanostatic charge/discharge testing was conducted between 0 and 1.0 V (*vs.* Ag/AgCl) at current densities ranging from 0.2 to 1.0 A g^{-1}. Electrochemical impedance spectroscopy (EIS) measurements were performed under AC amplitude of 5 mV and frequency range of 500,000 to 0.001 Hz.

2.3 Results and Discussion

2.3.1 Morphology and Structure Characterization

Figure 2.2 shows the SEM images of MPFs with low and high magnifications. MPFs were successfully spun into interconnected networks with no beads exhibiting via the FS method for different manganese nitrate contents. Bead-free feature can improve gravimetric performances when subsequently MPFs thermally decompose and phase transform into pseudocapacitive nanohybrids. For convenience, these MPFs are denoted as MPF-1, MPF-2 and MPF-3 with the increasing concentration of manganese nitrate. With increasing ratio of manganese nitrate to PVP, the as-spun MPFs exhibit more wrinkled surfaces. Additionally, these relatively randomly oriented MPFs form an intercrossing network. The average diameters of

these MPFs vary from 400 nm to 1 μm for MPF-1, MPF-2 and MPF-3. According to previous FS studies, the fiber diameter is determined by multiple factors, such as spinning solution viscosity, solution surface tension, spinning rotational speed and spinneret needle to fiber collector distance.[59-60] Owing to the increases in $Mn(NO_3)_2 \cdot xH_2O$ concentrations, the precursor solution viscosity increases,
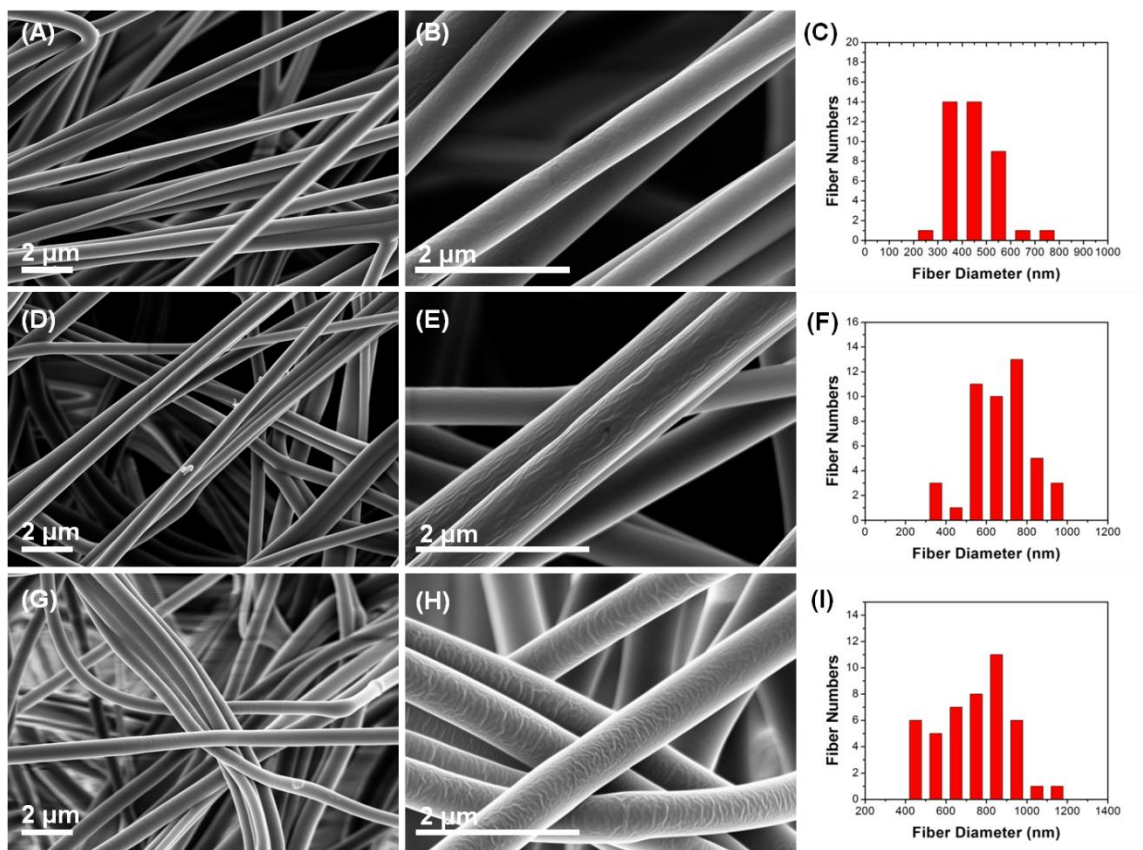
Figure 2.2 SEM images and diameter distributions of MPFs with different $Mn(NO_3)_2 \cdot xH_2O$ concentrations. (A, B, C) MPF-1, (D, E, F) MPF-2, and (G, H, I) MPF-3.

which is mainly responsible for the variations of diameters of the MPFs.[61-62] The rotational force and polymeric wettability are creatively utilized to cement MPFs onto current collectors without introducing any polymer binder for electrode fabrications. Particularly noteworthy is that

elimination of inactive binder and porous feature of network are critical to constructions of high

rate devices in energy storage.

Figure 2.3 shows the FTIR spectra from the three MPF samples. The sharp absorption

peak at 1383 cm^{-1} is attributed to N-O asymmetric stretching vibrations from NO^{3-} group.[63] Two

remarkable broad peaks originating from 3400 to 3480 cm^{-1} and from 1668 to 1630 cm^{-1}
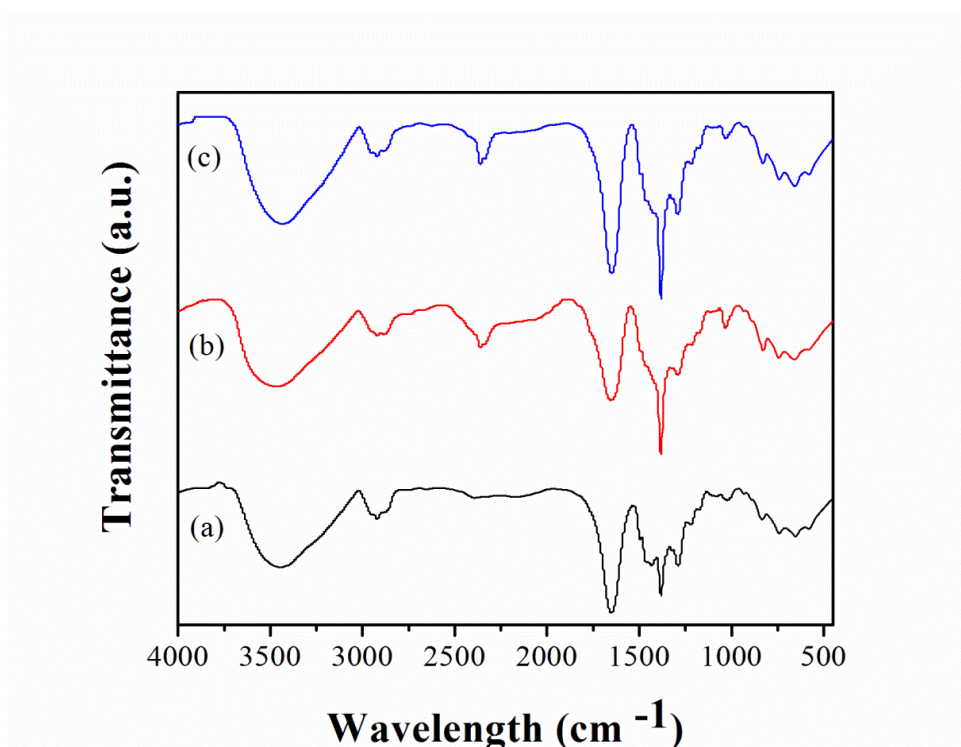
Figure 2.3 FTIR spectra of (a) MPF-1, (b) MPF-2, and (c) MPF-3.

correspond to O-H stretching and bending bands, respectively. They are derived from the

residual water solvent, the hydrate water from manganese nitrate and absorbed moisture on the

hygroscopic manganese nitrate and PVP. The fingerprint absorption modes of PVP are distinctly

identified with prominent peaks at about 1277-1294, 1321, 1424-1468, 1500 cm^{-1} and 2916-2960

cm^{-1}, which are assigned to N-C stretching of $N-CH_2$, $C-H_2$ wagging, $C-H_2$ scissoring, N-C

stretching of N-C=O, and symmetric C-H stretching, respectively.[64-65] The primary absorption mode at 1653 cm^{-1} corresponding to the carbonyl group C=O stretching vibration of PVP is probably superimposed with strong O-H bending vibration. The FTIR analyses indicate that the MPFs consist of nitrate anions and PVP polymer as well as water molecules. Along with the increasing manganese nitrate, the intensities of N-O stretching vibrations are apparently increased.
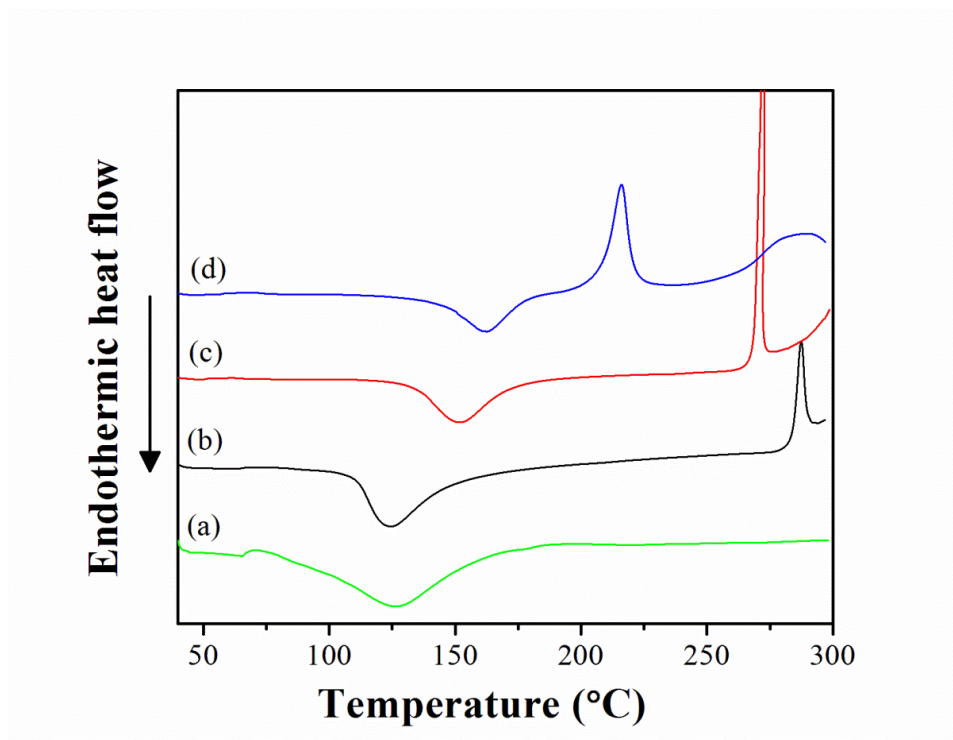
Figure 2.4 DSC thermograms of (a) pure PVP NFs, (b) MPF-1, (c) MPF-2, and (d) MPF-3 in nitrogen atmosphere.

Thermal experiments of the as-spun MPFs as well as PVP fibers were performed by DSC under nitrogen atmosphere, as showed in Figure 2.4. Each DSC thermogram from the three MPFs exhibits a distinct exothermic peak and an endothermic peak, even though the peak positions are shifting depending on different $Mn(NO_3)_2 \cdot xH_2O$ content. The endothermic peak

located in relatively low temperature region is associated with the dehydration of PVP in the MPFs.[66] The upshifted degradation temperature is presumably owing to increasing $Mn(NO_3)_2 \cdot xH_2O$ content as well as the interactions between $Mn(NO_3)_2 \cdot xH_2O$ and PVP.[67-69] The presence of manganese nitrate gives rise to steric hindrance to the mobility of polymeric PVP backbone. Coordination complexes formed through *van der* Waals forces, polar attraction and stabilization from *p*-bond overlap reduce the polymeric PVP flexibility and dehydration rate
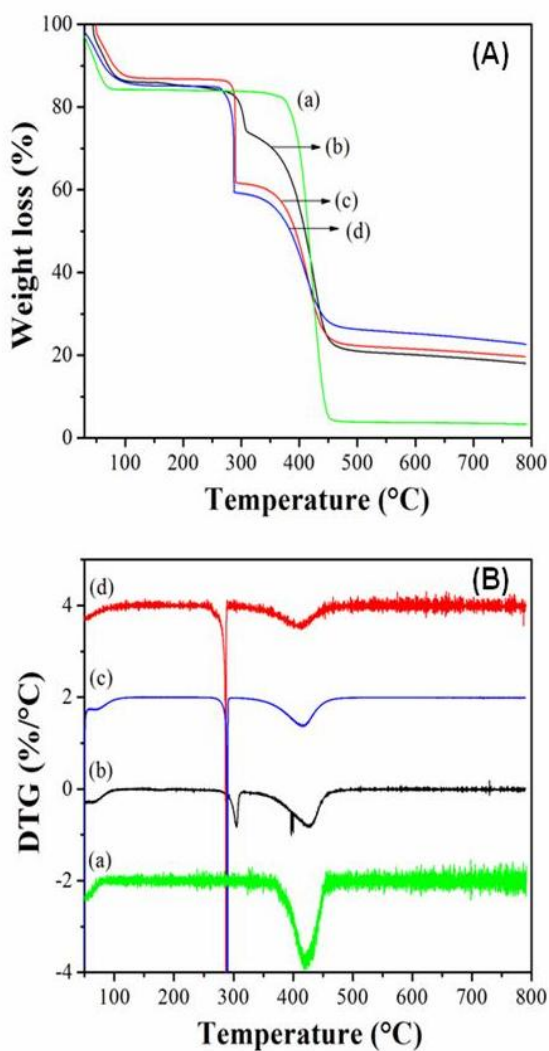
Figure 2.5 (A) TGA thermograms and (B) related DTG of (a) pure PVP fibers, (b) MPF-1, (c) MPF-2, and (d) MPF-3 in nitrogen atmosphere.

19

while improve its thermal stability in the lower temperature region. On the other hand, the exothermic peaks that appear in the region of 210-283 ℃ is downshifting with increasing $Mn(NO_3)_2 \cdot xH_2O$ content. According to the XPS study toward the residual product from PVP degradation at different temperatures by Chen *et al.*,[70] the exothermic peaks can be attributed to the breaking of the C-N bonds linking pyrrolidone rings to the polymeric backbone during the decomposition of PVP. The premature degradation of PVP as shown by the downshifted exothermic peak with increasing $Mn(NO_3)_2 \cdot xH_2O$ content possibly results from the interaction between Mn^{2+} ions and carbonyl groups of PVP. This interaction hinders the formation of free radicals and subsequently that of their intermolecular termination reactions and thus accelerates the degradation of PVP.[56] Furthermore, Mn^{2+} ions can act as an oxidant to lower the minimum oxidation temperature of PVP.[71-72] Similar behaviors have been reported in literatures from nanocomposites. In addition, the heat released from the decomposition of PVP in the MPF-2 is much sharper than that from the other two MPFs. As it is well-known, thermogram study can be interpreted to structural variations. The degradation of PVP contains multiple stages, such as chain scission, cross-linking, and side-chain cyclization. The intensified peak may be affected by complex combination of thermally exothermic processes.[56]

Figure 2.5A shows the TGA thermograms of the MPFs and PVP fibers under nitrogen atmosphere. The first weight loss occurring around 50-110 ℃ is attributed to the evaporation of physically adsorbed water molecules. After that, the thermal degradation curves of MPFs show two decays whereas pure PVP fibers show only one decay, which is in accordance with other observations.[73] The degradation with the onset of 250 ℃ correlates with the exothermic peaks in DSC curves and corresponds to the breakage of pyrrolidone pendant groups from the PVP backbone. The second weight drop stretching up to 480 ℃ is attributed to the degradation of the

20

main hydrocarbon chains of PVP. The differential of the weight loss (Figure 2.5B) highlights the two stages of PVP degradation more clearly. Interestingly no weight loss related to decomposition of anhydrous manganese nitrate from the MPNFs is distinguished in the range of 200-230 ℃ in DTG associated with DSC pattern, unlike thermal decomposition behavior of the pristine manganese nitrate. It is inferred that $Mn(NO_3)_2$ decomposition is postponed and occurs accompanying the degradation of the side chain of PVP due to the interaction between the manganese nitrate and PVP. The interaction may increase the activation energy of the formation of manganese oxide from manganese nitrate in PVP. The simultaneous degradation of manganese nitrate and PVP in the MPFs is supported by the fact that the decomposition percentage in the range of 263-315 ℃ increases proportionally with increasing the manganese nitrate content. Another interesting fact is that there is a slow but slight weight loss (~2 %) taking place after 480 ℃ from all three MPFs, in contrast to the pure PVP fibers. The decomposition of pure PVP completes at 480 ℃. Thereby, the 2 % weight loss after 480 ℃ is tentatively ascribed to the reduction of MnO_2, the direct decomposition product of $Mn(NO_3)_2$, to lower valent manganese oxide by surrounding reductive carbon or carbon-rich compounds generated during carbonization.[57] In addition, about 18.1, 19.7, 22.6 and 3.4 wt.% residuals are eventually present from the calcination to 800℃ in nitrogen of the MPF-1, -2, -3 and pure PVP fibers, respectively. The higher residual percentage from MPFs than that from pure PVP fibers indicates the formation of manganese oxide/carbon composites.

From SEM images shown in Figure 2.6, the diameter of the MCNFs does not shrink obviously from the MPFs in spite of ~80 wt.% weight loss during the calcinations. Canal-like patterns are present on the surface of the MCNFs and their surface roughness is gradually increasing with increasing MnO loading. Dark-field STEM images from individual MCNF
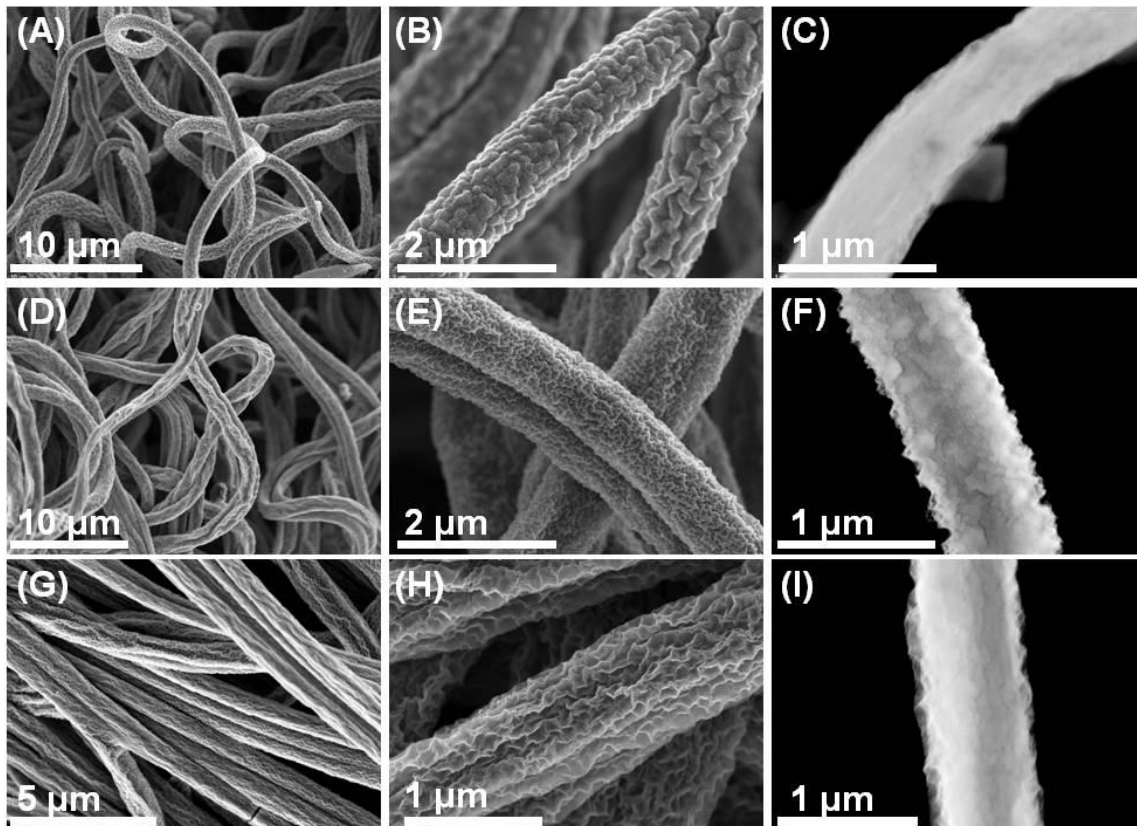
Figure 2.6 SEM images of MnO nanoparticle-encased carbon nanocomposite fibers with different MnO contents. (A, B) MCNF-1, (D, E) MCNF-2, and (G, H) MCNF-3. Corresponding dark-field STEM images are shown as (C) MCNF-1, (F) MCNF-2, and (I) MCNF-3.

(Figures 2.6C, F and I) demonstrate that MCNF-2 exhibits the most complicated zigzag-shaped canals on the surface. Such controllable hierarchical structure obtained by varying manganese salt loading in spinning precursor enables the nanocomposite fibers with high electrochemically active interfacial area with electrolytes, which improves pseudocapacitive redox reaction performance as demonstrated below.

MPFs are thermally transformed into heterogeneous MnO NC-encased carbon nanocomposite fibers through controlled calcinations outlined in the experimental section. Figure 5 displays morphological and structural information of the typical MCNF-2 sample initially
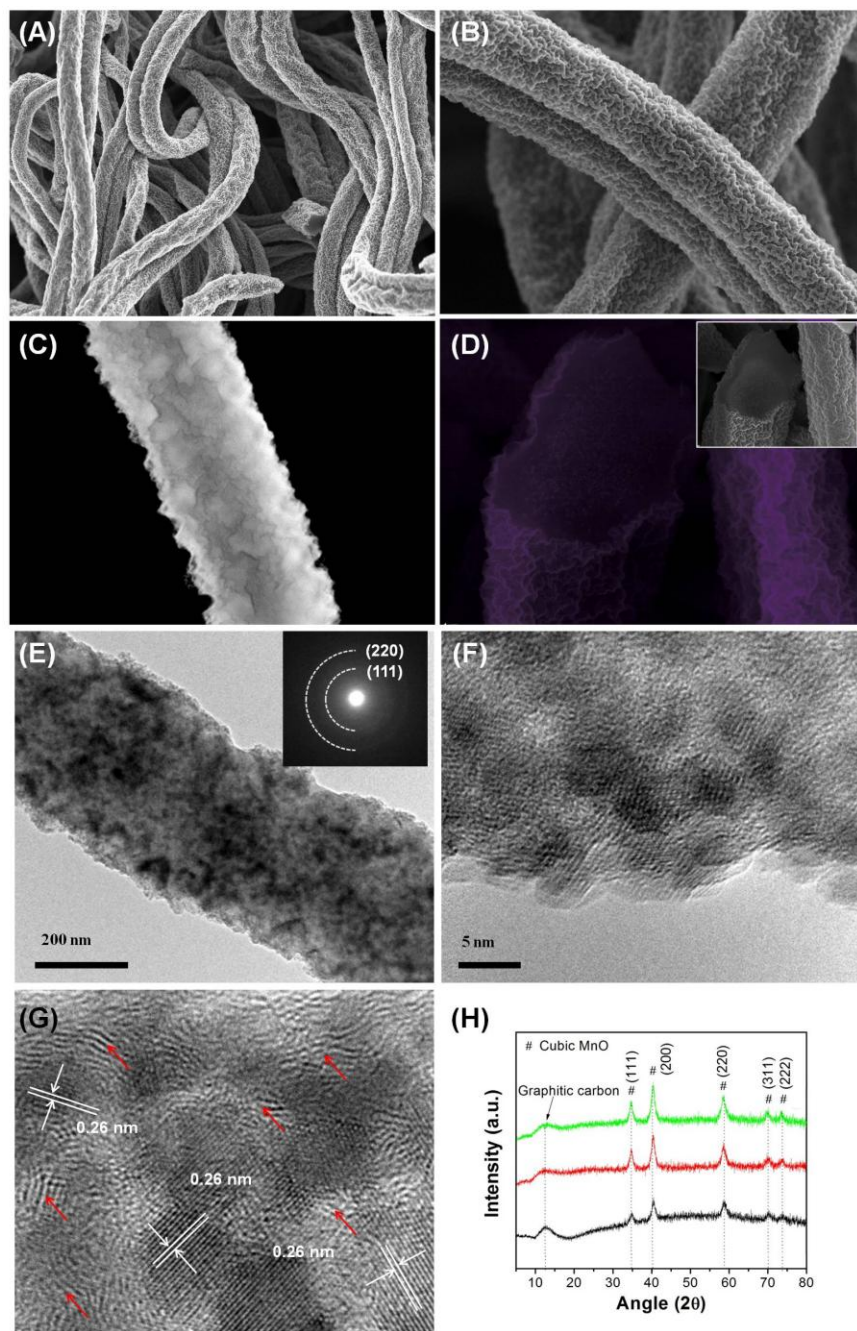
Figure 2.7 (A, B) Low- and high-magnification SEM images, (C) dark field STEM image, (D) BackScatter image with inset of corresponding InLens image, (E, F, G) TEM and HRTEM images with inset of related SAED pattern in (E), and (H) XRD pattern of MnO nanocrystal-encased carbon nanocomposite fibers (MCNF-2).

originating from MPF-2. Amazingly, the averaged diameter of MCNF-2 does not shrink apparently with respect to MPF-2 in spite of about 80 wt.% weight loss during the calcinations and this phenomenon is tentatively ascribed to formed carbon skeleton transformed from unprecedented heavily loaded polymer in FS recipe in contrast to electrospinning ingredients. Figure 2.7A&B show the micro/nanostructures of the nanocomposite fibers. The well-inherited intercrossing network of nanocomposites ensures great percolation of electrolyte and sufficient mechanical stability for volumetric expansion during battery-like pseudocapacitive TMOs performing. In the meanwhile, MCNFs exhibit undulate surface topography which is favorable to offer more accessible electrochemically active sites for Faradic redox reactions on the interface of electrolyte and electrode materials. The Figure 2.7D shows a cross-section image, taken under back-scatter detector, of an individual MCNF. Compared to lightweight carbon atoms, manganese with larger atomic number is chosen to be detected under backscattered electron imaging and apparently congregates on the surface or near surface regions of MCNFs,[74-75] unlike other homogeneous 1-D hybrids.[58, 76] The formation of heterogeneous structures with TMONC enriched surface is essential for high rate pseudocapacitors because it is widely accepted that the pseudocapacitive reactions only effectively occur in the first dozens of nanometers at high current densities.[2, 77] In other words, the utilization efficiency of pseudocapacitive materials in 1-D configuration will decrease along the radical direction from exterior surface to interior axis. Heterogeneous 1-D nanocomposites with active material-enriched surface or near surface utilize active materials most thoroughly. TEM studies of MCNF-2 were conducted to offer a further comprehension of structural features. In Figure 2.7E, F&G, the MCNFs display small, dark domains resulting from nanocrystals and relatively translucent carbon matrix, which indicates that the manganese oxide nanoparticles with about 10 nm size are evenly distributed and

24

incorporated into near surface terrains of carbon frameworks and shielded by the surrounding meandering-featured carbon.[58] The meandering-featured carbon is believed to possess a graphitic-like structure that formed in relatively low temperature carbonization due to Mn^{2+} as oxidant catalyzing the carbonation of polymer.[78-80] The carbon protection can prevent oxide domains from further growth during material synthesis and undesired aggregation during long term cycles of charge and discharge, which is one of key structural characteristics of these unique nanocomposites to overcome the devastating capacitance fading in current designs of pseudocapacitors. The XRD pattern in Figure 2.7H indicates that manganosite-type MnO (JCPDS card #75–0626; space group: $Fm\bar{3}m$ (225); a=4.4435 Å) is readily identified by the emergence of five characteristic peaks (2θ = 34.94, 40.58, 58.72, 70.20 and 73.82°), marked by their corresponding Miller indices ((111), (200), (220), (311), and (222)).[81] This result is further confirmed by two diffraction rings, ascribed to (111), and (220) planes of MnO, in SAED pattern and the well-resolved lattice fringes with an interplanar spacing of 0.26 nm of the (111) plane of cubic MnO in HRTEM image (Figure 2.7G). The broad peak centered at about 25° is assigned to amorphous or graphitic-like carbon.[78-80]

2.3.2 Electrochemical Oxidation

To electrochemically oxidize these MCNFs into EO-MCNFs, one cycle of anodic charge is first applied on the binder-free electrodes at a current density of 10 $\mu A\ cm^{-1}$ between -0.6 to 0.9 V for approximate 5,000 s, and then 1000 cycles of voltammetric scans with a potential window of 0 – 1 V (*vs.* Ag/AgCl) were conducted to achieve the electrochemical oxidation of MnO NPs into MnO_2 NPs in the carbon matrix.[82] These MCNFs also have excellent accommodation of strain caused by Na^+ intercalation/deintercalation, so process long stability as
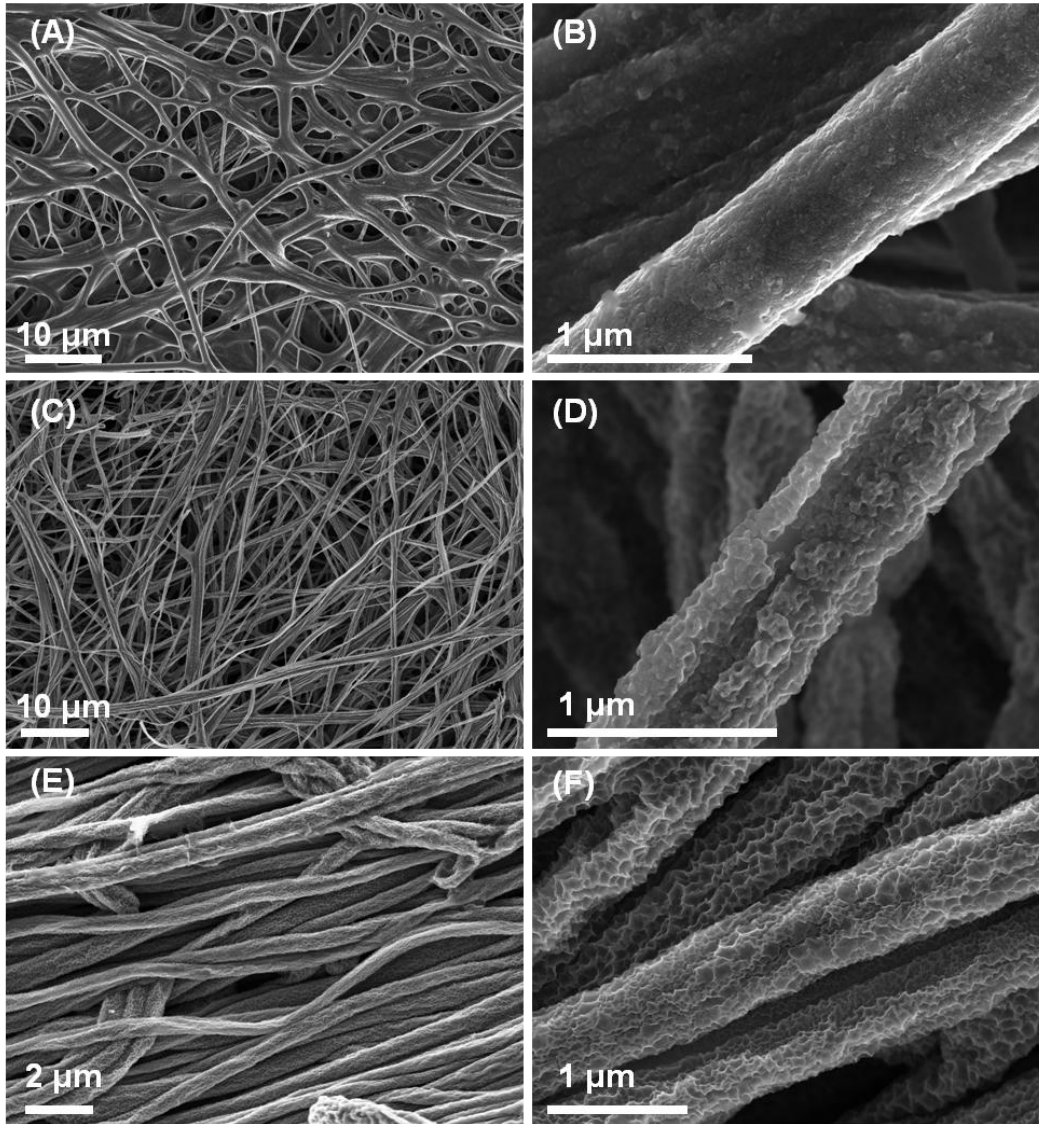
Figure 2.8 SEM images of MnO$_2$ nanoparticle-encased carbon nanocomposite fibers with different MnO$_2$ contents after anodic and 1000 cycles of voltammetric oxidation: (A, B) EO-MCNF-1, (D, E) EO-MCNF-2, and (G, H) EO-MCNF-3

electrode materials for supercapacitors as demonstrated below. According to Messaoudi *et al.*,[83] the transition sequence is described by the following stoichiometric reaction equations with slight modification, even though no particular transition would happen exclusively and thoroughly in each stage.
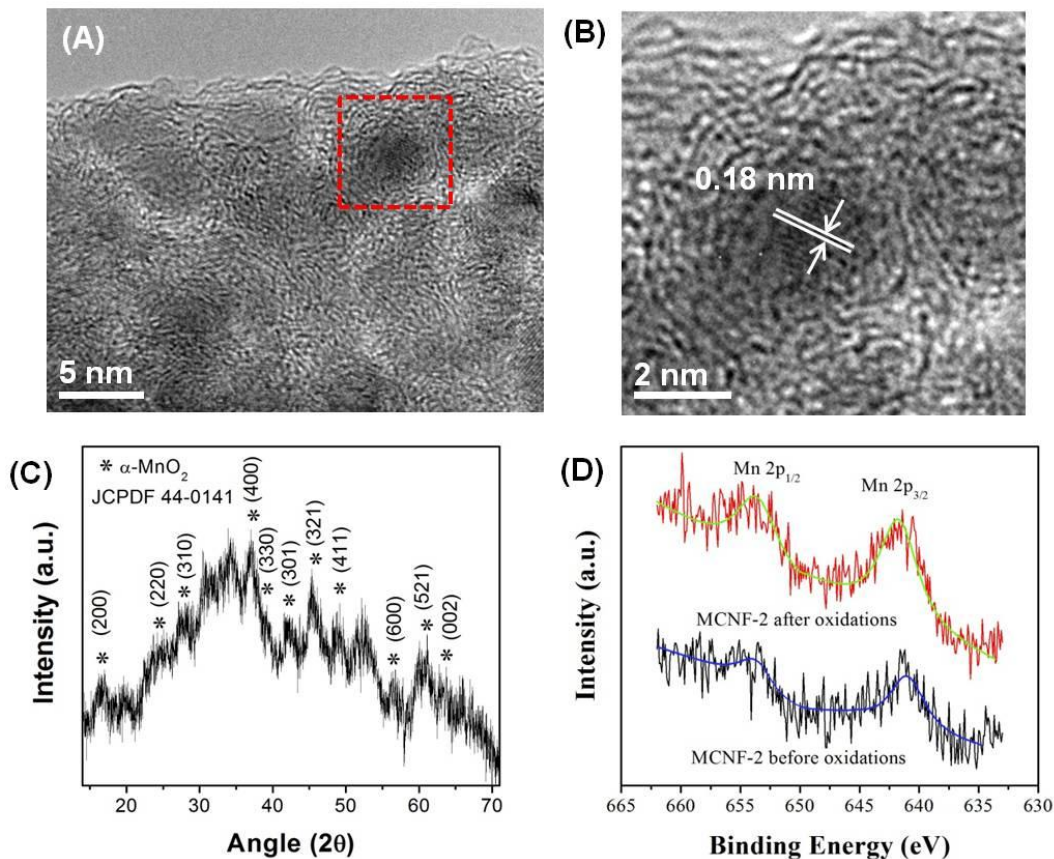
Figure 2.9 (A) Low- and (B) high-magnification TEM images, (C) XRD pattern and (D) XPS patterns of the EO-MCNF-2.

$$3MnO + H_2O \leftrightarrow Mn_3O_4 + 2H^+ + 2e^-$$

$$Mn_3O_4 \cdot 2H_2O + OH^- \leftrightarrow 2MnOOH + Mn(OH)_3 + e^-$$

$$4MnOOH + 2Mn(OH)_3 + 3OH^- \leftrightarrow 6MnO_2 + 5H_2O + 3H^+ + 6e^-$$
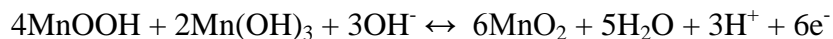
Morphological characterization of electrochemically oxidized MCNFs (denoted as EO-MCNFs thereafter) is conducted by SEM (Figure 2.8). As can be clearly seen, no distinct morphological change was observed after the transition from MCNFs into EO-MCNFs. Both well-defined microscopic and macroscopic morphologies were maintained for the nanocomposite carbon fibers. The preservation of the intercrossing network and surface topographies of our

nanocomposite fibers also indicates their excellent stability and reversibility as promising electrocapacitive materials as demonstrated below.

The EO-MCNFs electrochemically transformed from the MCNFs were also characterized by TEM (Figures 2.9A&B), XRD (Figure 2.9C) and XPS (Figure 2.9D). Apart from meandering graphitic structure, no apparent crystal lattice can be distinguished under high resolution TEM. The dark domains which represent active MnO_2 NPs appear to be amorphous structure, similar to some other reports.[13, 82, 84-86] Powder XRD experiment was carried out on the EO-MCNF-2 by scratching the sample off the titanium current collector. The resultant pattern shows that the EO-MCNF-2 has poor crystal structure of α-MnO_2 (JCPDS card #44-0141). Accordingly, some lattice observed in Figure 5B with plane space of ~0.18 nm is tentatively assigned to (411) plane of α-MnO_2. Also, XPS results validated the phase transformation from MnO to MnO_2.

2.3.3 Electrochemical Performance

Figure 2.10A exhibits the evolutions of CV curves and remarkable uphill leap in higher potential regions and expanded CV integrated areas are observed during the first three cyclic voltammetric oxidations, which is an evident indication of electrochemical oxidations of MnO and increased specific capacitances.[82, 85] Figure 2.10B compares the CV curves of MCNF-2 before electrochemical oxidations and after anodic oxidation and 1000 cycles of CV oxidations, respectively. Before electrochemical oxidations, the specific capacitance (C_s) of MCNF-2 is estimated to be 3.4 F g^{-1} from the calculation of integrated area of CV curve. Partial contribution of the C_s can be attributed to the double-layer energy storage that arises from electrostatic adsorption of electrolyte ions when hierarchical carbon skeleton with enhanced surface area is
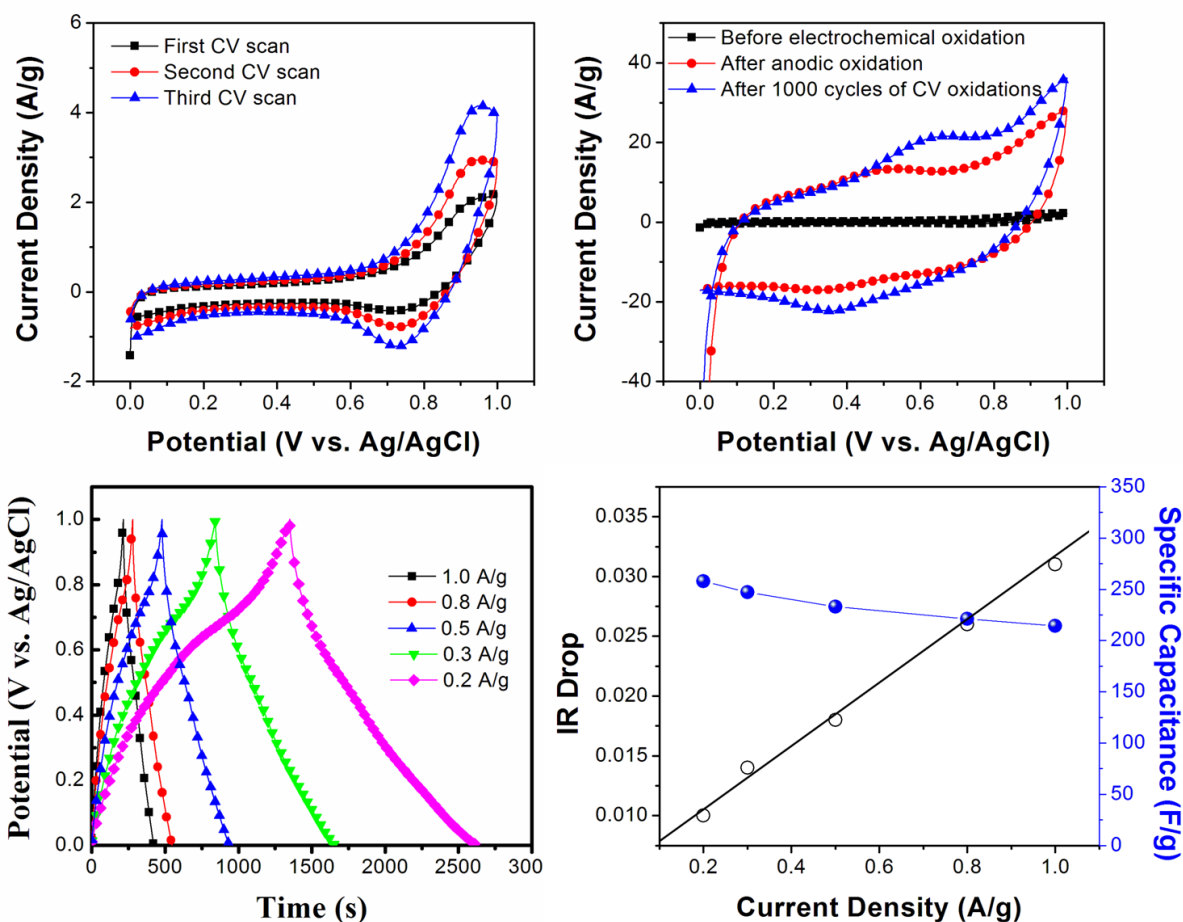
Figure 2.10 (A) The first three cyclic voltammetric cycles (CV) of MCNF-2 at a scan rate of 100 mV s^{-1}. (B) CV evolutions before electrochemical oxidations and after anodic and 1000 cycles of CV oxidations at a scan rate of 50 mV s^{-1}. (C) Galvanostatic charge and discharge curves at various current densities, and (D) specific capacitances and IR drops as a function of the current densities of electrochemically oxidized MCNF-2 (EO-MCNF-2).

taken into account. Particularly noteworthy is that after anodic oxidation at an areal current density of 10 μm cm^{-1} and oxidations of 1000 CV potential cycles, the C_s is dramatically boosted to 100.4 and 128.3 F g^{-1}, respectively. This can be explained by the phase transformation from inactive MnO to pseudocapacitive MnO_2/MnO_x which activates pseudocapacitive energy storage

29

on the surface or near surface of nanocomposites and eventually converts these unique heterogeneous nanostructures into pseudocapacitive electrode materials. Galvanostatic charge and discharge measurements are carried out to further investigate nanocomposites at a variety of current densities. The excellent symmetry of charge and discharge times and the pyramidal waves indicate a superior reversibility of the nanocomposites. The potential plateaus at about 0.7 V and 0.4 V on pyramids are well consistent with the anodic and cathodic peaks in CV studies (Figure 2.10B) and validate the Faradic redox reactions.[7, 33] Figure 2.10D shows the C_s, estimated from discharging times, as a function of the different discharging current densities. The nanocomposites deliver a maximum C_s of 257.9 F g^{-1} at a current density of 0.2 A g^{-1}. Also, the heterogeneous nanocomposite fibers maintain a C_s of 214.2 F g^{-1} at a high current density of 1.0 A g^{-1}, which is about 83.1 % of the value at 0.2 A g^{-1}. The fiber-twined network with kinetically unlimited ion diffusion is mainly responsible for the extraordinary rate capacity. The slope of linear correlation between IR drops and discharging current density can be applied to evaluate the internal resistance of electrode materials.[87] It is interesting to notice that the nanocomposites exhibit a low internal resistance without employing conductive and polymeric additives, which is owing to the firm attachment between nanocomposite electrode materials and current collector. Making use of high speed centrifugal force and wettability of PVP plays an important role in fabrication of mechanically stable electrodes.

2.4 Conclusion

In summary, we have successfully fabricated nanoarchitectured heterogeneous MnO$_x$ NC-encased carbon nanocomposite fibers with MnO$_x$ NC-enriched surface via a novel FS method

followed by calcination and electrochemical oxidations. The controllable ionic diffusion during thermolysis and phase transformation from electrochemically inactive MnO NCs to pseudocapacitive MnO_x NCs by anodic and CV scan oxidations has near surface regions of nanocomposite fibers incorporated with MnO_x NCs accessible to Faradic redox reactions that occur on the surface/near surface. The nanocomposite electrode with electrochemically oxidative enhancements can achieve boosted C_s of 128.3 F g^{-1} from initial value of 3.4 F g^{-1} before oxidations at a scan rate of 100 mV s^{-1}. The Mn^{2+} cations as oxidizing agent can accelerate carbonation of polymeric precursor and make carbonation take place at relatively low temperature condition. The fiber-twined network enables a high rate capacity in view of ideal pathways for ion percolation and electron transportation without kinetic limitations. When current density is up to 1.0 A g^{-1}, the C_s still maintain about 83.1 % of the maximum C_s obtained at 0.2 A g^{-1}. Owing to functional oxide nanoparticles thoroughly shielded by thin layer conductive carbon, the unique heterogeneous nanocomposite fibers are expected to resolve the uncontrollable aggregation and pulverization problems of oxide nanoparticles and become one of the best electrode designs for high performance pseudocapacitors.

CHAPTER III

MIXED-VALENT VO$_X$/POLYMER NANOHYBRID FIBERS FOR FLEXIBLE ENERGY

STORAGE MATERIALS

3.1 Introduction

Flexible/bendable supercapacitors and lithium-ion batteries (LIBs) have becoming promising for the next generation of electronic devices in a variety of sectors such as rollup displays, paper-like gadgets, miniature biomedical and wearable devices.[88-90] Hence a plethora of research efforts has been prompted to exploit new fabrication routes for lightweight, facile and high yielding flexible energy storage materials. In particular, the superior performance of flexible energy storage materials resorts to high mechanical resilience and stable electronic conductivity. In this point of view, carbon materials have been used as backbones or substrates in combination with electroactive transition metal oxides (TMOs).[50, 91-92] However, these hybrid materials are not yet incorporated into devices due to several remaining engineering challenges. These challenges include micro-batch processes necessitated by precise control of reactants, long reaction duration, multi-step hybridizing procedures and, frequently, low availability of expensive carbon nanostructures (including carbon nanotubes, graphene and conductive polymers) commonly prepared by inevitable high temperature treatment and/or tedious synthesis contradicting the requirements of ease manufacture on large-scale of these materials.[93-94]

Here, a high throughput protocol was developed for producing composite fibers from vanadium fluoride/polyvinylpyrrolidone (PVP) precursor with water as the only solvent through the FS technology via centrifugal force. The following low temperature calcination of these forcespun fibers yields heterogeneous bark-textured VO_x/PVP derivative hybrid systems with superior mechanical flexibility and high electronic conductivity. The nonwoven nanohybrid fiber networks demonstrate fast kinetics, and the nanostructured mixed-valent VO_x nanorods exhibit rapid electron transport and ion percolation at high scan rates. This effort is envisioned for developing various hybrid materials that will bring them closer to widespread production and potential energy storage applications for LIBs and supercapacitors.

3.2 Experimental

3.2.1 Materials

polyvinylpirrolidone (PVP, M_W = 1,300,000, Sigma-Aldrich), vanadium (IV) fluoride (VF_4, 95% metal basis, Alfa Aesar). All reagents were of analytical grade and were used without further purification.

3.2.2 Preparation of VO_x/polymer nanohybrid fibers

The precursor solution was prepared by mixing polyvinylpirrolidone (PVP, M_W = 1,300,000, Sigma-Aldrich), vanadium (IV) fluoride (VF_4, 95% metal basis, Alfa Aesar), and deionized water in a Teflon beaker with varying polymer, VF_4 and water ratios. The mixture was then magnetically stirred for approximately 45 minutes, allowed to degas for 3 h to remove any trapped air-bubbles, and spun by a Cyclone 1000-M FS apparatus (Fiberio Technology Corp.,

TX, USA) equipped with a Teflon-coated spinneret (with 3 equally circumferentially spaced orifices) at 7000-12000 rpm with an 8 cm orifice-to-collector distance to create a one-square-foot mat of precursor fibers. The as-spun precursor fibers were calcined in air at 420-600 ℃ for 1-6 h to generate the nanohybrid fibers. The most desirable product was achieved by heating the precursor fibers forcespun from a precursor solution with a PVP/VF$_4$/water weight ratio of 1:1:3 to 450 ℃ at a ramp rate of 2 ℃ min^{-1} and held isothermally for 1 hour.

3.2.3 Characterization

The morphological, structural properties and elemental composition of the resultant product were characterized using a Zeiss Sigma VP SEM equipped with a Kleindiek micromanipulator and back-scatter detector, a FEI Tecnai F30 HRTEM, a Bruker AXS D8 QUEST XRD, a TA Instrument Q500 TGA and a Time-of-Flight Secondary Ion Mass Spectrometer (TOF-SIMS).

3.2.4 Electrochemical Evaluation

The electrochemical performance was studied in a three-compartment cell using a Potentiostat/Galvanostat/ZRA (Gamry Reference 600). 1 M LiClO$_4$ ethylene carbonate (EC)/diethyl carbonate (DEC) (volume ratio = 1:1) solution was employed as electrolyte. For the Galvanostatic charge/discharge testing, the as-calcined free-standing nanohybrid fiber mat was used directly as working electrode, and was charged and discharged at 100 mA g^{-1} to the potentials of 2.0 V and 4.0 V versus Li/Li$^+$. For comparative cyclic voltammetric evaluations at 50 mV s^{-1}, the electrode was fabricated by grinding fibers and polyvinylidene fluoride (PVDF) with a weight ratio of 85:15 in ethanol and then pasting the mixture on alumina foil before

thoroughly drying at 60 ℃ overnight in a vacuum oven. The electrode can be readily rolled up with a tweezer into a rollup electrode.

3.3 Results and Discussion

3.3.1 Morphology and Structure Characterization
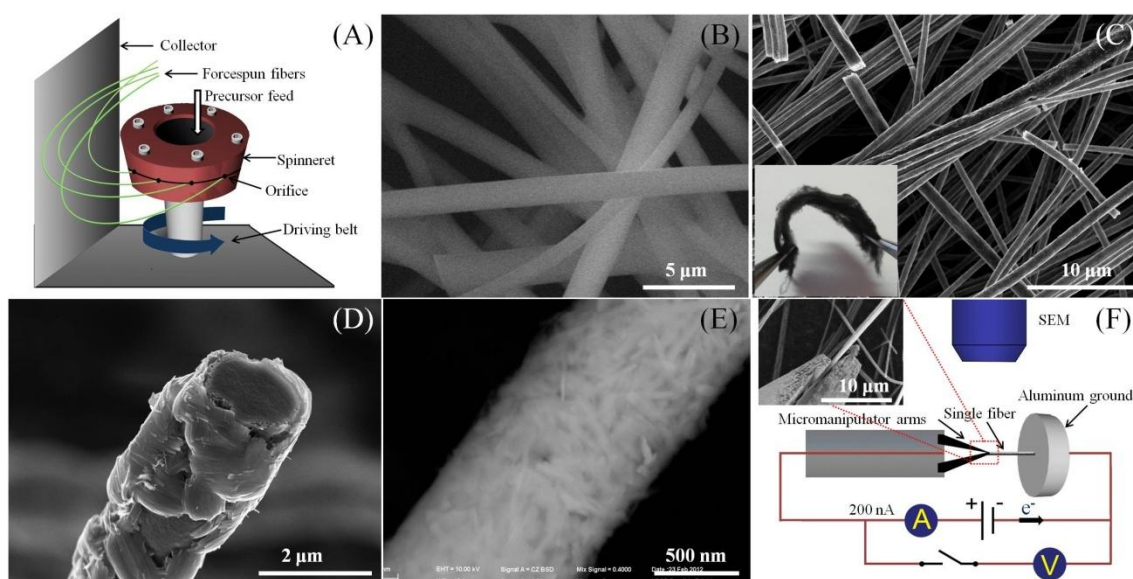
Figure 3.1 (A) Schematic representation of the FS process. (B) SEM image of the as-spun precursor fibers taken under environmental conditions. (C) Low and (D) high magnification SEM images of the as-calcined nanohybrid fibers. Inset in panel C is the photographic image of the corresponding mat exhibiting good flexibility. (E) Back-scattered SEM image of the as-calcined nanohybrid fibers. (F) Schematic representation of the electrical probing setup of micromanipulator under SEM observations.

The FS method (Figure 3.1A) was employed to prepare VF$_4$/PVP fiber mat (Figure 3.1B). The as-spun precursor fibers have smooth surface and diameter ranged from 500 nm to 2

μm. After feeding the precursor solution into the spinning reservoir of spinneret, the high-speed rotational force drove the viscous fluid through and out of orifices, provided the capillary force was exceeded by the centrifugal force and hydrostatic pressure.[45, 59-60] The FS process generates submicro/nanofibers regardless of the complex controlling parameters affecting Taylor cone and jet instability of widely used electrospinning process, *i.e.* high electrical field strength, intrinsic solution/melt conductivity, electrostatic and ionization fields.[95] In the FS process, solution viscosity and orifice-to-collector distance become the major contributing factors. The production rate has been estimated to be $>$ 1 g min^{-1} on a lab scale setup, a demonstration of its unique capability as a high-yield manufacturing technology of submicro/nanofibers.

According to our previous thermal studies on forcespun PVP and corresponding composite nanofibers, the cutoff degradation temperature of PVP is 450 ℃, therefore calcinations were performed on the as-spun precursor fibers at 450 ℃ in this study to thermally transform VF$_4$ to its oxide counterparts with high electronic conductivity and PVP to its moderately cross-linked derivatives with desirable mechanical properties.[96] Figure 3.1C exhibits the randomly oriented network of the as-calcined nanohybrid fibers as free-standing mat capable of being bent readily. The nanohybrid fibers did not undergo shrinkage apparently from the precursor fibers and possess an average axial length of 200 μm. The bark-textured individual nanohybrid fiber is emphasized in Figure 3.1-D. The sheath of vanadium oxide and the backbone of the flexible PVP residual can be clearly identified. The formation of this interesting heterogeneous structure is ascribed to the premature rigid shell of the precursor fibers during uneven heat transmission, which causes distinct inward and outward ionic diffusion rates.[70] After excluding the influence of carbon residual, the back-scattered SEM image (Figure 3.1E) indicates that the superficial sheath comprises fine vanadium oxide nanorods. Noteworthy is that

the heavily-loaded "carrier polymer" in FS processes can provide adequate medium resulting in different ionic diffusion rates at low ramp rates which alleviate burst-nucleation and generate electrochemically favored fine nanostructures in comparison with electrospinning.[97] Therefore, the FS process is essential and unique to generate this type of nanohybrid fibers. We also found that a lower PVP/VF$_4$ ratio and/or calcination temperature could result in hybrid fibers with unassociated highly scattered vanadium oxide nanorods rooted in the polymer skeleton and therefore poor electrical transportations. In addition, the resultant product with a high PVP/VF$_4$ ratio and calcined at 600 ℃ for 6 h showed nanorod-shaped single crystals with high aspect ratio but suffered from unfavorable brittleness.

The electronic conductivity of the nanohybrid fibers was investigated by an electrical probe (Kleindiek micromanipulator) (Figure 3.1F). One individual fiber was positioned by moving the robotic microgripper under the SEM. The conductivity is estimated based on the *I-V* response. The flexible nanohybrid fibers exhibited a high electronic conductivity of 4.48×10^4 S m^{-1}. The XRD pattern (data not shown here) indicates that the vanadium oxide sheath possesses a mixed-valent characteristic and is composed of polymorphic V$_2$O$_5$ and V$_6$O$_{13}$. The incomplete oxidation of hydrolytic product of VF$_4$ and phase transformation were responsible for this mixed vanadium valence formation and polymorphism phenomenon. The mixed-valent vanadium oxide compounds contain both donor and accepter sites interacting by a bridge. The electronic coupling of these two redox sites as well as the "reorganization energy" unpredictably enhances the electron transfer.[98] Consequently, the balance between mechanical flexibility and electronic conductivity could be achieved by forming mixed-valent vanadium oxides within the nanohybrid fiber. The TOF-SIMS study (data not shown here) determined an approximate vanadium/carbon

atomic ratio of 19:18. Moreover, the TGA curve (data not shown here) indicates that about 54.3% oxide residual is eventually present after heating the nanohybrid fibers in air to 800 ℃.

Further structural information about the heterogenerous nanostructures of vanadium oxide was obtained from TEM. Figure 3.2A&B clearly demonstrate the surface of nanohybrid fibers is covered with oblique nanorods ranging from 50-100 nm in diameter, in great accordance with back-scatter SEM image. The high-resolution TEM image (Figure 3.2C) reveals that the individual nanorod is single-crystalline. The characteristic interplane spacings of 0.71 nm and
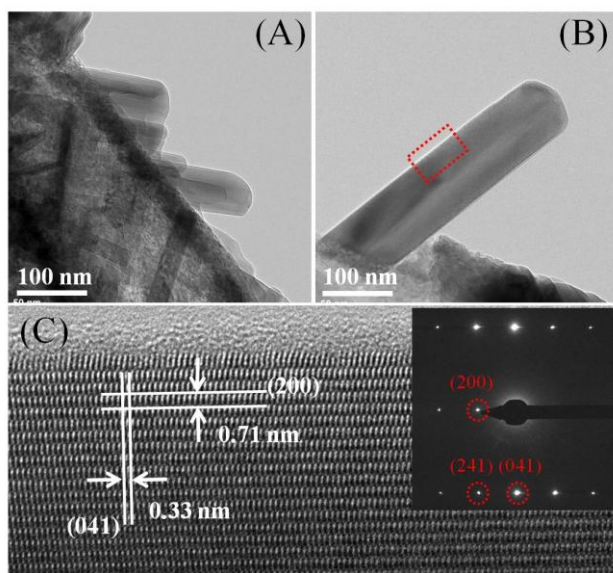
Figure 3.2 (A) TEM of a nanohybrid fiber. (B&C) High-resolution TEM of the nanorods on the nanohybrid fibers. The inset in panel C shows the SAED pattern of the corresponding nanorod.

0.33 nm (corresponding to the (200) and (041) planes, respectively) and the corresponding SAED pattern confirm that these nanorods are made of tetragonal V_2O_5. The high density of the central fiber core constricted the nucleation sites of V_2O_5 and forced the nanocrystals to grow laterally.[99] In other words, the V_6O_{13} phase congregated in the subsurface region of the nanohybrid fibers.

3.3.2 Electrochemical Performance

Figure 3.3A shows the CV measurements of the nanohybrid fibers before and after rolling. Shape changes of the CV curves were not observed, reflecting the potential applications of these nanohybrid fibers as electrode materials for flexible electrochemical energy storage devices. Interestingly, one pair of redox peaks situated at 2.88 and 3.20 V indicating the conversion of V^{4+}/V^{5+} was still well-defined at a scan rate as high as 50 mV s^{-1}. Besides the
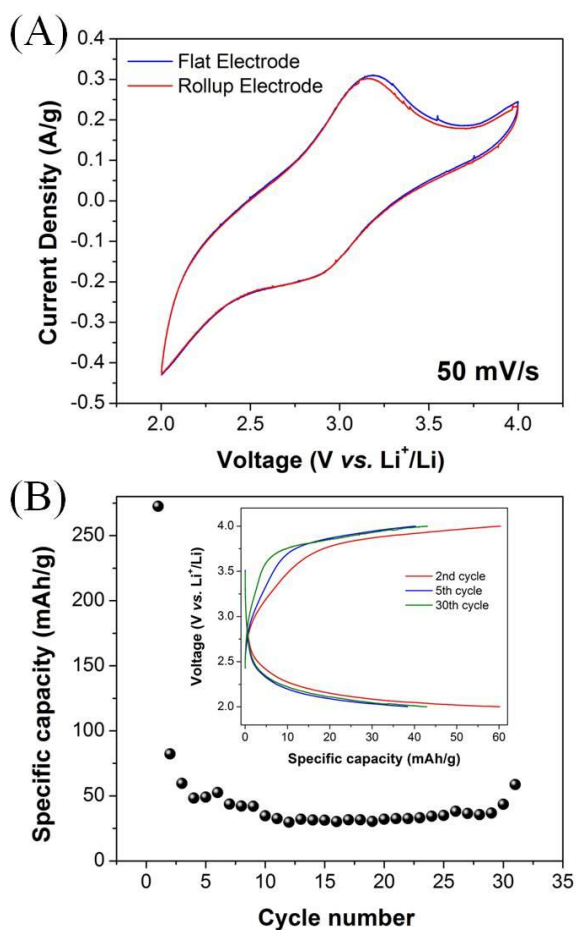
Figure 3.3 (A) Cyclic voltammetric curves of the nanohybrid fibers before and after rolling at 50 mV s^{-1}. (B) Cycling performance of the nanohybrid fibers up to 30 cycles at 100 mA g^{-1}. Inset in panel B shows the galvanostatic charge/discharge curves for the second, 5th and 30th cycles.

advantages of high mechanical flexibility, electronic conductivity and tolerance of volumetric expansion caused by Li^+ intercalation, the intertwining networks and the nanostructured sheath of the one-dimensional nanohybrid fibers allow efficient ion access and shortened ion diffusions without kinetic limitations. The nanohybrid fibers exhibited a first cycle discharge capacity of 276.2 mAh g^{-1} at a current density of 100 mA g^{-1}. After the initial several cycles, they stably delivered discharge capacity of about 46.5 mAh g^{-1} once the solid electrolyte interface layer forms. Our future endeavor includes (i) to lower carbonization temperature of the flexible cross-linked backbone and (ii) to incorporate conducting fillers to further promote the electrochemical performance of the nanohybrid fibers.

3.4 Conclusion

A successful preparation of hybrid VF_4/PVP precursor fibers via a novel Forcespinning process was reported here under the pursuit of a simplified approach and maximized throughput. The manipulative low temperature calcination process generates heterogeneous bark-textured VO_x/PVP derivative nanohybrid fibers. The nanohybrid fibers possess high mechanical stability, electrical conductivity and tolerance of volumetric expansion. When used as electrochemical electrode materials, they exhibit efficient ion access and shortened ion diffusions without kinetic limitations for flexible electrochemical energy storage devices.

CHAPTER IV

THREE-DIMENSIONAL ZNO@MNO$_2$ CORE@SHELL NANOSTRUCTURES FOR

ELECTROCHEMICAL ENERGY STORAGE

4.1 Introduction

Supercapacitors and lithium ion batteries (LIBs) have attracted increasing attention in recent years as energy storage devices, owing to the high power density, excellent reversibility, long cycle life and good operational safety of the former and the high energy density of the latter.[100-102] However, their miniaturization has not kept pace with advances of microelectromechanical systems (MEMS), biomedical and autonomous devices, whose desired on-board power storage happens on exceptionally small geometric scales. In either unit weight (Wh kg^{-1}) or volume (Wh L^{-1}), the amount of energy stored on a given footprint (J mm^{-2}) of these devices is desirable to surpass that of conventional two-dimensional (2-D) battery and supercapacitor configurations. To overcome the shortcomings of these technologies while developing more powerful energy storage devices,[41] one major approach pursued very recently is based on the fabrication of 3-D electrode structures at the nanoscale.

Compared with compact 2-D counterparts, 3-D architectures take advantage of the vertical dimension-height. 3-D nanostructured electrodes possess higher surface/body ratios, larger surface areas, more surface active sites within a small footprint area, and accordingly enlarged areal capacity.[103-104] Therefore, their synthesis is now considered as a new strategy for powering

MEMS and other small autonomous devices. Some efforts have been devoted to engineering 3-Dnanostructures as energy storage electrodes.[105-108] For example, Liu *et al.* built
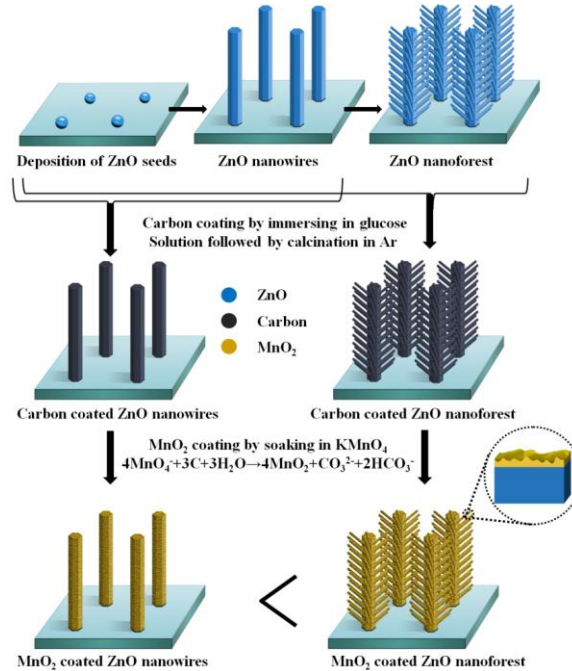
Figure 4.1 Schematic illustration of the fabrication process for the designed 3-D ZnO@MnO$_2$ core@shell nanowire array electrode and its nanoforest counterpart. The latter possesses further boosted electrochemical performance than the former.

electrodes of Co$_3$O$_4$@MnO$_2$ nanowire arrays using sacrificial reactive 3-D carbon template layers. Xia *et al* synthesized Co$_3$O$_4$@NiO core@shell nanowire arrays for supercapacitors with high capacitance and good cycling stability. Yan *et al.*coated V$_2$O$_5$ on SnO$_2$ nanowire arrays to bridge the performance gap between batteries and supercapacitors for high-rate LIBs. All these 3-D core@shell heterostructures consist of high conductive one-dimensional (1-D) nanowires as the core and electroactive transition metal oxide or hydroxide as shells and branches.

In this work, we designed a novel architecture composed of branched nanowire arrays, *i.e.* forest of nanotrees, to further boost electrochemical performance over 1-D nanowire arrays, inspired by branched trees with larger surface area to capture more sunlight.[109] Specifically, we first fabricated both 3-D ZnO@MnO$_2$ core@shell nanowire arrays and branched nanowire array counterpart, *i.e.* nanoforest, using hydrothermal and redox processes. The whole fabrication process is schematically illustrated in Figure 4.1. Moreover, our electrochemical characterization revealed that the 3-D ZnO@MnO$_2$ core@shell nanoforest electrodes possess higher capacitance (5 times), better rate performance, and longer retention of capacitance at higher current densities, compared to their nanowire array counterparts.

To the best of our knowledge, no electrodes composed of nanoforests have been applied to electrochemical energy storage devices yet. This new design not only fills the void in the gallery of heterostructured nanomaterials with a 3-D skeleton applied in electrochemical energy storage devices, but also provides a direction to meet the miniaturization requirements of powering MEMS and other miniaturized functional devices.

4.2 Experimental

4.2.1 Materials

Sodium hydroxide (NaOH), zinc acetate [Zn(O$_2$CCH$_3$)$_2$·2H$_2$O], hexamethylenetetramine (C$_6$H$_{12}$N$_4$, HMTA), polyethylenimine (PEI), ammonia (NH$_3$·H$_2$O) and glucose (C$_6$H$_{12}$O$_6$) were purchased from Sigma-Aldrich. Zinc nitrate hydrate [Zn(NO$_3$)$_2$·6H$_2$O] and potassium permanganate (KMnO$_4$) were purchased from Alfa Aesar. All reagents were of analytical grade and were used without further purification.

4.2.2 Preparation of 3-D ZnO@MnO$_2$ core@shell nanostructures

To demonstrate the advantages of nanoforests over corresponding nanowire arrays in electrochemical energy storage, two different 3-D nanostructures, *i.e.* ZnO@MnO$_2$ nanowire arrays and ZnO@MnO$_2$ nanoforests, were synthesized and compared. The fabrication procedures are illustrated in Figure 4.1. In the first step, ZnO nanoparticles seed solution was obtained through adding 25 mL of 0.03 M sodium hydroxide (NaOH) ethanol solution into 37.5 mL of 0.01 M zinc acetate [Zn(O$_2$CCH$_3$)$_2$·2H$_2$O] ethanol solution drop by drop, and then the mixture was actively stirred at 60 ℃ for 2 h. The seed solution was drop casted onto a titanium substrate. ZnO nanowire arrays were grown from these ZnO quantum dot seeds through immersing in an aqueous precursor solution containing 0.025 M zinc nitrate hydrate [Zn(NO$_3$)$_2$·6H$_2$O], 0.025 M hexamethylenetetramine (C$_6$H$_{12}$N$_4$, HMTA), 0.1 M polyethylenimine (PEI), and 0.15 M ammonia (NH$_3$·H$_2$O) at 60-90 ℃ for 7-15 h. Then the grown ZnO nanowire arrays were thoroughly rinsed with deionized water, and dried in air. After annealed at 350 ℃ in air for 10 min to remove residual organics, ZnO nanowire arrays on Ti substrate were obtained. ZnO nanoforests were obtained through adding ZnO seed solution onto the as-prepared ZnO nanowire arrays as the backbone and subsequently conducting a similar hydrothermal reaction as described above except without adding ammonia or PEI to grow ZnO nano-branches onto the ZnO nanowire array backbones.

To fabricate the final ZnO@MnO$_2$ nanowire arrays and ZnO@MnO$_2$ nanoforests, ZnO@C nanowire arrays and nanoforests were obtained through immersing ZnO nanowire arrays and nanoforests into glucose aqueous solution (0.03 M), respectively, for 1 h and then annealed in argon atmosphere at 500 ℃ for 3 h. This annealing step carbonizes the glucose

molecules absorbed onto the surface of ZnO nanowire arrays and nanoforests. Subsequently, electroactive MnO_2 nanoparticle coatings were purposely decorated onto ZnO nanowire arrays and nanoforests through immersing the hybrid ZnO@C nanowire arrays and nanoforests in 0.03 M $KMnO_4$ aqueous solution for 1 h at room temperature, respectively. A thin layer of MnO_2 nanoparticles was grown on the 3-D ZnO nanostructures through the redox reaction between the carbon coating on ZnO with the $KMnO_4$ solution. At last, the MnO_2 nanoparticles coated ZnO nanowire arrays and nanoforests were rinsed with deionized water and dried at 80 ℃ overnight in vacuum.

4.2.3 Characterization

The morphology and crystal structure of the ZnO@MnO_2 nanowire arrays and nanoforests were characterized through scanning electron microscopy (Carl Zeiss Sigma VP Field-Emission SEM at 2-5 kV), transmission electron microscopy (JEOL JEM-2010 UHR TEM) and high-resolution TEM (HRTEM), coupled with selected area electron diffraction (SAED) and energy dispersive X-ray spectroscopy (EDS). The surface chemical composition and oxidation state of the samples were determined by X-ray photoelectron spectroscopy (XPS) measurement (Kratos AXIS 165 X-ray photoelectron spectrometer). Raman spectroscopy was conducted on a Bruker SENTERRA RAMAN microscope with a 785 nm laser as the excitation source.

4.2.4 Electrochemical Evaluation

Cyclic voltammetry (CV) measurements were conducted on a Gamry Reference 600 electrochemical workstation, using a three-electrode mode in 1 M Na_2SO_4 aqueous solution with a voltage ranging from -0.2 V to 0.6 V at different scan rates (2 mV s^{-1} to 100 mV s^{-1}). A piece

of 0.6 cm^2 sample of ZnO@MnO$_2$ nanowire arrays or nanoforests on titanium foil was used as the working electrode. The reference electrode and counter electrode were Ag/AgCl and a platinum wire, respectively. With a similar setup, charge/discharge (CD) measurements of ZnO@MnO$_2$ nanowire arrays or nanoforests as working electrodes were conducted at various current densities of 0.02 to 0.2 mA/cm^2. Electrochemical impedance spectroscopy (EIS) measurements were performed by applying an AC amplitude of 5 mV in a frequency range from 100 kHz to 0.001 Hz.

4.3 Results and Discussion

4.3.1 Morphology and Structure Characterization

Figure 4.2A, B clearly present the 3-D ZnO@MnO$_2$ core@shell nanowire arrays, and Fig. 1c and d exhibit the typical morphology of the 3-D ZnO@MnO$_2$core@shell nanotrees. These arrays have average lengths over 10 μm, grown perpendicularly on the substrate of the titanium current collector (inset of Figure 4.2A). These nanotrees consist of 3-D ZnO@MnO$_2$ nanowire arrays as the trunks and ZnO@MnO$_2$ nanorods on the trunks as branches with an average length of ~ 800 nm.

HRTEM images of these ZnO@MnO$_2$ core@shell nanowire arrays and nanoforests (Figure 4.3) clearly demonstrate that well-dispersed MnO$_2$ nanoparticlelayers with a thickness of ~ 3 nm were coated on the well-crystalline ZnO nanowire and nanotree backbones, respectively. XPS and Raman data of the as-synthesized 3-D ZnO@MnO$_2$ nanoforests are not shown here. The peaks located at 1021 eV and 1044 eV are assigned to Zn 2p$_{3/2}$ and Zn 2p$_{1/2}$, respectively, indicating that the oxidation state of zinc is +2. The peaks at 653.9 eV and 642.3 eV

are attributed to Mn $2p_{3/2}$ and Mn $2p_{1/2}$ of MnO_2. The identity of ZnO and MnO_2 from the XPS

analysis is consistent with that from the Raman spectrum.
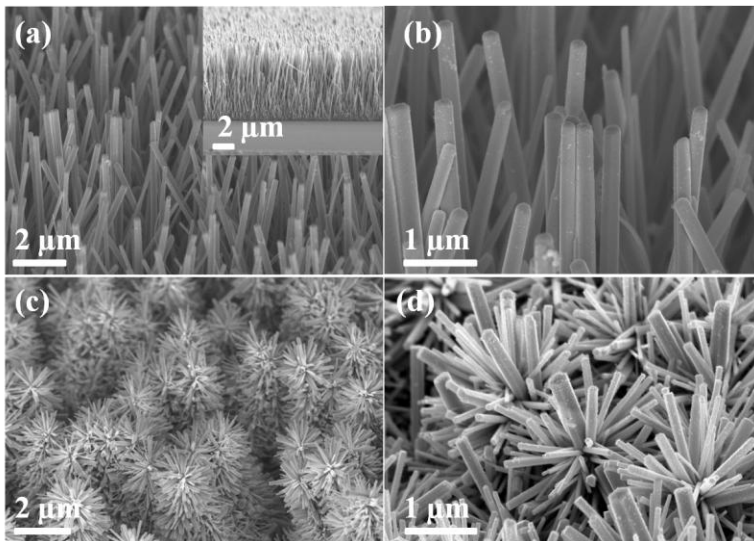
Figure 4.2 Typical SEM images of (A, B) ZnO@MnO_2 nanowire arrays and (C, D) ZnO@MnO_2

nanoforests.
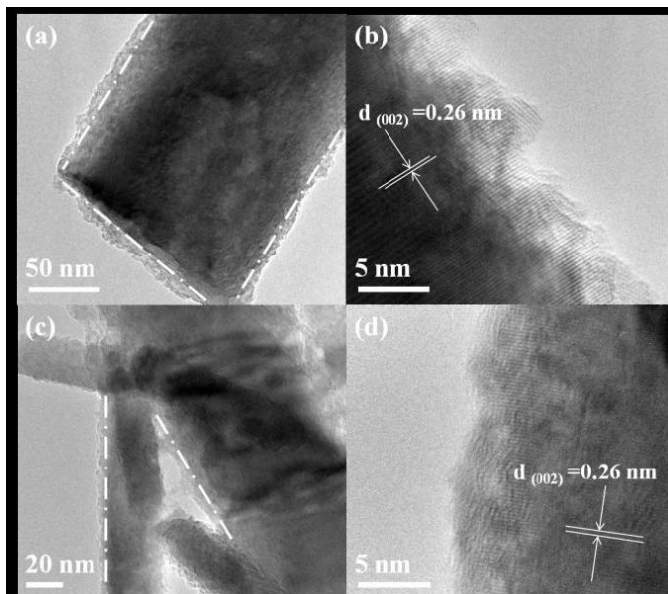
Figure 4.3 Representative TEM and HRTEM images of the synthesized 3-D ZnO@MnO_2

core@shell (A and B) nanowire arrays and (C and D) Nanoforests.

4.3.2 Electrochemical Performance

Cyclic voltammetry (CV) measurements (Figure 4.4A) were performed on the synthesized 3-D ZnO@MnO$_2$ core@shell nanoforest as working electrodes at different scan rates of 2, 5, 10, 20, 50, and 100 mV s^{-1}. In the potential range of -0.2 to 0.6 V (*vs.* Ag/AgCl), no obvious redox peaks were observed, which is characteristic of electroactive MnO$_2$ in this range. These CV curves exhibit approximately rectangular shape, especially at slow scan rates. This observation indicates excellent capacitive behaviour and a low contact resistance of the electrodes made from our synthesized 3-D ZnO@MnO$_2$ core@shell nanoforest, consistent with EIS data discussed below. As commonly observed, the rectangularity gradually expands and is distorted with increasing scan rates. However, the CV curves taken at the same scan rates of electrodes made of the 3-D nanowire array counterpart are evidently more distorted and possess much smaller area (data now shown here). It suggests that the 3-D ZnO@MnO$_2$ nanowire arrays possess faster downgrading capacitance than the nanoforests even though both nanoarchitectures are composed of the same materials and were fabricated by the same procedure. Furthermore, by comparing the CV curves taken at a scan rate of 2 mV s^{-1} with the same lateral size of electrodes made from the 3-D ZnO@MnO$_2$ core@shell nanoforest, nanowire array counterpart and pure titanium substrate (Figure 4.4B), a significant increase in integrated CV area was observed for the 3-D ZnO@MnO$_2$ core@shell nanoforest electrode over the nanowire array electrode, while the pure titanium substrate showed barely any capacitance. The much larger capacitance of the 3-D ZnO@MnO$_2$ core@shell nanoforest electrode can be attributed to the larger accessible surface area of its unique nanoarchitecture and higher loading of the electroactive MnO$_2$ nanoparticle coating over that of the 3-D ZnO@MnO$_2$ nanowire array counterpart at the same footprint.
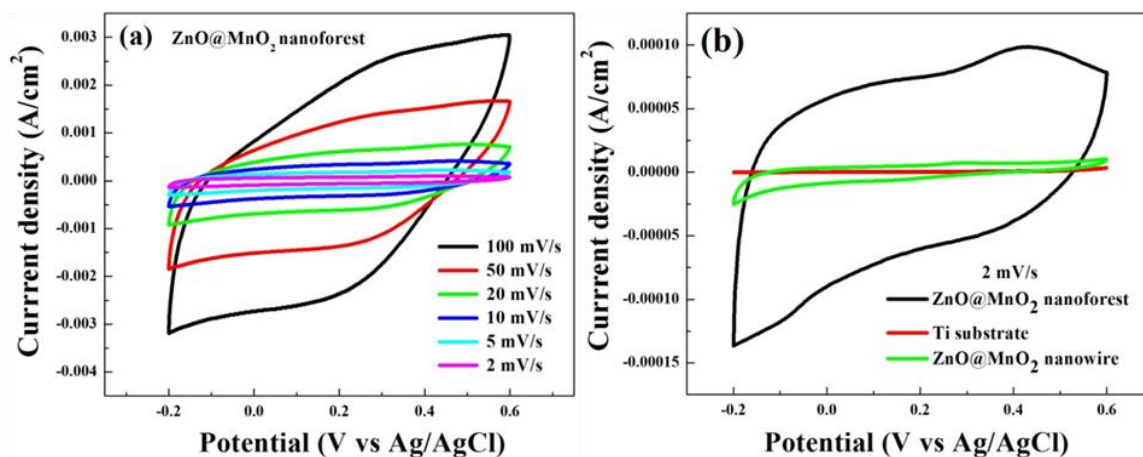
Figure 4.4 (a) Cyclic Voltammetry (CV) curves of ZnO@MnO$_2$ nanforest electrode at different scan rates. (b) CV curves of the 3-D ZnO@MnO$_2$ nanoforests, ZnO@MnO$_2$ nanowire arrays, and titanium substrate at 2 mV s^{-1}.

From the charge–discharge (CD) measurements conducted on both 3-D ZnO@MnO$_2$ core@shell nanoforest and nanowire array electrodes (Figure 4.5A, B and C), their specific areal capacitances C_{area} at different current densities (Figure 4.5D) were calculated according to their discharge profiles. The respective charging time and discharging time are nearly the same, indicating superior reversibility of charging and discharging reactions of the electrodes made from both the synthesized 3-D ZnO@MnO$_2$ core@shell nanoarchitectures. The C_{area} of 3-D ZnO@MnO$_2$ core@shell nanoforest electrode is estimated to be 31.30 mF cm^{-2}, which is nearly 5 times that of the 3-D ZnO@MnO$_2$ core@shell nanowire array electrode (6.30 mF cm^{-2}). The high C_{area} of the nanoforest electrode results from its enhanced surface area and higher loading amount of MnO$_2$ nanoparticle coating on the 3-D ZnO nanoforest backbone over those of the nanowire array counterpart. It implies the following electrochemical reactions between MnO$_2$ and electrolyte with possible intercalation or deintercalation of Na$^+$ or H$_3$O$^+$.

49
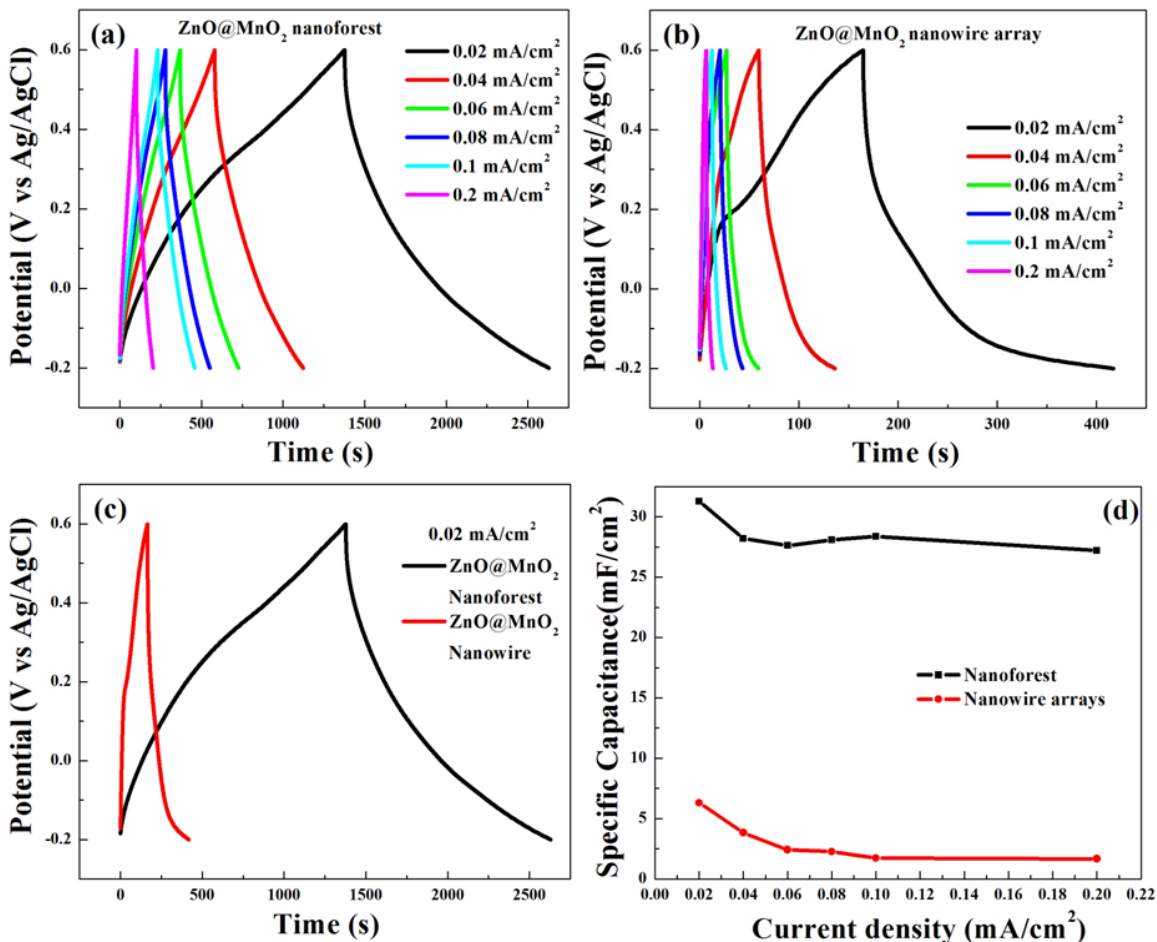
Figure 4.5 (A) Charge/discharge (CD) curves of 3-D ZnO@MnO$_2$ nanoforests as electrode at different current densities. (B) Charge/discharge (CD) curves of ZnO@MnO$_2$ nanowire arrays as electrode at different current densities. (C) CD curves of ZnO@MnO$_2$ nanowire arrays and nanoforests as working electrodes, respectively, at current density of 0.02 mA cm^{-2}. (D) Specific capacitances of ZnO@MnO$_2$ nanoforest and nanowire arrays at different current densities.

$$MnO_2 + M^+ + e^- \leftrightarrow MnOOM, M^+ = Na^+ \text{ or } H_3O^+$$

This novel nanoforest architecture utilizes space more efficiently than the nanowire array counterpart, guarantees effective interfacial contact between the electrolyte

and the electroactive MnO_2 thin layer, and offers improved electron transfer pathways from the 3-D ZnO nanoforest backbone to the current collector.

Moreover, it is evident that the 3-D $ZnO@MnO_2$ core@shell nanoforest electrode delivers higher capacity than the $ZnO@MnO_2$ core@shell nanowire array electrode. The 3-D $ZnO@MnO_2$ core@shell nanoforest electrode possesses 87% capacitance retention while the nanowire array counterpart has only 26% when discharging current density increases from 0.02 to 0.2 mA cm^{-2}. The higher rate capability of the 3-D $ZnO@MnO_2$core@shell nanoforest electrode may be attributed to the unique 3-D interconnected nanoarchitecture with elevated conductivity from the 3-D ZnO nanoforest backbone and larger specific surface area on the same footprint. These structural advantages promote the maintenance of good electrochemical stability at the larger voltage range and also accelerate charge separation and transport. As reported in the literature, the decrease in specific capacitance with increasing current density results from the internal resistance of electrodes.[10] Therefore, the higher capacitance retention of the 3-D $ZnO@MnO_2$ core@shell nanoforest electrodesuggests a lower internal resistance over the corresponding nanowire array electrode, as confirmed by our EIS data not shown.

Compared to the conventional 2-D electrode configurations of traditional batteries and supercapacitors, and even the most recently engineered 3-D nanostructured electrodes, *e.g.* the as-synthesized 3-D $ZnO@MnO_2$ core@shell nanowire arrays shown here, our smartly designed electrodes with the 3-D $ZnO@MnO_2$ core@shell nanoforest architecture are able to enhance the surface area and loading of electroactive MnO_2 on the same lateral footprint, while the 3-D ZnO nanotree backbone provides an ideal pathway for efficient charge transport. The main reasons behind the superior electrochemical performance of the nanoforest electrode possibly include: (i)

more electroactive MnO_2 nanoparticles were coated onto the 3-D ZnO nanotrees with larger surface area than the nanowire arrays as the backbones with the same footprint; (ii) comparatively higher percentages of electroactive MnO_2 coating were deposited onto the ZnO branches than the ZnO trunk due to the smaller diameter of the former; and (iii) the extra loading of the coated electroactive MnO_2 nanoparticles on this novel 3-D ZnO nanoforest architecture over that of thenanowire array counterpart were also finely dispersed, directly grown on the current collector, and so still have fast charge transport paths.

Moreover, the MnO_2 shell coating is amorphous, as confirmed by HRTEM and SAED (Figure 4.3). Amorphous MnO_2 was reported to be more desirable for supercapacitor applications owing to its high surface area and low mass density, compared with crystalline MnO_2.[110-111] The thin layer of amorphous MnO_2 enables fast and reversible faradaic reaction by a shortening ion diffusion path with large areal loading to achieve high specific capacitance while the 3-D ZnO nanotree backbone with high specific area provides highly conductive "highway" channels for effective electron transport. The novel design contributes to the superior capacitance and rate capability of our fabricated 3-D ZnO@MnO_2 core@shell nanoforests with reduced diffusion lengths of ions, highly accessible surface area and good electrical conductivity. Further studies are underway by integrating these novel 3-D ZnO@MnO_2 core@shell nanoforest electrodes into miniaturized LIBs and supercapacitors.

4.4 Conclusion

In summary, smartly designed 3-D ZnO@MnO_2 core@shell nanostructures have been successfully synthesized. These novel nanoarchitectures efficiently increase the accessible

surface area of electroactive materials to the electrolyte, loading amount of electroactive materials per unit substrate area, and electrical conductivity of the hybrid electrode. The 3-D ZnO@MnO$_2$ core@shell nanoforest electrodes offer five times higher areal capacitances, advanced rate capability, and better charge-discharge stability, compared with their corresponding nanowire array counterpart. The present work indicates that our smartly designed 3-D nanoforest electrodes possess great application potentials for miniaturized energy storage devices.

CHAPTER V

ASYMMETRIC SUPERCAPACITORS WITH DOMINANT PSEUDOCAPACIANCE BASED

ON MNO_2 NANOFLOWERS IN A NEUTRAL AQUEOUS ELECTROLYTE

5.1 Introduction

Consumer and industrial demand for compact, low mass and efficient electrical power devices is driving the development of higher power and energy density capacitor and batteries. As a promising alternative being able to provide a power-energy density balance that fills the gap between Li-ion batteries and conventional electric double-layer capacitors (EDLCs), supercapacitors which make use of both fast surface/subsurface redox reactions accompanying reversible phase changes and electric double-layer capacitance recently have attracted intensive interest.[2, 112-113] They employing aqueous electrolytes, especially neutral solutions, offer particular advantages over those using organic or ionic liquid electrolytes in terms of higher power density, higher ionic conductivity, lower fabrication and maintenance cost, superior safety and environmental benignness.[114-115] To overcome their comparatively narrow stable potential window and limited energy density, asymmetric supercapacitors (ASCs) incorporating a pseudocapacitive or battery-type electrode (energy source) and an EDLC-type electrode (power source) are becoming desirable electrochemical energy storage devices. However, some redox-active cathode materials, such as Co_3O_4, PbO_2 and $Ni(OH)_2/NiOOH$, can only perform in extreme pH media, thus causing environmental problems. $RuO_2 \bullet xH_2O$

54

and IrO_2 are cost-prohibitive, and VO_x systems face toxicity, water-solubility and cycling fading issues in aqueous solutions.

In comparison, MnO_2 is a promising pseudocapacitive candidate because of its low cost, environmental friendliness and rapid charge-discharge capability. So far, no reported MnO_2-based ASCs with pure manganese oxides as electrode materials deliver satisfactory energy densities, *e.g.* MnO_2//activated carbon (AC) with ≤ 28.8 Wh kg^{-1}.[116-125] When nanostructured MnO_2 is hybridized with conducting carbon nanotube (CNT), graphene or graphite nanosphere skeletons via tedious synthetic procedures, only reasonable energy and rate performance have been achieved even with the facilitated charge transport on hybridized interlayers, as demonstrated recently as graphene-patched CNTs@MnO_2//CNTs/polyaniline (24.8 Wh kg^{-1}),[126] and MnO_2/graphene//graphene/Ag (50.8 Wh kg^{-1}).[127] Moreover, these hybridized ASCs sacrifices from their multi-step processing, micro-batch production and compromised gravimetric value delivery. Consequently, safe and reliable MnO_2-based ASCs with high energy/power delivery, low-cost, environmental friendliness and ease of manufacture are urgently needed to connect their sustainable energies to power grids and hybrid vehicles. In this study, one such example based on pure manganese oxide nanoflowers (MnO_2-NFs) has been prepared by a novel and facile process and assembled into high performance ASCs.

Remarkable results of nanostructured supercapacitors are generally attributed to the large surface area (double-layer capacitive effect) and short charge transport path lengths (pseudocapacitive effect) of electroactive nanomaterials. As electrochemically active materials approach nanoscale dimensions, pseudocapacitive effect becomes increasingly important.[128-129] For example, a layered intercalated Na_xMnO_2 (x = 0.7 and

0.91) has been demonstrated recently as an enhanced electrode material with fast spontaneous ionic diffusion into interlayer space and thus optimized pseudocapacitive effect.[130] However, no studies have been reported in the literature on the successful fabrication of pseudocapacitance dominant ASCs based on manganese oxides, not even mention their pure forms, for high energy applications as we demonstrated here. Our cathode material of layered MnO_2-NFs (~25 nm in diameter) was synthesized through a novel pyrrolidone-ring opening reaction as described below. Without using tedious fabrication and hybridization processes (*e.g.* with graphene as reported in ref. 17), our easily assembled MnO_2//KCl//CNTs ASCs possess one of the highest reported energy densities (45.4 Wh kg^{-1}). Moreover, pseudocapacitance domination with rarely observed redox peaks was confirmed from our ASCs, for the first time from pure manganese oxide cathode material, due to nanoscale size effect, high interlayer ionic mobility, and fast kinetics of our electrodes offer. In terms of energy storage performance, our ASC devices have realized the intermediate state between supercapacitors and lithium ion batteries in a facile, cost-effective and environmentally friendly fashion. It is encouraging that dominant pseudocapacitance can outperform previous tedious hybridization efforts for high performance energy storage devices.

5.2 Experimental

5.2.1 Materials

N-Methyl-2-pyrrolidone (NMP), Potassium permanganate ($KMnO_4$), Multiple-walled carbon nanotubes (MWCNTs, product No. 636517) were purchased from Sigma Aldrich.

5.2.2 Preparation of MnO$_2$ nanoflowers

In a typical synthesis, 0.8 mmol of KMnO$_4$ was dissolved into 36 mL of deionized water under vigorous magnetic stirring for 20 min. Then 4.385 mL of N-Methyl-2-pyrrolidone (NMP) was added into the above solution and the mixture was stirred for another 5 min before kept still at 20-60 ℃ for 16 h. Subsequently, the brown-black precipitate was collected and repeatedly washed with deionized water and ethanol, and then dried in a vacuum oven overnight. Functionalization of carbon nanotubes (CNTs): 0.1 g of pristine MWCNTs (Sigma Aldrich, product No. 636517) were immersed into 150 mL concentrated nitric acid and refluxed at 70 ℃ for 3 h to remove metal catalyst impurities and yield oxygenated functional groups on the surface. The CNTs were filtered with a 0.45 μm PTFE membrane and washed with deionized water until the pH value of the supernatant was close to 7. The resultant CNTs were redispersed into ethanol for further utilization.

5.2.3 Characterization

The MnO$_2$ were characterized by field emission scanning electron microscopy (SEM, Carl Zeiss Sigma VP, equipped with scanning transmission electron microscopy (STEM)), energy dispersive X-ray spectroscopy (EDS), transmission electron microscopy (TEM, Zeiss LEO 900), X-ray powder diffraction (XRD, Rigaku Miniflex II with Cu Kα radiation, Raman spectroscopy (Bruker SENTERRA, 785 nm laser as excitation source), porosimetry analyzer (Micromeritics ASAP 2020 Analyzer, nitrogen adsorption at 77K), and Fourier transform infrared spectroscopy (FTIR, Thermal Nicolet Nexus 470 spectrometer).

5.2.4 Electrochemical Evaluation

All electrochemical measurements were conducted using a Gamry reference 600 Potentiostat/Galvanostat/ZRA workstation. For three-electrode testing, platinum gauze and Ag/AgCl were used as the counter and reference electrodes, respectively. The working electrodes of MnO_2 nanoflowers (NFs) or CNTs were fabricated as below: The as-prepared MnO_2-NFs (70 wt.%) were evenly mixed and grinded with carbon black (20 wt.%) and polyvinylidene fluoride (PVDF, 10 wt.%) in ethanol and the formed slurry was pasted onto a graphite paper disk (19 mm in diameter). The CNT electrode was prepared by pasting a mixture of CNTs and PVDF (90:10 in weight ratio) onto graphite fiber paper disk. They were pre-dried in a vacuum oven at 70 °C overnight. The graphite fiber papers are chosen as current collectors to prevent capacitance fading from delamination issue and an undesirable electrochemical corrosion towards traditional metallic foils. The porous characteristic of them allows heavy depositions of electroactive materials without penalizing the rate capacity of ASCs to deliver sufficient power for practical applications. The specific capacitance in this work is obtained after excluding the slight contribution of graphite fiber paper.

Based on CV measurements, the charges (q) stored on both electrodes were balanced according to $q = C_s \times \Delta V \times m$, where C_s is the specific capacitance, ΔV is the potential window, and m is the mass of active electrode material.

To build our ASCs, the optimal mass ratio between the MnO_2-NFs and CNTs was calculated to be 0.48 based on the relationship of $q^+ = q^-$ with respective Cs of MnO_2-NFs and CNTs as 145.4 and 70.3 F g^{-1}, respectively, at 20 mV s^{-1}. The actual loading amount for positive and negative materials on graphite current collector is 0.62 mg and 1.02 mg including the additives, respectively. The MnO_2-NFs//CNTs ASCs separated by an electrolyte-cast glassy fiber separator (Millipore Co., 0.45 μm pore size, 19 mm in diameter) were then assembled into a

stainless steel split flat cell (MTI Co.) in an Ar-filled glove box. The 2 M KCl aqueous solution was purged with high purity argon for 30 min for oxygen removal and used as the electrolyte. Chloride electrolyte was chosen over conventional sulfate electrolytes deliberately to improve the mobility of cations due to the relatively small ionic radius of chloride anions (ionic radii 1.67 Å of Cl^- vs 2.30 Å of SO_4^{2-}) in order to further reduce the kinetic limitations. The MnO_2-NFs//MnO_2-NFs and CNTs//CNTs symmetric supercapacitors were constructed following the same procedure. The mass is measured using A&D HR-202i analytical balance with readability of 0.01 mg.

5.3 Results and Discussion

5.3.1 Morphology and Structure Characterization

Experimentally, MnO_2-NFs composed of $K_{0.26}MnO_2$ nanoflake assemblies were first synthesized via a facile and green process, *i.e.* a pyrrolidone ring-opening reaction between N-Methyl-2-pyrrolidone (NMP) and oxidizing $KMnO_4$. FESEM and TEM images (Figure 5.1A, B) show that the product possesses a mesoporous network of MnO_2-NFs. These MnO_2-NFs with average diameter of ~25 nm are assemblies of ultrathin nanoflakes. STEM image and its corresponding size distribution (Figure 5.1C) confirm that these MnO_2-NFs are highly monodispersed. The hysteresis loop in the nitrogen sorption isotherm indicates a surface area of ~ 201.3 m^2 g^{-1}, and the average pore diameter between the MnO_2-NFs is ~22 nm (Figure 5.1D). Raman spectrum (Figure 5.1E) shows two distinct peaks of 575 cm^{-1} and 630 cm^{-1}, which are attributed to the Mn-O stretching vibration in the MnO_6 basal plane and the symmetric stretching vibration of the

MnO$_6$ group, respectively.[131] XRD pattern (Figure 5.1F) matches well with monoclinic potassium birnessite (JCPDS no. 80-1098). It means that the ultrathin nanoflakes consist of 2D sheets of edge-shared MnO$_6$ octahedra with interlayered K$^+$ cations and water
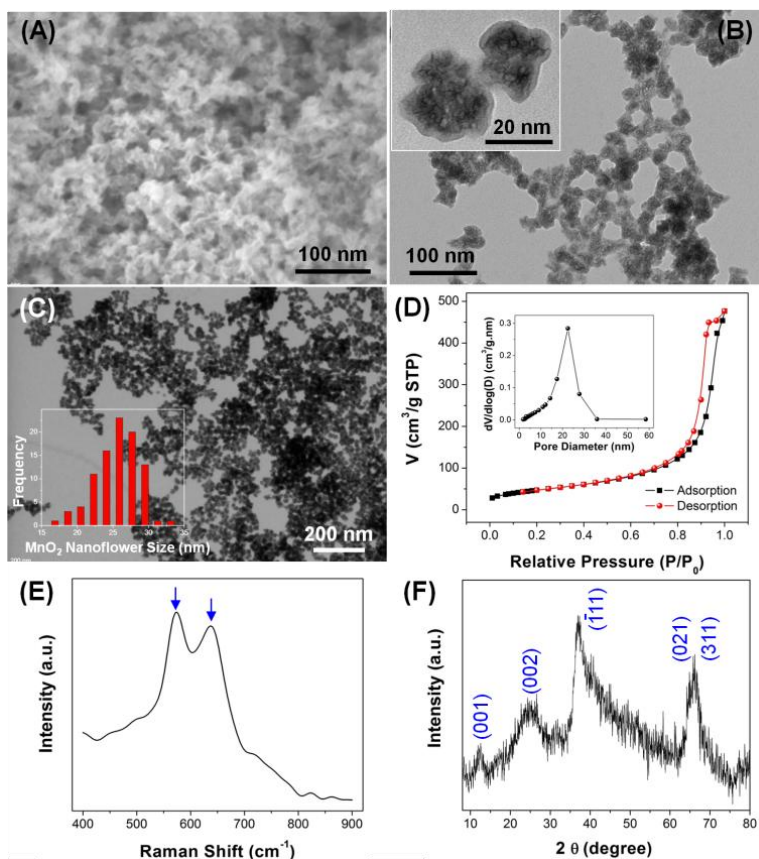
Figure 5.1 The as-synthesized MnO$_2$-NFs: (A) FESEM image, (B) TEM images, (C) STEM image (inset shows the size distribution), (D) nitrogen adsorption and desorption isotherms, (E) Raman spectrum, and (F) XRD pattern.

molecules.[132-133] The EDS pattern confirms an elemental combination of 5.21% K and 19.84% Mn, *i.e.* an empirical formula of K$_{0.26}$MnO$_2$, from the synthesized nanoflowers (data now shown here). Based on the IR spectra shown in Figure 5.2, we hypothesized that these defined MnO$_2$-based nanostructures were generated from the reduction of

KMnO$_4$ by NMP molecules through a pyrrolidone ring-opening reaction. More importantly, the generated birnessite-type MnO$_2$ nanoflakes have a unique open layered crystal structure with pathways from surface to electroactive subsurface sites for alkali cations. The high content of interlayer K$^+$ ions endows high mobility for efficient Faradic
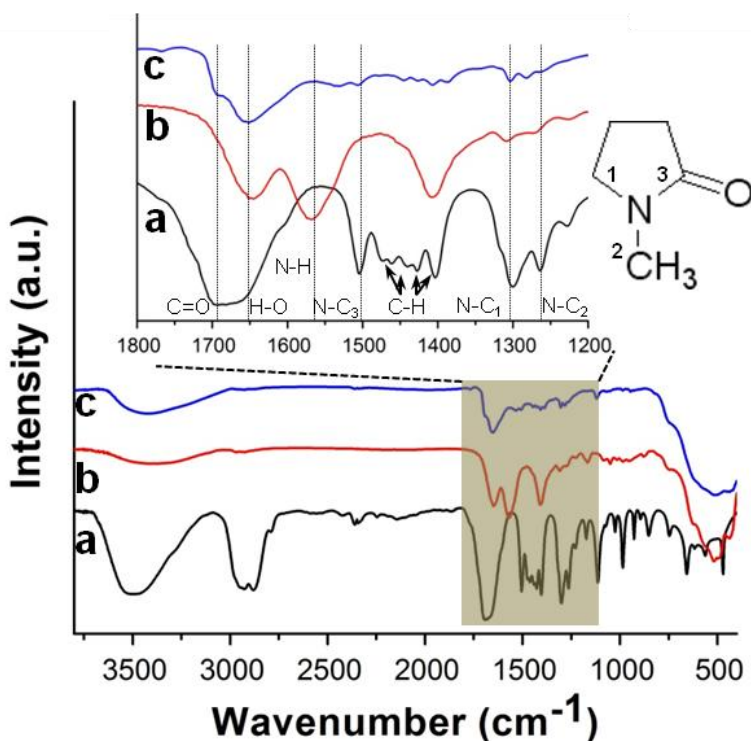
Figure 5.2 FTIR spectra of (a) pure NMP, (b) filtrated MnO$_2$-NFs after DI water rinse, and (c) thoroughly rinsed MnO$_2$-NFs with DI water and ethanol.

reactions. At the meantime, the accessible pores with feasible pore diameter between the MnO$_2$-NFs offers open straits for electrolyte infiltration. Therefore, these fine ultrathin nanoflake assemblies with a large number of accessible active sites are expected to allow fast kinetics of spatial electrolyte transportation and alkali ionic diffusion, and thus efficient surface and subsurface pseudocapacitive reactions, as confirmed below.

In virtue of the strong acidity and oxidizing property of $KMnO_4$, we hypothesize that the pyrrolidone ring-opening reaction of the NMP molecules would yield refined MnO_2 nanostructures. In our synthesis, overabundant NMP is used to react with strong oxidizing agent $KMnO_4$ to synthesize homogeneously distributed MnO_2 nanostructures at relatively low temperature. The high bond strength of C-N (292 kJ mol^{-1}) would give rise to a high reaction activation energy and accordingly brings a significant effect on MnO_2 nucleation and growth rates. Infrared spectra (Figure 5.2) were recorded to insightfully investigate synthesis process. The resultant precipitation was first deliberately filtrated and rinsed with water to exclude the influence of residual NMP to the effect that the superficial product compounds on MnO_2 could be detected by IR spectrum and this sample is denoted as filtrated MnO_2 (Figure 5.2b).

As shown in Figure 5.2, most interesting observation in the IR curve from the filtrated MnO_2 is that the $N-C_3$ stretching vibration bands, located at 1504 cm^{-1}, of N-C=O in the pyrrolidone ring disappears, whereas the $N-C_1$ at ~1264 cm^{-1} and $N-C_2$ bonds at ~1301 cm^{-1} have similar chemical environments in comparison with IR spectrum of pure NMP. The other great change is an apparent absorption peak at ~1567 cm^{-1} corresponding to N-H bending vibration of amines emerges in filtrated MnO_2 specimen. Additionally, the relative intensity difference among the C-H vibrational bands is noticeable, which was regarded as evidence of capping ligands chemisorbing on the MnO_2 nanocrystals. Meanwhile, a remarkable broad band centered at 500 cm^{-1} can be ascribed to the Mn-O vibrations in MnO_6 octahedra. The results demonstrate that the NMP undergoes the $N-C_3$ breaking of pyrrolidone rings in the presence of $KMnO_4$ and generate MnO_2 in spite of not eliminating the possibility that the partial NMP might be accompanied with their intrinsic hydrolysis in acidic atmosphere. However, whether the hypothetic by-product, namely 4-(Methylamino)butyric acid, is able to continue being oxidized

by $KMnO_4$ through the breaking of C-N bonds is still under investigation and the likelihood of the occurrence of oxidative azo coupling reaction among the C-NH-C bonds is ruled out due to the absence of acidic catalyst and overabundance of NMP addition.

Therefore, the plausible formation mechanism of these monodisperse sub-30 nm MnO_2-NFs is as follow: N-Methyl-2-pyrrolidone (NMP) reduces $KMnO_4$ to generate MnO_2. The initially formed MnO_2 nuclei experience a rapid growth and fuse into amorphous aggregations. As the reaction proceeds, an Ostwald ripening mechanism takes over the growth. The ultrathin nanoflakes form according as the lamellar crystal structures of birnessite-type MnO_2 and/or anisotropic growth caused by the selective chemisorption of 4-(Methylamino)butyric acid on certain crystal planes, and subsequently self-assemble into flower-like nanostructures. The further growth of these nanoflowers stops after depletion of $KMnO_4$ in the solution. The possible surface capping by 4-(Methylamino)butyric acid and/or its protection networks by hydrogen bonds between its nitrogen donors may prevent MnO_2-NFs from growing. Comparing to previous studies, the high activation energy for the pyrrolidone ring-opening of NMP is capable of effectively downsizing the formed MnO_2-NFs.

5.3.2 Electrochemical Performance

Before assembling our ASCs using the as-synthesized MnO_2-NFs as cathode combining with functionalized CNTs as anode in neutral KCl aqueous electrolyte solution (Figure 5.3A), cyclic voltammetric (CV) measurements with a three-electrode setup were performed at a scan rate of 20 mV s^{-1} in 2 M KCl aqueous electrolyte within potential windows of 0 to 1.0 V and -1.0 to 0 V (*vs.* Ag/AgCl) on the MnO_2-NFs and CNTs, respectively (Figure 5.3B). These two CV curves exhibit near mirror-images with respect

to the zero-current axis, indicating both materials possess good reversibility.[134-136] According to the schematic illustration in Figure 5.3A, MnO$_2$-NFs//CNTs ASCs were assembled with the optimal mass ratio of 0.48 (m_{MnO2}/m_{CNTs}). The fabricated ASCs exhibit a stable potential window up to 2.0 V without noticeable H$_2$ or O$_2$ evolution at the potential cut-offs (Figure 5.3C). Unlike previous investigations in acid electrolyte, *e.g.* 1 M H$_2$SO$_4$ aqueous solution, the operating window would be limited to ~1.2 V due to H$_2$
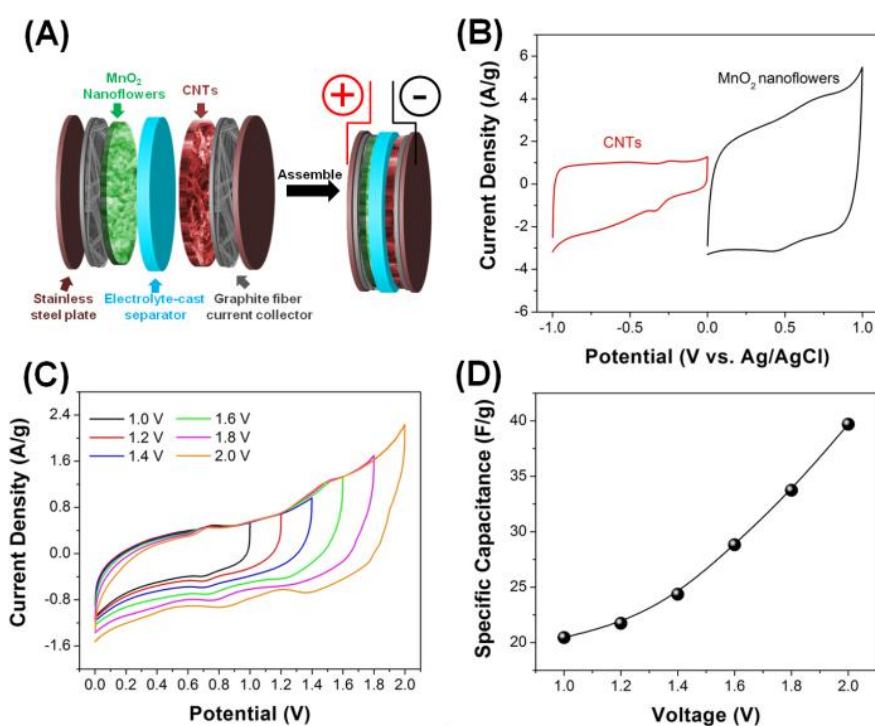
Figure 5.3 ASCs assembled from the as-synthesized MnO$_2$-NFs and CNTs: (A) Schematic illustration. (B) Comparative CVs of MnO$_2$-NFs and CNTs at a scan rate of 20 mV s^{-1} in a three-electrode system. (C) CVs of the assembled ASCs measured at various potential windows at a scan rate of 20 mV s^{-1}. (D) Specific capacitance of the assembled ASCs as a function of the extending potential window at a scan rate of 20 mV s^{-1}.

gas evolution from the reaction of H$^+$ ions.[8, 119, 137] Favourably, in neutral aqueous electrolytes, the concentrations of H$^+$ and OH$^-$ ions are too low to induce gas evolution

reactions. Consequently, the specific capacitance of our ASCs boosts from 20.5 to 39.7 F g^{-1} when the potential window is broadened from 1.0 to 2.0 V (Figure 5.3D). Consequently, the delivered energy from our ASCs is improved by 674.6% according to $E = \frac{1}{2} C_s \times (\Delta V)^2$.

Figure 5.4A shows the CV scans from our ASCs at different scan rates. Two redox couples situated at 0.78/0.54 V and 1.48/1.26 V were observed. To the best of our
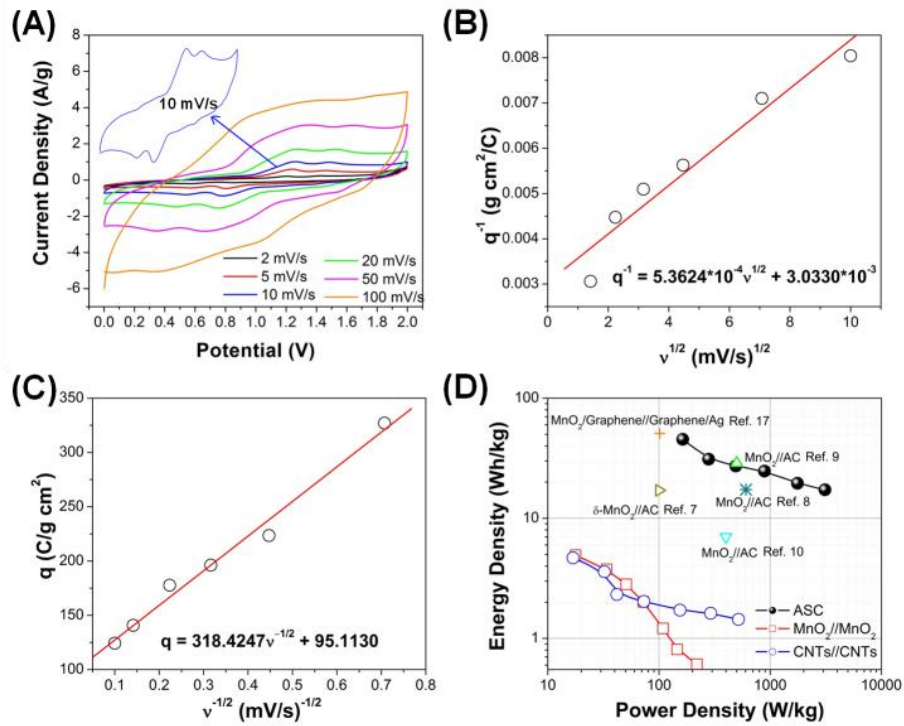
Figure 5.4 Capacitance and energy/power density of the assembled ASCs: (A) CV curves at different scan rates, (B) Dependence of voltammetric charge q^{-1} on $v^{1/2}$, (C) Dependence of voltammetric charge q on $v^{-1/2}$, and (D) Ragone plots of energy density *vs* power density compared to those from symmetric MnO_2-NFs//MnO_2-NFs and CNTs//CNTs supercapacitors as well as reported typical ASCs as references.

knowledge, this phenomenon rarely happens in MnO_2-based supercapacitors. From most MnO_2-based ASCs, rectangular/quasi-rectangular CV profiles imply a nearly ideal capacitive mechanism with fast reversible charge/discharge properties.[124, 134] However, it appears in $LiMn_2O_4$-based Li-ion batteries, and these double redox peaks are due to the intercalation/deintercalation of alkali cations, *e.g.* Li^+, into/from the host spinel phase of nano-$LiMn_2O_4$ in both organic $LiPF_6$/ethylene carbonate/dimethylene carbonate (EC/DMC) and aqueous Li_2SO_4 electrolytes.[138-140] Moreover, the double redox peaks from our ASCs are still well-defined even at a relative high scan rate of 100 mV s^{-1}, despite the increased peak separation with increasing scan rate due to polarization. Kaven *et al.* proposed that different potentials for specified superstructures of pseudocapacitive oxides exist upon the increasing Li^+ loading.[141] Zukalova *et al.* stated that the two potentials represent ion insertion into different facets of crystal structure.[142] The exact origin of these double peaks from our ASCs needs further separate investigation, but it is obvious that nanocrystalline or semi-amorphous electroactive oxides with unique morphology and surface have a significant influence on ionic diffusion into their subsurface and/or bulk solid phase. The enhanced sensitivity in full cell CV investigations compared to three-electrode systems is partially attributed to the fast kinetics that the CNT anode offers.[143] The nearly symmetric charge/discharge times in galvanostatic mode also indicate a rapid *I-V* response of our ASCs (data now shown here).

In this study, we were able to further differentiate the respective contribution of the pseudocapacitance and electric double-layer (EDL) capacitance to the overall electrochemical performance from ASCs for the first time. To do so, the concept of outer electroactive sites of metal oxides was introduced and the total C_s was partitioned into

pseudo- and EDL-capacitance.[144-145] This theory is rooted on the fact that the electrochemical kinetics of pseudocapacitive reactions is relatively blunt in contrast to ion adsorption and desorption at EDLs. In the partition process, the total voltammetric charge, q_T, is extrapolated from the dependence of q^{-1} on $v^{1/2}$ to when v is equal to zero, where v is the scan rate in mV s^{-1} (Figure 5.4B). On the other hand, the double-layer charge, q_{dl}, is estimated from the dependence of q on $v^{-1/2}$ when v is infinite (Figure 5.4C). Ultimately, the pseudocapacitance charge, q_{pseudo}, is obtained by subtracting the q_{dl} (95.113 C g^{-1} cm^{-2}) from q_T (329.707 C g^{-1} cm^{-2}). In our case, q_{pseudo} is equal to 234.594 C g^{-1} cm^{-2}, and therefore q_{pseudo}/q_{dl} = 2.5. Because of pseudocapacitive dominance, our ASCs deliver an outstanding C_s of 81.7 F g^{-1} at a scan rate of 2 mV s^{-1}.

As plotted in the Ragone diagram shown in Figure 5.4D, we confirmed that our ASCs of MnO$_2$-NFs//KCl//CNTs deliver both high energy density (E) and power density (P). As reference, the relevant values from previously reported MnO$_2$-based ASCs were also plotted. The maximum energy density of 45.4 Wh kg^{-1} (at a power density of 163.5 W kg^{-1}) and the maximum power density of 3107.7 W kg^{-1} (at an energy density of 17.3 Wh kg^{-1}) were achieved from our ASCs with an operating voltage of 2.0 V. These values are outstanding, not only much higher than those from pure MnO$_2$-based ECs using aqueous electrolytes,[77, 116-125, 132, 134, 146-148] but also higher than or comparable to those from ECs based on hybridized MnO$_2$/carbon nano-skeletons.[127, 149-150] More specifically, the delivered energy density of our MnO$_2$-NFs//KCl//CNTs ASCs is over 10 times larger than that of traditional EDLCs.[11] The electrochemical performance of our low-cost, green and safe ASCs using neutral aqueous electrolyte even does not fall behind of recently reported hybrid CNTs/Au/MnO$_2$//AC ECs in ionic liquid electrolyte with an operating

voltage range of 3.0 V (the maximum energy density of 67.5 Wh kg^{-1} at a power density of 593.8 W kg^{-1}).[151] Even the theoretical capacitance of Ni(OH)$_2$ (2,602.5 F g^{-1}) is approximately two times of that of manganese oxide-based materials, reported Ni(OH)$_2$//AC ASCs deliver a maximum energy density of 42.6 Wh kg^{-1} (at a power density of 110 W kg^{-1}) in a basic aqueous electrolyte with a limited potential window from 0.4 to 1.6 V.[152]

In addition, our MnO$_2$-NFs//KCl//CNTs ASCs also show excellent stability and reversibility over 20,000 cycles from galvanostatic testing at a current density of 2.0 A g^{-1}
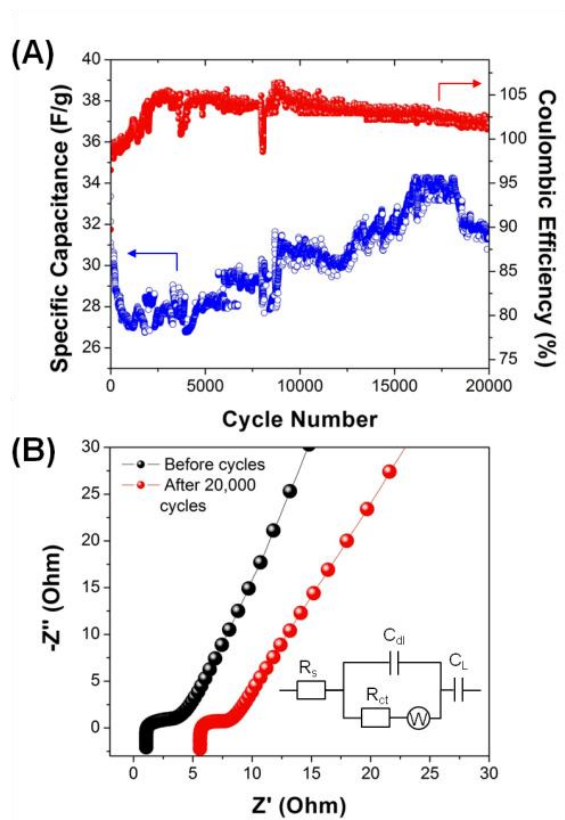
Figure 5.5 (A) Cycling performance of the assembled ASCs at a current density of 2.0 A g^{-1}. (B) Nyquist plots in the frequency range of 0.01 Hz to 10 kHz before and after 20,000 cycles, and the electrical equivalent circuit used to fit the impedance spectra.

between 0 to 2.0 V (Figure 5.5) Initially, a ~13% capacitance deterioration was observed in the first 2,000 cycles, which is probably owing to the irreversible K^+ intercalation into birnessite lattice. After that, the capacitance tends to increase gradually and even reached ~110.3% of the initial capacitance value of our ASCs, but it undergoes a partial capacitance loss in the last 2,000 cycles. This gradual buildup after the first 2,000 cycles instead of deterioration may be caused by the deep permeation of aqueous electrolyte into inner cavities of the electrodes. The coulombic efficiency fluctuates between 105% and 101% excluding the first 2,000 cycles. The superior cycling performance of our ASCs can also be attributed to the neutral aqueous electrolyte solution. In neutral solutions, the conversion between Mn^{3+}/Mn^{4+} is stable, and does not need the protection from the so-called SEI film as in organic electrolytes, where the Mn ions ceaselessly dissolve into solution with capacity fading.[153]

Nyquist plots were also analyzed using the Echem analysis software series (Gamry Instruments) on the basis of the equivalent circuit (Figure 5.5B). At high-frequency region, the intercept of EIS curve at the real axis (Z') represents the combined resistance (R_s) including contact resistance on the interface of electrode materials and current collector, ionic resistance of electrolyte and inherent resistance of current collector and the R_s underwent a small increase from 1.1 to 5.6 Ω after 20,000 cycles at a current density of 2.0 A g^{-1} between 0 to 2.0 V, which is probably due to the partial delamination of active materials from the current collectors. Furthermore, the semicircle at the medium-high region represents the charge transfer resistance (R_{ct}), which maintains at ~2.2 Ω for both impedance spectra taken before and after the 20,000 cycles. Since R_{ct} represents the resistance from both Faradic reactions and double-layer capacitance (C_{dl})

on electrode surface, the unchanged R_{ct} indicates that effective pseudocapacitive reactions occur in our ASCs without exterior and interior disturbance in accordance with the almost unaltered slopes of Warburg diffusion impedances (Z_w) at low-frequency region.

Based on the preceding structural and electrochemical analysis of our ASCs, their pseudocapacitive dominance, high energy and power densities, and superior cycling performance can all be attributed to the novel MnO_2-NF architecture and rational ASC design. First, the peculiar MnO_2-NFs assembled from ultrathin nanoflakes with several atomic layers create a non-dense stacking environment. The space amongst these MnO_2-NFs allows super easy and fast access of neutral KCl aqueous electrolyte into even deep cavities. The K^+ ions transport swiftly along grain boundaries of the MnO_2-NFs and into the open channels of the ultrathin sheets. These structural features significantly shorten the charge diffusion distance and advantageously facilitate pseudocapacitive reactions in general. At the meantime, during K^+ intercalation/deintercalation into/from the non-stoichiometric $K_{0.26}MnO_2$ NFs, the valence state change of Mn ions enriches the intermediate conversions between III and IV.[154] This occurs simultaneously with fast ionic diffusion due to the high potassium cationic distribution in the bulk phase of our MnO_2-NFs. It enables the spontaneous K^+ intercalation/deintercalation poccesses not solely happening right beneath the surface but the whole MnO_2-NF-based electrode.[130, 138] On the other hand, compared to commonly employed activated carbon with averaged pore size smaller than 5 Å and intensively stacked graphene layers, our selected CNTs possess enhanced kinetics to further improve fast pseudocapacitive reactions and overall capacitance.

5.4 Conclusion

In conclusion, we first developed a facile and green synthesis procedure in mild conditions to synthesize unique MnO_2 nanoflowers, *i.e.* ultrathin $K_{0.26}MnO_2$ nanoflake assemblies, with an average diameter of ~25 nm through a pyrrolidone ring-opening reaction between NMP and $KMnO_4$. Prototype MnO_2-NFs//KCl//CNTs ASC cells were easily fabricated using the as-synthesized MnO_2-NFs as cathode material coupled with CNTs as anode material in neutral aqueous KCl electrolyte. These prototype ASC devices allow rapid charge/discharge and ionic diffusion kinetics, fast ionic response, and evident pseudocapacitive dominance (q_{pseudo}/q_{dl} = 2.5) for the first time. More specifically, they delivered a maximum specific capacitance as high as 81.7 F g^{-1} and an exceptional energy density of 45.4 Wh kg^{-1} (at a power density of 163.5 W kg^{-1}). These ASCs possess excellent cycling performance without obvious capacitance deterioration after 20,000 cycles in a potential window of 2.0 V at a current density of 2.0 A g^{-1}. To sum, we believe that such low-cost and high-performance manganese oxide nanoflowers using earth-abundant and environmentally friendly materials and synthesized by a facile, scalable and green solution-based process can offer great potential in grid-scale energy storage device applications. Furthermore, our study provides a brilliant proof-of-concept design of novel supercapacitors with pseudocapacitive dominance to achieve ultimate energy storage applications with both high energy and power densities.

CHAPTER VI

INTERCONNECTED THREE-DIMENSIONAL CATERPILLAR ZNO NETWORKS:

PHOTOELECTROCHEMICAL ENHANCEMENT

6.1 Introduction

Since the pioneering demonstration of metal oxides as photoanodes applied in photoelectrochemical (PEC) water splitting in 1972,[155] considerable attention has been received to develop satisfactory photoanodes that harvest inexhaustible solar energy to generate sustainable hydrogen.[156-158] One dimensional (1-D) metal oxide, predominantly TiO_2,[159-162] ZnO,[163-166] α-Fe_2O_3,[167-170] $BiVO_4$[171-172] and WO_3,[173-175] nanostructures, such as nanowires (NWs), nanotubes (NTs) and nanorods (NRs), have been deemed to be tunable building blocks for future effective photovoltaic devices owing to their shortened lateral charge carrier diffusion length, monocrystal-induced high electron mobility, explicit control over structural uniformity and preferred crystallographic orientation. Especially, ZnO's ease of crystallization and structurally anisotropic extensions conduces to constructing high performance 1-D photoelectrodes. Indeed, the 1-D based photovoltaic devices evidently yielded higher solar-to-hydrogen conversion efficiency than those based on nanoparticles (0-D) due to the direct charge transport channels and the eliminated electron trapping at grain boundaries.[176-177]

However, the insufficient utilization of voids among 1-D arrays results in low surface areas, which severely restrains the light absorption capability. Therefore, a large surface area is desired

without losing the advantageous features of 1-D geometries and by this token structural hierarchy is contrived stepping toward essential multiscale complexity, *i.e.* branched NWs/NTs/NRs nanoconfigurations.[109, 178-180] Yang *et al.* synthesized comblike ZnO structures via high-temperature evaporation of metallic powder and condensation method [181]. Yan *et al.* used a two-step vapor-solid procedure to synthesize dendritic ZnO nanostructures at high temperatures.[182] Fan *et al.* recently reported three-dimensional (3-D) ZnO nanosuperstructure photoanodes using porous gold catalyst through chemical vapor deposition (CVD) but relatively low photocurrent density of 0.18 mA cm^{-2} at bias of 1.21 V *vs.* RHE was achieved.[183] However, besides extreme requisites like high temperature and/or noble metal catalysts, most synthetic strategies are observed unlikely to produce uniform secondary nanostructures with high density and/or high aspect ratio, two crucial factors to determine surface-to-volume ratio. In remarkable contrast to afore-mentioned methods, the solution-phase synthesis is considered as an effective bottom-up route to fabricate 3-D hierarchical nanostructures due to its low cost, low reaction temperature, environmental benignity and ease of scaling up.[184-185] In particular, Ko *et al.* obtained upstanding "tree-like" multigeneration hierarchical ZnO nanostructures with high surface-to-volume ratio by repeatedly growing subordinate NWs on as-prepared seeded trunks or even nanotrees.[109] However, still some disadvantageous engineering obstacles remain in this route: (1) uncontrollable growth of secondary NWs on each segment of the parental trunks compromises the light absorption ability; (2) multi-step seeding-growth-seeding processes are time/agent-consuming and contradict the ease of manufacturing; (3) superfluous seeds after spinning-coating/drop-casting processes would aggregate in the void space, thereby blocking the light penetration into deep cavities. So it will be highly appreciated if one facile, robust and time-efficient protocol of fabricating ZnO photoanodes consisting of 3-D hierarchical nanostructures

with nanoscale precision and dramatically promoted surface-to-volume ratio is actualized to address pre-existing questions and improve light conversion efficiency.

In this work, we establish a rational fabrication of 3-D hierarchical branched ZnO nanostructures (BZNs). First, the PVP/Zn(NO$_3$)$_2$ composite fibers were produced in a large scale using a novel FS technology and calcined at 500 ℃ to convert to ZnO nanofibers (NFs) serving as tridimensional nucleation sites air-sprayed onto ITO substrates. Subsequently, omnidirectional, highly-dense NWs with high aspect ratio radically burgeoned from as-prepared ZnO nanofiber seeds under mild hydrothermal conditions to weave an interconnected network with open cavities. The extremely high branch density benefits from the nanoconfinement effect that the protection from excess polymer "carrier" in forcespun precursor fibers brought into upon ZnO nucleation and growth. The elaborate branches with small diameter are vital to shorten the minority carrier diffusion lengths. Furthermore, the branch growth in a 360° fashion along axial direction of parental NFs leads to a high spatial occupancy of NWs in multiple directions in a given footprint and hence significantly increases the roughness factor. The relevant photoanodes consisting of BZNs with open structures can improve light capture, penetration and multi-reflection abilities. The major merit of this strategy is that the interconnected BZNs offer a rapid highway for the electron transport back to contact, realizing charge transfer in nanostructures across micrometer-scale distances. The aforementioned features, illustrated in Figure 6.1, are expected to reduce charge recombination and enhance the overall light-conversion efficiency, upon which various applications in energy storage and conversion can be developed by exploring the structural, optical and electronic properties of our herein identified hierarchical nanostructure system.

6.2 Experimental

6.2.1 Materials

Polyvinylpyrrolidone (PVP, Mw = 130 000, Sigma-Aldrich), zinc nitrate hexahydrate ($Zn(NO_3)_2.6H_2O$, reagent grade 98%, Sigma-Aldrich), hexamethylenetetramine ($C_6H_{12}N_4$, HMTA, $\geq$ 99%, Sigma-Aldrich), polyethylenimine (PEI, Mw = ~ 800, Sigma-Aldrich), ammonia ($NH_3.H_2O$, 28- 30%, Sigma-Aldrich) were used without any purification.

6.2.2 Preparation of 3-D ZnO nanostructures and relevant photoanodes

A typical 32 wt% polyvinylpyrrolidone (PVP, Mw = 130 000, Sigma-Aldrich) stock solution was prepared by dissolving 3.7 g PVP into 8.0 mL deionized water in a capped vial under magnetically stirring for 24 h, followed by a vortex mixing for 8 h for homogeneous dissolution. 1.5 g zinc nitrate hexahydrate ($Zn(NO_3)_2.6H_2O$, reagent grade 98%, Sigma-Aldrich) was added to the above PVP stock solution by vortex mixing, the viscous mixture of which was allowed to degas for 3h in vacuum for removing any trapped air-bubbles. An aliquot of the freshly prepared PVP/$Zn(NO_3)_2$ solution was fed into the reservoir of proprietary spinneret with 8 equally circumferentially spaced orifices equipped with 30 gauge stainless steel needles. Typical FS parameters were as follows: rotational speed was 9 000 rpm; needle-to-aluminum collector was 6 cm; Forcespinning duration was 1 min for each fiber collection. The as-spun PVP/$Zn(NO_3)_2$ composite fibers were then folded in the form of one-square-foot mat for further utilization.

The ZnO nanofibers that comprise ZnO spherical nanoseeds were synthesized by heating the as-spun PVP/$Zn(NO_3)_2$ composite fibers in air to 500 ℃, held isothermally for 3 h, at

a ramp rate of 2 ℃ min^{-1} to remove the carrier polymer. 2 g ZnO nanofiber powder was dispersed first in 10 mL of 1-butanol (≥ 99%, Sigma-Aldrich) to form a paste by sonicating for 5 min. Subsequently, the airbrush technique operated at spray pressure of 10 psi was employed to deposit the suspension paste onto 180 nm indium tin oxide (ITO)-coated glass substrates (MTI Co., ≤ 15 Ω square^{-1}) and the ZnO nanofiber-carried ITO substrates were dried in vacuum oven at 80 ℃ overnight and then heated at 350 ℃ for 10 min for stabilization. The deposition thickness was controlled to ~ 8 μm by spray duration. The branched ZnO nanostructures were grown using the hydrothermal method reported previously with further optimization.[109] In a typical growth, one ZnNF-carried ITO substrate was immersed in an aqueous nutrient solution containing 0.025 M zinc nitrate hexahydrate, 0.025 M hexamethylenetetramine ($C_6H_{12}N_4$, HMTA, ≥ 99%, Sigma-Aldrich), 0.0035 M polyethylenimine (PEI, Mw = ~ 800, Sigma-Aldrich), and 0.1 M ammonia ($NH_3.H_2O$, 28-30%, Sigma-Aldrich) at 90 ℃ for 5 h with the back side of ITO substrate uppermost to grow secondary branches originating from nanofiber seeds. These photoelectrodes after branch growth were thoroughly rinsed with deionized water and ethanol, dried in vacuum oven, and then annealed in air at 350 ℃ for 10 min to remove the residual HMTA and PEI polymers. The preparation of vertical ZnO NW array being ~ 10 μm in height as reference for comparison was described in detail in our previous work.[129]

6.2.3 Characterization

The morphologies of samples were characterized using a Field-emission scanning electron microscopy (FESEM, Carl Zeiss Sigma VP, equipped with back-scatter electron detector). The images/patterns of transmission electron microscopy (TEM), high resolution TEM (HRTEM) TEM and selected area electron diffraction (SAED) were recorded on an Hitachi H-

9500 microscope with an accelerating voltage of 300 kV. A Dimension 3000 atomic force microscopy (AFM) with the nanoscope analysis software was used to measure mean roughness factors (R_a) on a scan projected area of 25×25 μm with a frequency of 0.3 Hz. The crystal structural information were determined using powder X-ray diffraction (XRD) (Bruker AXS D8 QUEST diffractometer with Cu Kα radiation ($\lambda = 1.5406$ Å)) and the Fourier transform infrared (FTIR) spectra were recorded from 4000 to 450 cm^{-1} with a 4 cm^{-1} spectral resolution on a Thermal Nicolet Nexus 470 spectrometer with a DTGS detector by signal averaging 32 scans. Thermogravimetic Analysis (TGA) and differential scanning calorimetry (DSC) were run between 25 ℃ and 600 ℃ at a heating rate of 10 ℃ min^{-1} on TA Instruments Q500 TGA and Q10 DSC in air, respectively, towards precursor fibers.

6.2.4 Photoelectrochemical Evaluation

PEC measurements for water splitting were performed in a standard three-electrode cell configuration using the as-prepared BZN photoanodes (deposition area of 1 cm^{-2}) as the working electrode, a platinum wire as the counter electrode, Ag/AgCl in 1 M saturated KCl as the reference electrode and 0.5 M Na_2SO_4 solution buffered to pH ~7.0 with 0.1 M potassium phosphate buffer solution as the electrolyte purged with N_2 for 10 min in advance. The current density versus voltage (*J-V*) responses were conducted on Gamry reference 600 Potentiostat/Galvanostat/ZRA workstation under AM 1.5 G illumination from a solar simulator (1 sun, 100 mV cm^{-2}, Iwasaki Solar Simulation Evaluation Systems equipped with EYE/Iwasaki electronic ballast system and infrared filters). The light fixture was built with four metal halide-based arc lamps in the form of 2×2 array to ensure the light uniformity and the setup matches the solar spectrum within 5 % error and is specified as IEC 60904-9 Class A standard (+/-2 %).
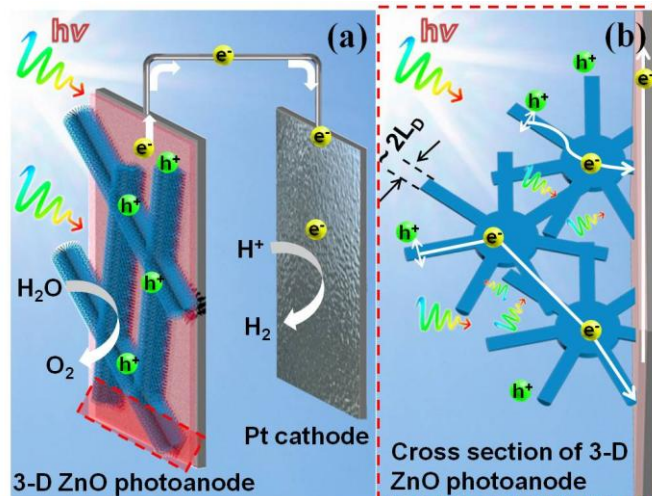
Figure 6.1 Schematic illustrations of (A) PEC water splitting setup and (B) the cross section of the BZN photoanode from the area outlined by the red rectangle in panel a, demonstrating the PEC reactions with rapid electron transport, improved light-harvesting and electron-hole dissociation.

6.3 Results and Discussion

6.3.1 Morphology and Structure Characterization

The crystal phase information of the $PVP/Zn(NO_3)_2$ precursor fibers and as-annealed ZnO NFs before and after hydrothermal growth of secondary branches was characterized by XRD analysis, as shown in Figure 6.2. It can be seen that the broad diffraction peak of the amorphous PVP ($2\theta = \sim 21.7°$) could be identified in the $PVP/Zn(NO_3)_2$ precursor fibers (Figure 6.2a).[186] After the calcination at 500 ℃ and subsequent branch growth, the XRD studies suggest that all the characteristic peaks conformed to the hexagonal wurtzite ZnO (JCPDS Card No. 36-

1451) with no any impurity (Figure 6.2b, c).[187] The measurement regarding the ZnO NFs suggested a Scherrer particle size of ~ 10 nm in diameter. These elaborate nanocrystals would
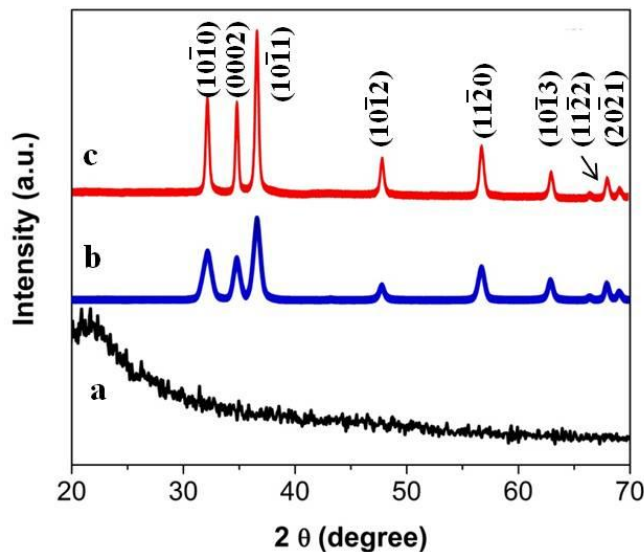
Figure 6.2 XRD patterns of (a) as-forcespun PVP/Zn(NO$_3$)$_2$ precursor fibers, (b) ZnO NFs and

(c) BZNs.

serve as numerous nucleation sites to lower thermodynamic barrier and consequently resulted in the further growth of highly-dense NW branches with high aspect ratio.[188]

The SEM images shown in Figure 6.3 reveal that highly-dense secondary branches can readily burgeon from the corresponding parental ZnO NF seeds prepared through FS technology followed by calcination and the schematic illustration depicts the formation process of the 3-D hierarchically-branched ZnO nanostructures. Figure 6.3a, b present SEM images of the PVP/Zn(NO$_3$)$_2$ composite fibers spun from a viscous Zn (II)-containing PVP solution heavily loaded with "carrier" polymer, *i.e.* water/PVP ratio = 1:0.47. The continuous composite fibers have smooth surface and an average diameter of ~ 800 nm and are randomly oriented. Specific to

FS process, the high-speed rotational force (9,000 rpm) drove the viscous fluid through orifices regardless of the tedious controlling parameters influencing Taylor cone and jet instability,
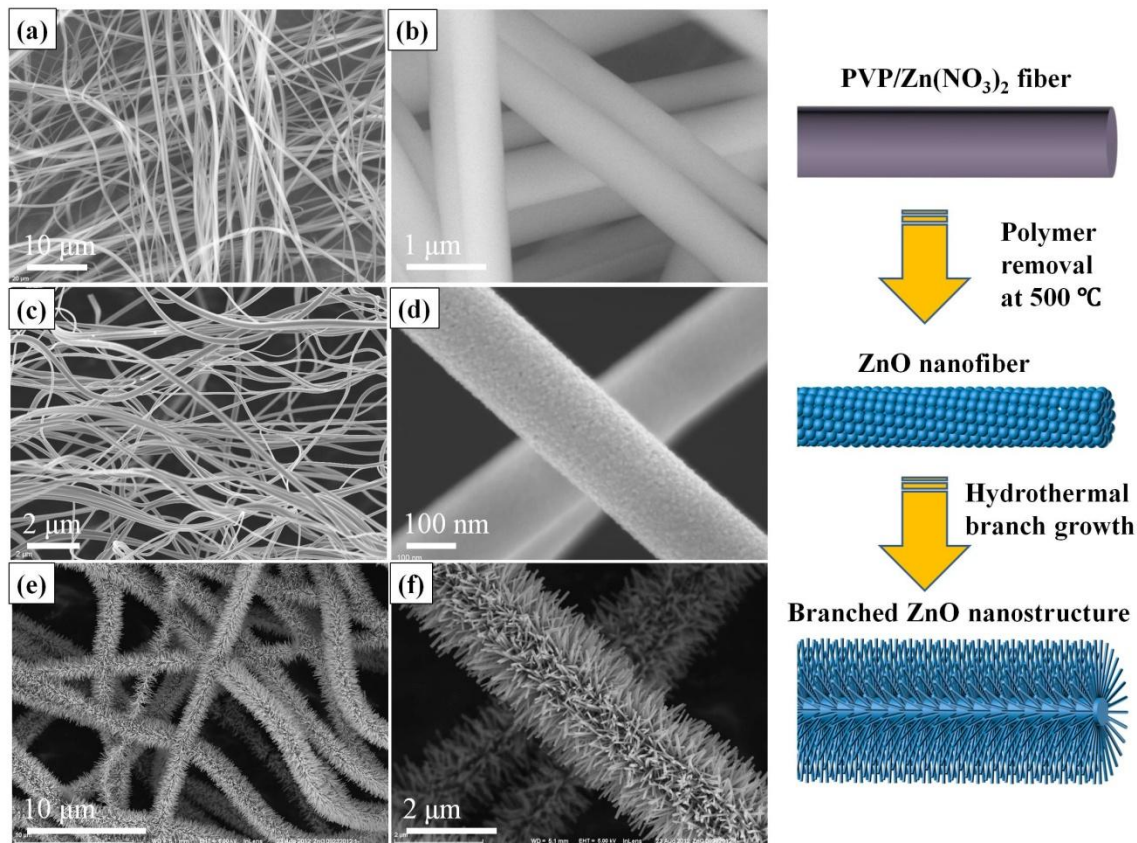
Figure 6.3 Low- and high magnification SEM images of (a, b) as-forcespun $PVP/Zn(NO_3)_2$ precursor fibers, (c, d) ZnO NFs and (e, f) BZNs. Schematic illustration of the BZNs' growth process is shown on the right column.

provided that the centrifugal force and hydrostatic pressure exceeded the capillary force.[45, 59, 189-190] The production rate for the $PVP/Zn(NO_3)_2$ composite fibers was measured to be ~ 0.68 g min^{-1} on a lab scale setup. Besides the unique capability to fulfill manufacturing demands, the FS technique was deliberately utilized to enrich polymer matrix. Figure 6.3c, d exhibit the ZnO NFs after calcination at 500 ℃ for 3 h. The ZnO NFs underwent an apparent shrinkage of diameter to

~ 200 nm because of the removal of PVP matrix and manifested ~ 10 nm ZnO nanocrystal aggregation in nanofiber form, consistent with the XRD results. Essentially grown were the matured ZnO NW branches by immersing the parental ZnO NFs in a nutrient growth solution
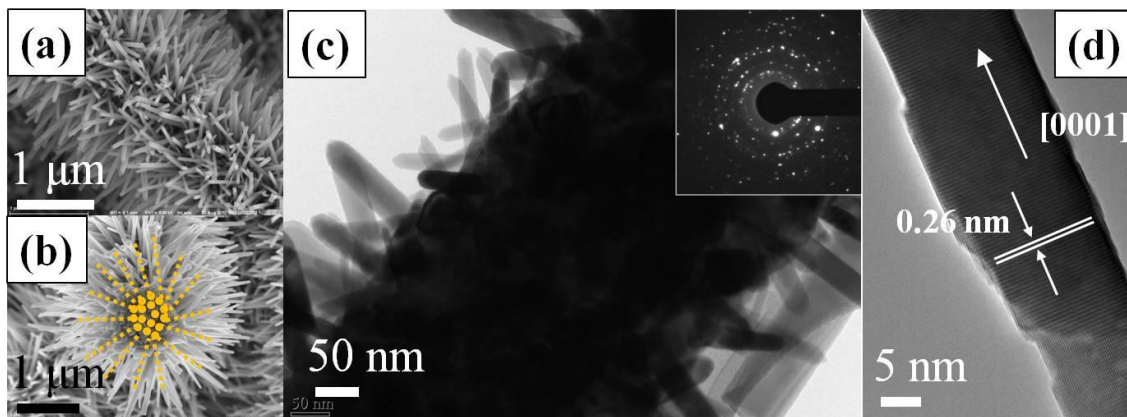
Figure 6.4 SEM images of (a) top view and (b) transverse view of one individual BZN. (c) Typical TEM image of one individual BZN. The inset in panel c shows SAED pattern. (d) HRTEM image of one NW branch laterally grown out of its parental ZnO NF.

described in detail in experimental section. As we expected, highly dense secondary branches with diameters of 30-50 nm and lengths of 600-800 nm laterally originated from the as-obtained ZnO NFs without applying additional seeding steps (figure 6.3e). The hierarchical structures maintained intact and their branch density is estimated as high as ~ 1.6×10^{12} NWs cm^{-2}. A typical image of such individual BZN shown in Figure 6.3f indicates that the secondary NW branches uniformly grew along a 360° path around the entire axial length of the pristine NFs, forming a supernanostructure resembling the hairy caterpillars, which greatly increase the surface area for more light harvesting.

The different regions of individual BZN were emphasized using SEM (Figure 6.4a, b). The transversely broken structure further verifies that the secondary ZnO NWs branched out of

the nanofiber seeds. The crystal structure was examined using TEM and HRTEM analysis. The TEM image in Figure 6.4c shows a portion of the BZN and the inset shows a SAED pattern taken from Figure 6.4c, signifying a polycrystalline buildup indexed for the hexagonal wurtzite ZnO and different alignments of the secondary branches. The HRTEM image in Figure 3d indicates that the secondary branches are highly crystallized with a lattice spacing of 0.26 nm, ascribed to the (0002) planes, and grow along the [0001] direction based on the fact that it is parallel to the long-axis direction of the NWs.[129, 188]

In order to clarify the formation of the extremely dense ZnO secondary branches. The FTIR and TGA/DSC measurements were carried out (Figure 6.5). In IR curve regarding PVP/Zn(NO$_3$)$_2$ fibers (Figure 6.5a1), the sharp absorption peak at 1383 cm^{-1} belongs to N-O asymmetric stretching vibrations of NO^{3-} group.[63] The fingerprint absorption modes of PVP are evidently identified with prominent peaks at about 1277-1294, 1321, 1424-1468, 1500 cm^{-1} and 2916-2960 cm^{-1}, which are assigned to N-C stretching of N-CH$_2$, C-H$_2$ wagging, C-H$_2$ scissoring, N-C stretching of N-C=O, and symmetric C-H stretching, respectively.[64-65] The primary absorption mode at 1653 cm^{-1} related to the carbonyl group C=O stretching vibration of PVP is presumably superimposed with strong O-H bending vibration. However, after the heat treatment, the IR spectrum in Figure 6.5a2 exhibits a significant absorption peak at 450 cm^{-1}, which is assigned to Zn-O stretching vibration, and the previous characteristic peaks regarding nitrate and PVP disappear [191]. This apparently signifies the thorough degradations of nitrate and PVP matrix. The TGA/DSC measurements were performed on the as-spun PVP/Zn(NO$_3$)$_2$ composite sample in air atmosphere (Figure 6.5b). The calorimetric thermogram displays three well-resolved exothermic signals. The first peak centered at 322 ℃, corresponding to an energy release of 166.4 J g^{-1} and a weight loss of 19 wt%, can be attributed to the decomposition of

nitrate salt.[70] Moreover, the thermal degradation of PVP displays a two-step decay in accordance with our previous studies towards polymer composites.[189] The peak centered at 438 ℃ correlates with the weight loss with the onset of ~ 345 ℃ in TGA and corresponds to the breakage of
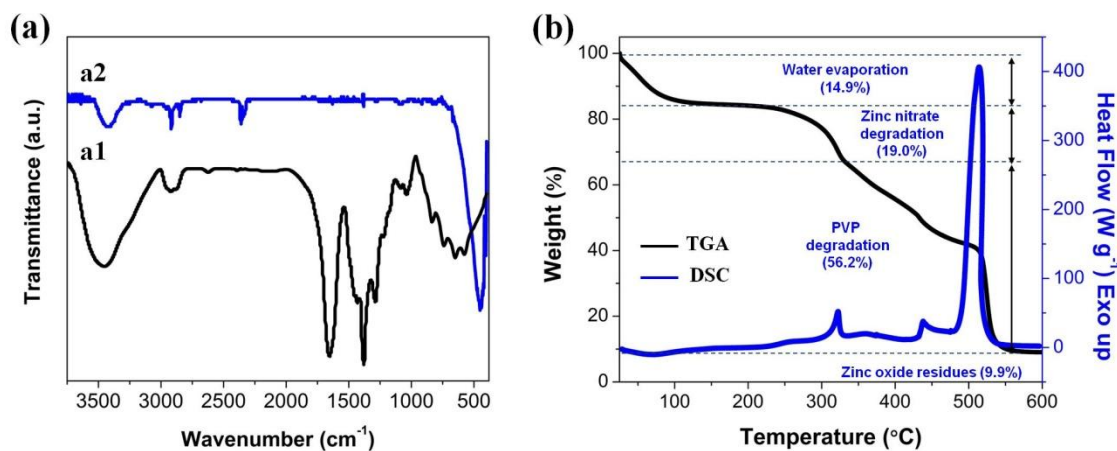
Figure 6.5 (a) FTIR spectra of (a1) as-forcespun PVP/Zn(NO₃)₂ precursor fibers and (a2) ZnO NFs. (b) TGA and DSC thermograms of as as-forcespun PVP/Zn(NO₃)₂ precursor fibers in air.

pyrrolidone pendant groups off the PVP backbones with an energy release of 45.9 J g^{-1}, while the remarkable exothermic peak located at 514 ℃ corresponding to an energy release of 3344 J g^{-1} is assigned to the degradation of the main hydrocarbon chains of PVP. The whole degradation of PVP stretching up to 557 ℃ in TGA curve reflects a weight drop of 56.2 wt%, leaving behind the ZnO NF residual of 9.9 wt%. Well-known is that the thermogram study can be interpreted to structural variations.[56] Particularly, the nitrate salt would decompose to ZnO nanoparticles prior to the degradation of PVP matrix so that the polymer skeleton can space-confine ZnO nanocrystals from upsizing upon nucleation and growth. Therefore, a heavy loading of "carrier" polymer in FS solution is desirable to invoke the nanoconfinement.[192] The ZnO nanocrystals as nuclei hydrothermally evolved to ultra-dense secondary NW branches with high aspect ratio by

taking in nutrients like Zn^{2+} from growth solution through bottom-up mechanism. Capping agent, PEI, played an important role in fostering an axial growth by selectively absorbing onto the side surface of ZnO NWs.[185, 193-194]
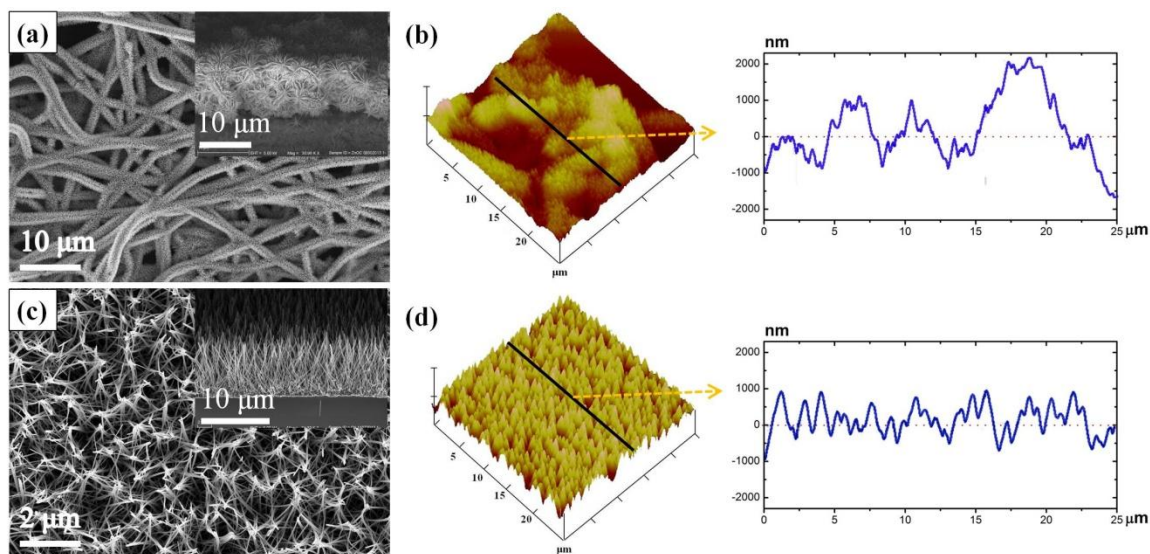
Figure 6.6 SEM and AFM images with the corresponding depth profile of the line of interest: (a, b) typical BZN photoanode (main panel, top view; inset, side view) and (c, d) vertically-aligned NW array photoanode.

The application of the BZNs was demonstrated as photoanode materials for solar assisted water splitting. To fabricate photoanodes that carry 3-D BZNs, the parental ZnO NFs' paste in 1-butanol was sprayed on ITO substrates using airbrush technique prior to growth of the secondary NW branches. The thermal stabilizations at 350 ℃ for 10 min were conducted on the photoanodes before and after branching as so to ensure an intimate attachment of our nanostructures on the substrates. This method avoids that repeated high temperature treatments on photoanodes for removal of polymer matrix deteriorated the electric conductivity owing to the size increase of ITO nanoparticles.[195] The BZN photoanode and the conventional vertically-

aligned ZnO NW array counterpart were studies through SEM and AFM characterizations (Figure 6.6). The SEM images reveal that the BZNs weave a mechanically and electrically robust network with open structures (Figure 6.6a). They interconnect with associative long branches and pile in a layer-by-layer form (~ 10 μm in thickness). In contrast to its vertical NW counterpart (Figure 6.6c), the secondary NWs of the BZNs are arranged polydirectionally and thus thoroughly occupy the void space among the parental backbones. The AFM results show that the mean roughness factor (R_a) of BZN photoanode is 926.64 nm, over 3 times higher than the R_a of 282.59 nm of the vertical NW counterpart, even though the mean roughness for the BZNs with multidirectionally distributed NWs is certainly underestimated, considering the multi-layer structure of the BZN photoanode and the AFM limitation of coarse acquisition aiming at non-Z axis complexity (Figure 6.6b, d).[196]

6.3.2 Photoelectrochemical Performance

Figure 6.7a shows the linear sweep voltammograms recorded from -0.5 to +1.2 V (*vs.* Ag/AgCl) on three typical ZnO nanostructures including the parental ZnO NFs, vertically-aligned NWs and BZNs under irradiation (100 mW cm^{-2}) as well as the BZNs in dark for comparison. The scan for the BZN electrode in the dark shows a negligible current density below 0.001 mA cm^{-2}. When illuminated under AM 1.5G simulated light, the parental ZnO NFs also produced a small photocurrent density of ~ 0.001 mA cm^{-2} from -0.5 to +1.0 V and 0.089 mA cm^{-2} at +1.2 V due to the limited surface area, invalid charge separation as well as the absence of electron transport paths. Significantly, the BZNs excelled others with its maximum current density of 0.524 mA cm^{-2} at +1.2 V (*vs.* Ag/AgCl), which is almost 151% higher than that of the ZnO NW arrays (0.348 mA cm^{-2}) tested at the same conditions. In addition, no saturation of photocurrent density was observed on our BZN electrode at the more positive potentials,

suggesting efficient charge separation and collection in those 3-D branched nanostructures under solar irradiation.
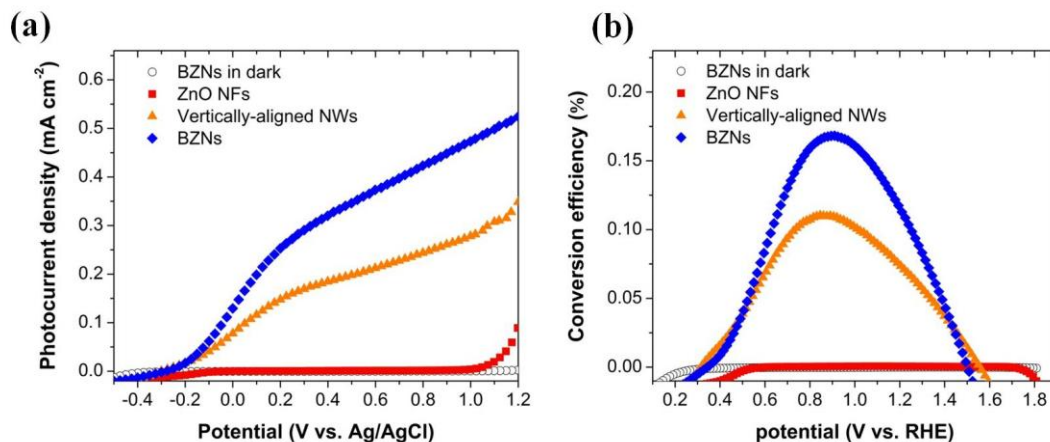
Figure 6.7 (a) *J-V* curves recorded at a scan rate of 10 mV s^{-1} under 1 sun illumination (100 mW cm^{-2} AM 1.5G), (b) Photoconversion efficiency (η) as a function of applied potential referenced to RHE.

The photoelectrochemical efficiencies (η) of all the photoanodes based on different ZnO nanostructures were evaluated via the equation:[156]

$$\eta(photo)\% = \frac{100J_p}{I_0}(E_{rev}^0 - |E_b|)$$

where j_p is the photocurrent density (mA cm^{-2}); E$^0_{rev}$ is the standard state-reversible potential (1.23 V for water splitting); P$_0$ is the incident light intensity (100 mW cm^{-2}); and the E_b is the applied bias potential, which is the difference between the bias potential at which j_p is measured and the bias potential at the open circuit under the same illumination intensity. The potential measured against Ag/AgCl is converted to reversible hydrogen electrode (RHE) using the equation E(RHE) = E(Ag/AgCl) + 0.1976 V + 0.0059 pH. As shown in Figure 6b, the

maximum efficiency for the BZNs is ~ 0.165% (at 0.89 V *vs.* RHE), 147% higher than 0.112% of the vertically-aligned NW counterpart (at 0.85 *vs.* RHE).

Some merits of constructing such hierarchically-branched ZnO nanostructures are responsible for the improvement of PEC efficiency. Firstly, the ultra-dense secondary NWs oriented in multi-directions caused a high spatial occupancy of the NWs, which greatly increased the surface-to-volume ratio and roughness factor and thus helped capture more sunlight. Secondly, the non-woven network consisting of the BZNs possessed an open structure prone to benefit the light penetration and trap the light via multi-reflections. Additionally, the fine branches (30-50 nm in diameter) with high length-to-diameter aspect ratio could facilitate the charge separation and hole diffusion at the electrode/electrolyte interface. Most importantly, the improved electron migration reduced the charge recombination, while the extensive branches elongated and yielded a great number of joint sites. This indeed realized the charge transport in nanostructures across the micrometer-scale distances. Compared with previous synthetic methods, the ease of preparation, less environmental impact and superior structural features endow the BZNs a promising system for various electronic, optical and energy conversion applications. This work is devoted to replace traditional seeding methods conducted using spin-coating/drop-casting techniques. The bulk of our demonstration in this report is the rational fabrication of a structural model for PEC water splitting. The inherently large band gap of ZnO restricts the visible light absorption in solar spectrum in spite of a validated improvement of PEC performances using our BZNs. Therefore, further improvement is envisaged by substitutional doping, noble metal coating and sensitizing.

6.4 Conclusion

In summary, we have reported a robust fabrication of 3-D hierarchically-branched ZnO nanostructures by hydrothermally branching out of the ZnO seed-aggregated nanofibers, serving as nucleation sites, which derived from the forcespun $PVP/Zn(NO_3)_2$ composite fibers. Such 3-D nanostructures weaved into an electrically interconnected network. Material chemistry was tuned to yield secondary branches with high length-to-diameter aspect ratio and the characteristic of the ultra-dense, omnidirectional branches allowed for a high spatial occupancy of nanowires. When performed as rationally constructed PEC photoanodes, the 3-D nanostructures could attain an improved photo-to-hydrogen conversion efficiency of 0.165% and a maximum photocurrent density of 0.524 mA cm^{-2} at +1.2 V (*vs.* Ag/AgCl) on account of the enhanced light-harvesting ability and the effective electron-hole separation.

CHAPTER VII

FUTURE ENDEAVORS

There are many more research investigations that plan to be carried out concerning developments of 1/3-D nanostrctures and excitation of pseudocapacitance domination that have great potentials to maximally activating intrinsic natures of pseudocapacitive transition metal oxides/hydroxides. We assume that the intercalating alkali ion quantity in interlayers of electroactive nanostructures may determine the pseudocapacitance domination levels and hence results in the promotions of specific capacitance and energy density. The controls of crystallographic orientations of crystal structures, such as birnessite and lepidocrocite, and electrochemical preintercalation of alkali ions will be adopted to tune pseudocapacitive activity in our group. We plan to introduce our materials in lithium-ion batteries and flexible/bendable electrochemical devices and investigate their electrochemical performance. Simultaneously, the 1/3-D nanostructures will continue being fabricated in order to resolve the negative influence of heavily loaded active materials on conducting substrates to mechanical integrity and effective electrolyte ion penetration and eventually improve the rate capacity performance with no kinetic limitation. The potentials of Forcespinning® technology in energy storage and conversion will be continuously exploited.

REFERENCES

1.   L. L. Zhang, and X. S. Zhao Carbon-Based Materials as Supercapacitor Electrodes, *Chem. Soc. Rev.,* **38**, 2520-2531 (2009).

2.   P. Simon, and Y. Gogotsi Materials for Electrochemical Capacitors, *Nature Materials,* **7**, 845-854 (2008).

3.   E. Frackowiak, and F. Beguin Carbon Materials for the Electrochemical Storage of Energy in Capacitors, *Carbon,* **39**, 937-950 (2001).

4.   J. Chmiola, G. Yushin, Y. Gogotsi, C. Portet, P. Simon, and P. L. Taberna Anomalous Increase in Carbon Capacitance at Pore Sizes Less than 1 Nanometer, *Science,* **313**, 1760-1763 (2006).

5.   M. Kaempgen, C. K. Chan, J. Ma, Y. Cui, and G. Gruner Printable Thin Film Supercapacitors Using Single-Walled Carbon Nanotubes, *Nano Lett.,* **9**, 1872-1876 (2009).

6.   M. D. Stoller, S. J. Park, Y. W. Zhu, J. H. An, and R. S. Ruoff Graphene-Based Ultracapacitors, *Nano Lett.,* **8**, 3498-3502 (2008).

7.   X. Y. Lang, A. Hirata, T. Fujita, and M. W. Chen Nanoporous Metal/Oxide Hybrid Electrodes for Electrochemical Supercapacitors, *Nat. Nanotechnol.,* **6**, 232-236 (2011).

8.   X. Zhao, L. L. Zhang, S. Murali, M. D. Stoller, Q. H. Zhang, Y. W. Zhu, and R. S. Ruoff Incorporation of Manganese Dioxide within Ultraporous Activated Graphene for High-Performance Electrochemical Capacitors, *ACS Nano,* **6**, 5404-5412 (2012).

9.   C. C. Hu, K. H. Chang, M. C. Lin, and Y. T. Wu Design and Tailoring of the Nanotubular Arrayed Architecture of Hydrous RuO_2 for Next Generation Supercapacitors, *Nano Lett.,* **6**, 2690-2695 (2006).

10.   R. B. Rakhi, W. Chen, D. Y. Cha, and H. N. Alshareef Substrate Dependent Self-Organization of Mesoporous Cobalt Oxide Nanowires with Remarkable Pseudocapacitance, *Nano Lett.,* **12**, 2559-2567 (2012).

11.   M. Winter, and R. J. Brodd What are batteries, fuel cells, and supercapacitors?, *Chem. Rev.,* **104**, 4245-4269 (2004).

12.   D. Bélanger, T. Brousse, and J. W. Long Manganese Oxides: Battery Materials Make the Leap to Electrochemical Capacitors, *Electrochem. Soc. Interface*, 49-52 (2008).

13.   Y. Dai, K. Wang, and J. Y. Xie From Spinel Mn_3O_4 to Layered Nanoarchitectures Using Electrochemical Cycling and the Distinctive Pseudocapacitive Behavior, *Appl. Phys. Lett.,* **90**, (2007).

14.   R. N. Reddy, and R. G. Reddy Sol-gel MnO_2 as An Electrode Material for Electrochemical Capacitors, *J. Power Sources,* **124**, 330-337 (2003).

15.   B. Saravanakumar, K. K. Purushothaman, and G. Muralidharan Interconnected V2O5 Nanoporous Network for High-Performance Supercapacitors, *ACS Appl. Mater. Inter.,* **4**, 4484-4490 (2012).

16.   L. Yang, S. Cheng, Y. Ding, X. B. Zhu, Z. L. Wang, and M. L. Liu Hierarchical Network Architectures of Carbon Fiber Paper Supported Cobalt Oxide Nanonet for High-Capacity Pseudocapacitors, *Nano Lett.,* **12**, 321-325 (2012).

17.   S. K. Meher, P. Justin, and G. R. Rao Microwave-Mediated Synthesis for Improved Morphology and Pseudocapacitance Performance of Nickel Oxide, *ACS Appl. Mater. Inter.,* **3**, 2063-2073 (2011).

18.   M. Yang, J. X. Li, H. H. Li, L. W. Su, J. P. Wei, and Z. Zhou Mesoporous slit-structured NiO for high-performance pseudocapacitors, *Phys. Chem. Chem. Phys.,* **14**, 11048-11052 (2012).

19.   Y. Y. Dan, H. B. Lin, X. L. Liu, H. Y. Lu, J. Z. Zhao, Z. Shi, and Y. P. Guo Porous Quasi Three-dimensional Nano-Mn_3O_4/PbO_2 Composite as Supercapacitor Electrode Material, *Electrochim. Acta,* **83**, 175-182 (2012).

20.   N. F. Yu, and L. J. Gao Electrodeposited PbO_2 Thin Film on Ti Electrode for Application in Hybrid Supercapacitor, *Electrochem. Commun.,* **11**, 220-222 (2009).

21.   G. Binitha, M. S. Soumya, A. A. Madhavan, P. Praveen, A. Balakrishnan, K. R. V. Subramanian, M. V. Reddy, S. V. Nair, A. S. Nair, and N. Sivakumar Electrospun Alpha-Fe_2O_3 Nanostructures for Supercapacitor Applications, *J. Mater. Chem. A,* **1**, 11698-11704 (2013).

22.   W. Tian, X. Wang, C. Y. Zhi, T. Y. Zhai, D. Q. Liu, C. Zhang, D. Golberg, and Y. Bando $Ni(OH)_2$ Nanosheet@Fe_2O_3 Nanowire Hybrid Composite Arrays for High-performance Supercapacitor Electrodes, *Nano Energy,* **2**, 754-763 (2013).

23. B. K. Balan, H. D. Chaudhari, U. K. Kharul, and S. Kurungot Carbon Nanofiber-RuO_2-Poly(benzimidazole) Ternary Hybrids for Improved Supercapacitor Performance, *RSC Adv.,* **3**, 2428-2436 (2013).

24. S. K. Mondal, and N. Munichandraiah Anodic Deposition of Porous RuO2 on Stainless Steel for Supercapacitor Studies at High Current Densities, *J. Power Sources,* **175**, 657-663 (2008).

25. X. B. Ren, H. Y. Lu, H. B. Lin, Y. N. Liu, and Y. Xing Preparation and Characterization of the $Ti/IrO_2/WO_3$ as Supercapacitor Electrode Materials, *Russ. J. Electrochem.,* **46**, 77-80 (2010).

26. Z. G. Ye, G. W. Liu, G. B. Huang, K. Wang, and G. J. Qiao Nano-Wedge IrO_2/MnO_2 Hybrid Film Electrode for Electrochemical Supercapacitors, *ECS Electrochem. Lett.,* **2**, A118-A120 (2013).

27. C. Jo, J. Hwang, H. Song, A. H. Dao, Y. T. Kim, S. H. Lee, S. W. Hong, S. Yoon, and J. Lee Block-Copolymer-Assisted One-Pot Synthesis of Ordered Mesoporous WO_{3-x}/Carbon Nanocomposites as High-Rate-Performance Electrodes for Pseudocapacitors, *Adv. Funct. Mater.,* **23**, 3747-3754 (2013).

28. K. H. Chang, C. C. Hu, C. M. Huang, Y. L. Liu, and C. I. Chang Microwave-assisted Hydrothermal Synthesis of Crystalline WO_3-WO_3.$5H_2O$ mixtures for pseudocapacitors of the asymmetric type, *J. Power Sources,* **196**, 2387-2392 (2011).

29. X. Xiao, T. P. Ding, L. Y. Yuan, Y. Q. Shen, Q. Zhong, X. H. Zhang, Y. Z. Cao, B. Hu, T. Zhai, L. Gong, J. Chen, Y. X. Tong, J. Zhou, and Z. L. Wang WO_{3-x}/MoO_{3-x} Core/Shell Nanowires on Carbon Fabric as an Anode for All-Solid-State Asymmetric Supercapacitors, *Adv. Energy Mater.,* **2**, 1328-1332 (2012).

30. S. R. Sivakkumar, J. M. Ko, D. Y. Kim, B. C. Kim, and G. G. Wallace Performance Evaluation of CNT/Polypyrrole/MnO_2 Composite Electrodes for Electrochemical Capacitors, *Electrochim. Acta,* **52**, 7377-7385 (2007).

31. Y. Wang, H. C. Zeng, and J. Y. Lee Highly Reversible Lithium Storage in Porous SnO_2 Nanotubes with Coaxially Grown Carbon Nanotube Overlayers, *Adv. Mater.,* **18**, 645-649 (2006).

32.   Y. Hou, Y. W. Cheng, T. Hobson, and J. Liu Design and Synthesis of Hierarchical MnO_2 Nanospheres/Carbon Nanotubes/Conducting Polymer Ternary Composite for High Performance Electrochemical Electrodes, *Nano Lett.,* **10**, 2727-2733 (2010).

33.   Z. B. Lei, F. H. Shi, and L. Lu Incorporation of MnO_2-Coated Carbon Nanotubes between Graphene Sheets as Supercapacitor Electrode, *ACS Appl. Mater. Inter.,* **4**, 1058-1064 (2012).

34.   C. G. Liu, Z. N. Yu, D. Neff, A. Zhamu, and B. Z. Jang Graphene-Based Supercapacitor with an Ultrahigh Energy Density, *Nano Lett.,* **10**, 4863-4868 (2010).

35.   L. B. Hu, W. Chen, X. Xie, N. A. Liu, Y. Yang, H. Wu, Y. Yao, M. Pasta, H. N. Alshareef, and Y. Cui Symmetrical MnO_2-Carbon Nanotube-Textile Nanostructures for Wearable Pseudocapacitors with High Mass Loading, *ACS Nano,* **5**, 8904-8913 (2011).

36.   Y. C. Chen, Y. K. Hsu, Y. G. Lin, Y. K. Lin, Y. Y. Horng, L. C. Chen, and K. H. Chen Highly Flexible Supercapacitors with Manganese Oxide Nanosheet/Carbon Cloth Electrode, *Electrochim. Acta,* **56**, 7124-7130 (2011).

37.   X. Xiao, T. Li, P. Yang, Y. Gao, H. Jin, W. Ni, W. Zhan, X. Zhang, Y. Cao, J. Zhong, L. Gong, W. C. Yen, W. Mai, J. Chen, K. Huo, Y. L. Chueh, Z. L. Wang, and J. Zhou Fiber-Based All-Solid-State Flexible Supercapacitors for Self-powered Systems, *ACS Nano,* **6**, 9200-6 (2012).

38.   L. Y. Yuan, X. H. Lu, X. Xiao, T. Zhai, J. J. Dai, F. C. Zhang, B. Hu, X. Wang, L. Gong, J. Chen, C. G. Hu, Y. X. Tong, J. Zhou, and Z. L. Wang Flexible Solid-State Supercapacitors Based on Carbon Nanoparticles/MnO_2 Nanorods Hybrid Structure, *ACS Nano,* **6**, 656-661 (2012).

39.   Z. B. Lei, N. Christov, and X. S. Zhao Intercalation of Mesoporous Carbon Spheres between Reduced Graphene Oxide Sheets for Preparing High-Rate Supercapacitor Electrodes, *Energ. Environ. Sci.,* **4**, 1866-1873 (2011).

40.   W. Wei, X. B. Huang, Y. M. Tao, K. Y. Chen, and X. Z. Tang Enhancement of the Electrocapacitive Performance of Manganese Dioxide by Introducing a Microporous Carbon Spheres Network, *Phys. Chem. Chem. Phys.,* **14**, 5966-5972 (2012).

41.   T. S. Arthur, D. J. Bates, N. Cirigliano, D. C. Johnson, P. Malati, J. M. Mosby, E. Perre, M. T. Rawls, A. L. Prieto, and B. Dunn Three-dimensional Electrodes and Battery Architectures, *MRS Bull.,* **36**, 523-531 (2011).

42.   S. B. Ma, K. W. Nam, W. S. Yoon, X. Q. Yang, K. Y. Ahn, K. H. Oh, and K. B. Kim Electrochemical Properties of Manganese Oxide Coated onto Carbon Nanotubes for Energy-Storage Applications, *J. Power Sources,* **178**, 483-489 (2008).

43.   R. Liu, J. Duay, and S. B. Lee Redox Exchange Induced MnO_2 Nanoparticle Enrichment in Poly(3,4-ethylenedioxythiophene) Nanowires for Electrochemical Energy Storage, *ACS Nano,* **4**, 4299-4307 (2010).

44.   G. L. Baker Progress toward Processable, Environmentally Stable Conducting Polymers, *Adv. Chem. Ser.*, 271-296 (1988).

45.   A. Altecor, Q. Li, K. Lozano, and Y. B. Mao Mixed-valent VO_x/polymer Nanohybrid Fibers for Flexible Energy Storage Materials *Ceramics International,* **40**, (2014).

46.   J. S. Lee, O. S. Kwon, S. J. Park, E. Y. Park, S. A. You, H. Yoon, and J. Jang Fabrication of Ultrafine Metal-Oxide-Decorated Carbon Nanofibers for DMMP Sensor Application, *ACS Nano,* **5**, 7992-8001 (2011).

47.   I. Capek Dispersions, Novel Nanomaterial Sensors and Nanoconjugates Based on Carbon Nanotubes, *Adv. Colloid. Interfac.,* **150**, 63-89 (2009).

48.   Y. Liang, Y. Li, H. Wang, and H. Dai Strongly Coupled Inorganic/Nanocarbon Hybrid Materials for Advanced Electrocatalysis, *J. Am. Chem. Soc.,* **135**, 2013-36 (2013).

49.   A. Jensen, J. R. Hauptmann, J. Nygard, J. Sadowski, and P. E. Lindelof Hybrid Devices from Single Wall Carbon Nanotubes Epitaxially Grown into a Semiconductor Heterostructure, *Nano Lett.,* **4**, 349-352 (2004).

50.   J. Duay, E. Gillette, R. Liu, and S. B. Lee Highly Flexible Pseudocapacitor Based on Freestanding Heterogeneous MnO_2/Conductive Polymer Nanowire Arrays, *Phys. Chem. Chem. Phys.,* **14**, 3329-3337 (2012).

51.   R. H. Baughman, A. A. Zakhidov, and W. A. de Heer Carbon Nanotubes - the Route toward Applications, *Science,* **297**, 787-792 (2002).

52.   Y. Y. Liang, M. G. Schwab, L. J. Zhi, E. Mugnaioli, U. Kolb, X. L. Feng, and K. Mullen Direct Access to Metal or Metal Oxide Nanocrystals Integrated with One-Dimensional Nanoporous Carbons for Electrochemical Energy Storage, *J. Am. Chem. Soc.,* **132**, 15030-15037 (2010).

53.   S. Boukhalfa, K. Evanoff, and G. Yushin Atomic Layer Deposition of Vanadium Oxide on Carbon Nanotubes for High-power Supercapacitor Electrodes, *Energ. Environ. Sci.,* **5**, 6872-6879 (2012).

54.   M. Sathiya, A. S. Prakash, K. Ramesha, J. M. Tarascon, and A. K. Shukla V_2O_5-Anchored Carbon Nanotubes for Enhanced Electrochemical Energy Storage, *J. Am. Chem. Soc.,* **133**, 16291-16299 (2011).

55.   W. Tang, X. W. Gao, Y. S. Zhu, Y. B. Yue, Y. Shi, Y. P. Wu, and K. Zhu A Hybrid of V_2O_5 Nanowires and MWCNTs Coated with Polypyrrole as An Anode Material for Aqueous Rechargeable Lithium Batteries with Excellent Cycling Performance, *J. Mater. Chem.,* **22**, 20143-20145 (2012).

56.   L. W. Ji, Z. Lin, M. Alcoutlabi, O. Toprakci, Y. F. Yao, G. J. Xu, S. L. Li, and X. W. Zhang Electrospun Carbon Nanofibers Decorated with Various Amounts of Electrochemically-Inert Nickel Nanoparticles for Use as High-Performance Energy Storage Materials, *RSC Adv.,* **2**, 192-198 (2012).

57.   S. R. Li, Y. Sun, S. Y. Ge, Y. Qiao, Y. M. Chen, I. Liebervvirth, Y. Yu, and C. H. Chen A Facile Route to Synthesize Nano-MnO/C Composites and Their Application in Lithium Ion Batteries, *Chem. Eng. J.,* **192**, 226-231 (2012).

58.   L. W. Ji, A. J. Medford, and X. W. Zhang Porous Carbon Nanofibers Loaded with Manganese Oxide Particles: Formation Mechanism and Electrochemical Performance as Energy-Storage Materials, *J. Mater. Chem.,* **19**, 5593-5601 (2009).

59.   K. Sarkar, C. Gomez, S. Zambrano, M. Ramirez, E. de Hoyos, H. Vasquez, and K. Lozano Electrospinning to Forcespinning (TM), *Mater. Today,* **13**, 12-14 (2010).

60.   K. Shanmuganathan, Y. C. Fang, D. Y. Chou, S. Sparks, J. Hibbert, and C. J. Ellison Solventless High Throughput Manufacturing of Poly(butylene terephthalate) Nanofibers, *ACS Macro. Lett.,* **1**, 960-964 (2012).

61.   Q. P. Pham, U. Sharma, and A. G. Mikos Electrospinning of Polymeric Nanofibers for Tissue Engineering Applications: A Review, *Tissue Eng.,* **12**, 1197-1211 (2006).

62.   J. M. Du, S. Shintay, and X. W. Zhang Diameter Control of Electrospun Polyacrylonitrile/Iron Acetylacetonate Ultrafine Nanofibers, *J. Polym. Sci. Pol. Phys.,* **46**, 1611-1618 (2008).

63.	O. Dag, O. Samarskaya, C. Tura, A. Gunay, and O. Celik Spectroscopic Investigation of Nitrate-Metal and Metal-Surfactant Interactions in the Solid $AgNO_3/C_{12}EO_{10}$ and Liquid-Crystalline $[M(H_2O)_n](NO_3)_2/C_{12}EO_{10}$ Systems, *Langmuir,* **19**, 3671-3676 (2003).

64.	J. Y. Xian, Q. Hua, Z. Q. Jiang, Y. S. Ma, and W. X. Huang Size-Dependent Interaction of the Poly(N-vinyl-2-pyrrolidone) Capping Ligand with Pd Nanocrystals, *Langmuir,* **28**, 6736-6741 (2012).

65.	M. A. Moharram, and M. G. Khafagi Application of FTIR Spectroscopy for Structural Characterization of Ternary Poly(acrylic acid)-Metal-Poly(vinyl pyrrolidone) Complexes, *J. Appl. Polym. Sci.,* **105**, 1888-1893 (2007).

66.	L. N. C. Rodrigues, M. G. Issa, A. C. C. Asbahr, M. A. C. Silva, and H. G. Ferraz Multicomponent Complex Formation between Pyrimethamine, Cyclodextrins and Water-soluble Polymers, *Braz. Arch. Biol. Techn.,* **54**, 965-972 (2011).

67.	G. Gaucher, K. Asahina, J. H. Wang, and J. C. Leroux Effect of Poly(N-vinyl-pyrrolidone)-block-poly(D,L-lactide) as Coating Agent on the Opsonization, Phagocytosis, and Pharmacokinetics of Biodegradable Nanoparticles, *Biomacromolecules,* **10**, 408-416 (2009).

68.	C. B. Jing, X. G. Xu, X. L. Zhang, Z. B. Liu, and J. H. Chu In Situ Synthesis and Third-Order Nonlinear Optical Properties of CdS/PVP Nanocomposite Films, *J. Phys. D. Appl. Phys.,* **42**, (2009).

69.	C. K. Chan, I. M. Chu, C. F. Ou, and Y. W. Lin Interfacial Interactions and their Influence to Phase Behavior in Poly(vinyl pyrrolidone)/Silica Hybrid Materials Prepared by Sol-gel Process, *Mater. Lett.,* **58**, 2243-2247 (2004).

70.	X. Chen, K. M. Unruh, C. Y. Ni, B. Ali, Z. C. Sun, Q. Lu, J. Deitzel, and J. Q. Xiao Fabrication, Formation Mechanism, and Magnetic Properties of Metal Oxide Nanotubes via Electrospinning and Thermal Treatment, *J. Phys. Chem. C,* **115**, 373-378 (2011).

71.	J. M. Kim, H. I. Joh, S. M. Jo, D. J. Ahn, H. Y. Ha, S. A. Hong, and S. K. Kim Preparation and Characterization of Pt Nanowire by Electrospinning Method for Methanol Oxidation, *Electrochim. Acta,* **55**, 4827-4835 (2010).

72.	K. X. Yao, and H. C. Zeng ZnO/PVP Nanocomposite Spheres with Two Hemispheres, *J. Phys. Chem. C,* **111**, 13301-13308 (2007).

73.	L. C. Mendes, R. C. Rodrigues, and E. P. Silva Thermal, Structural and Morphological Assessment of PVP/HA Composites, *J. Therm. Anal. Calorim.,* **101**, 899-905 (2010).

74. M. Mohl, D. Dobo, A. Kukovecz, Z. Konya, K. Kordas, J. Q. Wei, R. Vajtai, and P. M. Ajayan Formation of CuPd and CuPt Bimetallic Nanotubes by Galvanic Replacement Reaction, *J. Phys. Chem. C,* **115**, 9403-9409 (2011).

75. F. Xia, J. Brugger, Y. Ngothai, B. O'Neill, G. R. Chen, and A. Pring Three-Dimensional Ordered Arrays of Zeolite Nanocrystals with Uniform Size and Orientation by a Pseudomorphic Coupled Dissolution-Reprecipitation Replacement Route, *Cryst. Growth Des.,* **9**, 4902-4906 (2009).

76. L. W. Ji, O. Toprakci, M. Alcoutlabi, Y. F. Yao, Y. Li, S. Zhang, B. K. Guo, Z. Lin, and X. W. Zhang alpha-Fe_2O_3 Nanoparticle-Loaded Carbon Nanofibers as Stable and High-Capacity Anodes for Rechargeable Lithium-Ion Batteries, *ACS Appl. Mater. Inter.,* **4**, 2672-2679 (2012).

77. H. Jiang, C. Z. Li, T. Sun, and J. Ma A Green and High Energy Density Asymmetric Supercapacitor Based on Ultrathin MnO_2 Nanostructures and Functional Mesoporous Carbon Nanotube Electrodes, *Nanoscale,* **4**, 807-812 (2012).

78. Y. M. Sun, X. L. Hu, W. Luo, and Y. H. Huang Porous Carbon-Modified MnO Disks Prepared by a Microwave-Polyol Process and their Superior Lithium-ion Storage Properties, *J. Mater. Chem.,* **22**, 19190-19195 (2012).

79. J. X. Zhu, T. Sun, J. S. Chen, W. H. Shi, X. J. Zhang, X. W. Lou, S. Mhaisalkar, H. H. Hng, F. Boey, J. Ma, and Q. Y. Yan Controlled Synthesis of Sb Nanostructures and Their Conversion to $CoSb_3$ Nanoparticle Chains for Li-Ion Battery Electrodes, *Chemistry of Materials,* **22**, 5333-5339 (2010).

80. Z. Y. Wang, J. S. Chen, T. Zhu, S. Madhavi, and X. W. Lou One-pot Synthesis of Uniform Carbon-coated MoO_2 Nanospheres for High-rate Reversible Lithium Storage, *Chem. Commun.,* **46**, 6906-6908 (2010).

81. X. W. Li, D. Li, L. Qiao, X. H. Wang, X. L. Sun, P. Wang, and D. Y. He Interconnected Porous MnO Nanoflakes for High-Performance Lithium Ion Battery Anodes, *J. Mater. Chem.,* **22**, 9189-9194 (2012).

82. H. Xia, Y. S. Meng, X. G. Li, G. L. Yuan, and C. Cui Porous Manganese Oxide Generated from Lithiation/Delithiation with Improved Electrochemical Oxidation for Supercapacitors, *J. Mater. Chem.,* **21**, 15521-15526 (2011).

83. B. Messaoudi, S. Joiret, M. Keddam, and H. Takenouti Anodic Behaviour of Manganese in Alkaline Medium, *Electrochim. Acta,* **46**, 2487-2498 (2001).

84.   B. Djurfors, J. N. Broughton, M. J. Brett, and D. G. Ivey Electrochemical Oxidation of Mn/MnO Films: Formation of an Electrochemical Capacitor, *Acta Mater.,* **53**, 957-965 (2005).

85.   B. Djurfors, J. N. Broughton, M. J. Brett, and D. G. Ivey Electrochemical Oxidation of Mn/MnO Films: Mechanism of Porous Film Growth, *J. Electrochem. Soc.,* **153**, A64-A68 (2006).

86.   D. P. Dubal, D. S. Dhawale, R. R. Salunkhe, and C. D. Lokhande A Novel Chemical Synthesis of Mn_3O_4 Thin Film and its Stepwise Conversion into Birnessite MnO_2 during Super Capacitive Studies, *J. Electroanal. Chem.,* **647**, 60-65 (2010).

87.   C. W. Huang, and H. S. Teng Influence of Carbon Nanotube Grafting on the Impedance Behavior of Activated Carbon Capacitors, *J. Electrochem. Soc.,* **155**, A739-A744 (2008).

88.   M. F. El-Kady, V. Strong, S. Dubin, and R. B. Kaner Laser Scribing of High-Performance and Flexible Graphene-Based Electrochemical Capacitors, *Science,* **335**, 1326-1330 (2012).

89.   B. Liu, J. Zhang, X. F. Wang, G. Chen, D. Chen, C. W. Zhou, and G. Z. Shen Hierarchical Three-Dimensional $ZnCo_2O_4$ Nanowire Arrays/Carbon Cloth Anodes for a Novel Class of High-Performance Flexible Lithium-Ion Batteries, *Nano Lett.,* **12**, 3005-3011 (2012).

90.   H. Gwon, H. S. Kim, K. U. Lee, D. H. Seo, Y. C. Park, Y. S. Lee, B. T. Ahn, and K. Kang Flexible Energy Storage Devices Based on Graphene Paper, *Energ. Environ. Sci.,* **4**, 1277-1283 (2011).

91.   B. Liu, X. F. Wang, H. T. Chen, Z. R. Wang, D. Chen, Y. B. Cheng, C. W. Zhou, and G. Z. Shen Hierarchical Silicon Nanowires-Carbon Textiles Matrix as a Binder-free Anode for High-Performance Advanced Lithium-ion Batteries, *Sci. Rep.,* **3**, (2013).

92.   P. C. Chen, G. Z. Shen, Y. Shi, H. T. Chen, and C. W. Zhou Preparation and Characterization of Flexible Asymmetric Supercapacitors Based on Transition-Metal-Oxide Nanowire/Single-Walled Carbon Nanotube Hybrid Thin-Film Electrodes, *ACS Nano,* **4**, 4403-4411 (2010).

93.   M. L. Terranova, V. Sessa, and M. Rossi The world of carbon nanotubes: An Overview of CVD Growth Methodologies, *Chem. Vapor Depos.,* **12**, 315-325 (2006).

94.   H. H. Cheng, Z. L. Dong, C. G. Hu, Y. Zhao, Y. Hu, L. T. Qu, N. Chena, and L. M. Dai Textile Electrodes Woven by Carbon Nanotube-graphene Hybrid Fibers for Flexible Electrochemical Capacitors, *Nanoscale,* **5**, 3428-3434 (2013).

95.   L. Q. Mai, L. Xu, C. H. Han, X. Xu, Y. Z. Luo, S. Y. Zhao, and Y. L. Zhao Electrospun Ultralong Hierarchical Vanadium Oxide Nanowires with High Performance for Lithium Ion Batteries, *Nano Lett.,* **10**, 4750-4755 (2010).

96.   A. Matsumoto, S. Ogawa, T. Matsuda, A. Ueda, H. Aota, T. Fujii, and H. Toridome Further Discussion on Correlation between Brittleness and Inhomogeneous Network Structure of Cross-Linked Resins Originating in Specific Polymerization Behavior of Triallyl Isocyanurate, *Macromolecules,* **41**, 7938-7945 (2008).

97.   Z. Kurban, A. Lovell, S. M. Bennington, D. W. K. Jenkins, K. R. Ryan, M. O. Jones, N. T. Skipper, and W. I. F. David A Solution Selection Model for Coaxial Electrospinning and Its Application to Nanostructured Hydrogen Storage Materials, *J. Phys. Chem. C,* **114**, 21201-21213 (2010).

98.   M. K. Song, S. Cheng, H. Y. Chen, W. T. Qin, K. W. Nam, S. C. Xu, X. Q. Yang, A. Bongiorno, J. Lee, J. M. Bai, T. A. Tyson, J. Cho, and M. L. Liu Anomalous Pseudocapacitive Behavior of a Nanostructured, Mixed-Valent Manganese Oxide Film for Electrical Energy Storage, *Nano Lett.,* **12**, 4416-4416 (2012).

99.   R. Ostermann, D. Li, Y. D. Yin, J. T. McCann, and Y. N. Xia V_2O_5 Nanorods on TiO_2 nanofibers: A New Class of Hierarchical Nanostructures Enabled by Electrospinning and Calcination, *Nano Lett.,* **6**, 1297-1302 (2006).

100.   H. Jiang, C. Z. Li, T. Sun, and J. Ma High-performance supercapacitor material based on $Ni(OH)_2$ Nanowire-MnO_2 Nanoflakes Core-Shell Nanostructures, *Chem. Commun.,* **48**, 2606-2608 (2012).

101.   S. Xin, Y. G. Guo, and L. J. Wan Nanocarbon Networks for Advanced Rechargeable Lithium Batteries, *Accounts Chem. Res.,* **45**, 1759-1769 (2012).

102.   J. Jiang, Y. Y. Li, J. P. Liu, X. T. Huang, C. Z. Yuan, and X. W. Lou Recent Advances in Metal Oxide-based Electrode Architecture Design for Electrochemical Energy Storage, *Adv. Mater.,* **24**, 5166-5180 (2012).

103.   L. Q. Mai, F. Yang, Y. L. Zhao, X. Xu, L. Xu, and Y. Z. Luo Hierarchical $MnMoO_4$/$CoMoO_4$ Heterostructured Nanowires with Enhanced Supercapacitor Performance, *Nat. Commun.,* **2**, (2011).

104.   H. G. Wei, X. R. Yan, S. J. Wu, Z. P. Luo, S. Y. Wei, and Z. H. Guo Electropolymerized Polyaniline Stabilized Tungsten Oxide Nanocomposite Films: Electrochromic Behavior and Electrochemical Energy Storage, *J. Phys. Chem. C,* **116**, 25052-25064 (2012).

105.   J. P. Liu, J. Jiang, C. W. Cheng, H. X. Li, J. X. Zhang, H. Gong, and H. J. Fan Co_3O_4 Nanowire@MnO_2 Ultrathin Nanosheet Core/Shell Arrays: A New Class of High-Performance Pseudocapacitive Materials, *Adv. Mater.,* **23**, 2076-2081 (2011).

106.   X. H. Xia, J. P. Tu, Y. Q. Zhang, X. L. Wang, C. D. Gu, X. B. Zhao, and H. J. Fan High-Quality Metal Oxide Core/Shell Nanowire Arrays on Conductive Substrates for Electrochemical Energy Storage, *ACS Nano,* **6**, 5531-5538 (2012).

107.   C. W. Cheng, and H. J. Fan Branched nanowires: Synthesis and Energy Applications, *Nano Today,* **7**, 327-343 (2012).

108.   H. Wu, M. Xu, Y. C. Wang, and G. F. Zheng Branched Co_3O_4/Fe_2O_3 Nanowires as High Capacity Lithium-ion Battery Anodes, *Nano Res.,* **6**, 167-173 (2013).

109.   S. H. Ko, D. Lee, H. W. Kang, K. H. Nam, J. Y. Yeo, S. J. Hong, C. P. Grigoropoulos, and H. J. Sung Nanoforest of Hydrothermally Grown Hierarchical ZnO Nanowires for a High Efficiency Dye-Sensitized Solar Cell, *Nano Lett.,* **11**, 666-671 (2011).

110.   L. H. Bao, J. F. Zang, and X. D. Li Flexible Zn_2SnO_4/MnO_2 Core/Shell Nanocable-Carbon Microfiber Hybrid Composites for High-Performance Supercapacitor Electrodes, *Nano Lett.,* **11**, 1215-1220 (2011).

111.   J. G. Wang, Y. Yang, Z. H. Huang, and F. Y. Kang Rational Synthesis of MnO_2/Conducting Polypyrrole@Carbon Nanofiber Triaxial Nano-cables for High-performance Supercapacitors, *J. Mater. Chem.,* **22**, 16943-16949 (2012).

112.   G. H. Yu, L. B. Hu, M. Vosgueritchian, H. L. Wang, X. Xie, J. R. McDonough, X. Cui, Y. Cui, and Z. N. Bao Solution-Processed Graphene/MnO_2 Nanostructured Textiles for High-Performance Electrochemical Capacitors, *Nano Lett.,* **11**, 2905-2911 (2011).

113.   Z. G. Yang, J. L. Zhang, M. C. W. Kintner-Meyer, X. C. Lu, D. W. Choi, J. P. Lemmon, and J. Liu Electrochemical Energy Storage for Green Grid, *Chem. Rev.,* **111**, 3577-3613 (2011).

114.   X. J. Wang, Y. Y. Hou, Y. S. Zhu, Y. P. Wu, and R. Holze An Aqueous Rechargeable Lithium Battery Using Coated Li Metal as Anode, *Sci. Rep.,* **3**, (2013).

115.   J. M. Tarascon, and M. Armand Issues and Challenges Facing Rechargeable Lithium Batteries, *Nature,* **414**, 359-367 (2001).

116.   V. Khomenko, E. Raymundo-Pinero, and F. Beguin Optimisation of an Asymmetric Manganese Oxide/Activated Carbon Capacitor Working at 2 V in Aqueous Medium, *J. Power Sources,* **153**, 183-190 (2006).

117.   X. Zhang, P. Yu, H. T. Zhang, D. C. Zhang, X. Z. Sun, and Y. W. Ma Rapid Hydrothermal Synthesis of Hierarchical Nanostructures Assembled from Ultrathin Birnessite-Type MnO_2 Nanosheets for Supercapacitor Applications, *Electrochim. Acta,* **89**, 523-529 (2013).

118.   T. Cottineau, M. Toupin, T. Delahaye, T. Brousse, and D. Belanger Nanostructured Transition Metal Oxides for Aqueous Hybrid Electrochemical Supercapacitors, *Appl. Phys. a-Mater.,* **82**, 599-606 (2006).

119.   M. S. Hong, S. H. Lee, and S. W. Kim Use of KCl Aqueous Electrolyte for 2 V Manganese Oxide/Activated Carbon Hybrid Capacitor, *Electrochem. Solid St.,* **5**, A227-A230 (2002).

120.   T. Brousse, M. Toupin, and D. Belanger A Hybrid Activated Carbon-Manganese Dioxide Capacitor Using a Mild Aqueous Electrolyte, *J. Electrochem. Soc.,* **151**, A614-A622 (2004).

121.   T. Brousse, P. L. Taberna, O. Crosnier, R. Dugas, P. Guillemet, Y. Scudeller, Y. Zhou, F. Favier, D. Belanger, and P. Simon Long-term Cycling Behavior of Asymmetric Activated Carbon/MnO_2 Aqueous Electrochemical Supercapacitor, *J. Power Sources,* **173**, 633-641 (2007).

122.   Q. T. Qu, L. Li, S. Tian, W. L. Guo, Y. P. Wu, and R. Holze A cheap asymmetric supercapacitor with high energy at high power: Activated Carbon//$K_{0.27}MnO_2$ Center Dot $0.6H_2O$, *J. Power Sources,* **195**, 2789-2794 (2010).

123.   Q. T. Qu, Y. Shi, S. Tian, Y. H. Chen, Y. P. Wu, and R. Holze A New Cheap Asymmetric Aqueous Supercapacitor: Activated Carbon//$NaMnO_2$, *J. Power Sources,* **194**, 1222-1225 (2009).

124.   Y. T. Wang, A. H. Lu, H. L. Zhang, and W. C. Li Synthesis of Nanostructured Mesoporous Manganese Oxides with Three-Dimensional Frameworks and Their Application in Supercapacitors, *J. Phys. Chem. C,* **115**, 5413-5421 (2011).

125.   Q. T. Qu, P. Zhang, B. Wang, Y. H. Chen, S. Tian, Y. P. Wu, and R. Holze Electrochemical Performance of MnO_2 Nanorods in Neutral Aqueous Electrolytes as a Cathode for Asymmetric Supercapacitors, *J. Phys. Chem. C,* **113**, 14020-14027 (2009).

126.   Y. Jin, H. Chen, M. Chen, N. Liu, and Q. Li Graphene-Patched CNT/MnO2 Nanocomposite Papers for the Electrode of High-Performance Flexible Asymmetric Supercapacitors, *ACS Appl. Mater. Interfaces,* **5**, 3408-16 (2013).

127.   Y. L. Shao, H. Z. Wang, Q. H. Zhang, and Y. G. Li High-performance Flexible Asymmetric Supercapacitors Based on 3D Porous Graphene/MnO_2 Nanorod and Graphene/Ag Hybrid Thin-film Electrodes, *J Mater Chem C,* **1**, 1245-1251 (2013).

128.   J. Wang, J. Polleux, J. Lim, and B. Dunn Pseudocapacitive Contributions to Electrochemical Energy Storage in TiO_2 (Anatase) Nanoparticles, *J. Phys. Chem. C,* **111**, 14925-14931 (2007).

129.   X. Sun, Q. Li, Y. Lu, and Y. Mao Three-dimensional ZnO@MnO_2 Core@Shell Nanostructures for Electrochemical Energy Storage, *Chem. Commun.,* **49**, 4456-8 (2013).

130.   L. Mai, H. Li, Y. Zhao, L. Xu, X. Xu, Y. Luo, Z. Zhang, W. Ke, C. Niu, and Q. Zhang Fast Ionic Diffusion-enabled Nanoflake Electrode by Spontaneous Electrochemical Pre-Intercalation for High-performance Supercapacitor, *Sci. Rep.,* **3**, 1718 (2013).

131.   Y. K. Hsu, Y. C. Chen, Y. G. Lin, L. C. Chen, and K. H. Chen Reversible Phase Transformation of MnO_2 Nanosheets in an Electrochemical Capacitor Investigated by in-situ Raman Spectroscopy, *Chem. Commun.,* **47**, 1252-1254 (2011).

132.   M. Yeager, W. X. Du, R. Si, D. Su, N. Marinkovic, and X. W. Teng Highly Efficient $K_{0.15}MnO_2$ Birnessite Nanosheets for Stable Pseudocapacitive Cathodes, *J. Phys. Chem. C,* **116**, 20173-20181 (2012).

133.   W. Xiao, D. L. Wang, and X. W. Lou Shape-Controlled Synthesis of MnO_2 Nanostructures with Enhanced Electrocatalytic Activity for Oxygen Reduction, *J. Phys. Chem. C,* **114**, 1694-1700 (2010).

134.   H. C. Gao, F. Xiao, C. B. Ching, and H. W. Duan High-Performance Asymmetric Supercapacitor Based on Graphene Hydrogel and Nanostructured MnO_2, *ACS Appl. Mater. Inter.,* **4**, 2801-2810 (2012).

135.   C. S. Du, and N. Pan High Power Density Supercapacitor Electrodes of Carbon Nanotube Films by Electrophoretic Deposition, *Nanotechnology,* **17**, 5314-5318 (2006).

136.   J. Y. Cao, Y. M. Wang, Y. Zhou, J. H. Ouyang, D. C. Jia, and L. X. Guo High Voltage Asymmetric Supercapacitor Based on MnO_2 and Graphene Electrodes, *J. Electroanal. Chem.,* **689**, 201-206 (2013).

137.   L. Demarconnay, E. Raymundo-Pinero, and F. Beguin A Symmetric Carbon/Carbon Supercapacitor Operating at 1.6 V by Using a Neutral Aqueous Solution, *Electrochem. Commun.,* **12**, 1275-1278 (2010).

138.   W. Tang, Y. Hou, F. Wang, L. Liu, Y. Wu, and K. Zhu $LiMn_2O_4$ Nanotube as Cathode Material of Second-Level Charge Capability for Aqueous Rechargeable Batteries, *Nano Lett.,* **13**, 2036-40 (2013).

139.   G. Ceder, and B. Kang Response to "Unsupported Claims of Ultrafast Charging of Li-ion Batteries", *J. Power Sources,* **194**, 1024-1028 (2009).

140.   B. Kang, and G. Ceder Battery Materials for Ultrafast Charging and Discharging, *Nature,* **458**, 190-193 (2009).

141.   L. Kavan, J. Rathousky, M. Gratzel, V. Shklover, and A. Zukal Surfactant-templated TiO_2 (Anatase): Characteristic Features of Lithium Insertion Electrochemistry in Organized Nanostructures, *J. Phys. Chem. B,* **104**, 12012-12020 (2000).

142.   M. Zukalova, M. Kalbac, L. Kavan, I. Exnar, and M. Graetzel Pseudocapacitive Lithium Storage in TiO_2(B), *Chemistry of Materials,* **17**, 1248-1255 (2005).

143.   M. D. Stoller, and R. S. Ruoff Best Practice Methods for Determining an Electrode Material's Performance for Ultracapacitors, *Energ. Environ. Sci.,* **3**, 1294-1301 (2010).

144.   K. H. Chang, C. C. Hu, and C. Y. Chou Textural and Capacitive Characteristics of Hydrothermally Derived RuO_2 Center Dot xH_2O Nanocrystallites: Independent Control of Crystal Size and Water Content, *Chemistry of Materials,* **19**, 2112-2119 (2007).

145.   Y. H. Lee, K. H. Chang, and C. C. Hu Differentiate the Pseudocapacitance and Double-layer Capacitance Contributions for Nitrogen-doped Reduced Graphene Oxide in Acidic and Alkaline Electrolytes, *J. Power Sources,* **227**, 300-308 (2013).

146.   V. Khomenko, E. Raymundo-Pinero, E. Frackowiak, and F. Beguin High-voltage Asymmetric Supercapacitors Operating in Aqueous Electrolyte, *Appl. Phys. a-Mater.,* **82**, 567-573 (2006).

147.   Y. Wang, Y. Wang, E. Hosono, K. Wang, and H. Zhou The Design of a LiFePO4/Carbon Nanocomposite With a Core-Shell Structure and Its Synthesis by an In Situ Polymerization Restriction Method, *Angewandte Chemie International Edition,* **47**, 7461-7465 (2008).

148.   J. Cao, Y. Wang, Y. Zhou, J.-H. Ouyang, D. Jia, and L. Guo High Voltage Asymmetric Supercapacitor Based on MnO_2 and Graphene Electrodes, *J. Electroanal. Chem.,* **689**, 201-206 (2013).

149.   Z. S. Wu, W. C. Ren, D. W. Wang, F. Li, B. L. Liu, and H. M. Cheng High-Energy MnO_2 Nanowire/Graphene and Graphene Asymmetric Electrochemical Capacitors, *ACS Nano,* **4**, 5835-5842 (2010).

150.   Z. B. Lei, J. T. Zhang, and X. S. Zhao Ultrathin MnO_2 Nanofibers Grown on Graphitic Carbon Spheres as High-performance Asymmetric Supercapacitor Electrodes, *J. Mater. Chem.,* **22**, 153-160 (2012).

151.   X. Zhang, D. D. Zhao, Y. Q. Zhao, P. Y. Tang, Y. L. Shen, C. L. Xu, H. L. Li, and Y. Xiao High Performance Asymmetric Supercapacitor Based on MnO_2 Electrode in Ionic Liquid Electrolyte, *J. Mater. Chem. A,* **1**, 3706-3712 (2013).

152.   J. W. Lang, L. B. Kong, M. Liu, Y. C. Luo, and L. Kang Asymmetric Supercapacitors Based on Stabilized Alpha-$Ni(OH)_2$ and Activated Carbon, *J. Solid State Electr.,* **14**, 1533-1539 (2010).

153.   K. Fic, G. Lota, M. Meller, and E. Frackowiak Novel Insight into Neutral Medium as Electrolyte for High-voltage Supercapacitors, *Energ. Environ. Sci.,* **5**, 5842-5850 (2012).

154.   X. Zhao, M. V. Reddy, H. X. Liu, S. Ramakrishna, G. V. S. Rao, and B. V. R. Chowdari Nano $LiMn_2O_4$ with Spherical Morphology Synthesized by a Molten Salt Method as Cathodes for Lithium Ion Batteries, *RSC Adv.,* **2**, 7462-7469 (2012).

155.   A. Fujishima, and K. Honda Electrochemical Photolysis of Water at a Semiconductor Electrode, *Nature,* **238**, 37-8 (1972).

156.   M. G. Walter, E. L. Warren, J. R. McKone, S. W. Boettcher, Q. X. Mi, E. A. Santori, and N. S. Lewis Solar Water Splitting Cells, *Chem. Rev.,* **110**, 6446-6473 (2010).

157.   F. E. Osterloh Inorganic Nanostructures for Photoelectrochemical and Photocatalytic Water Splitting, *Chem. Soc. Rev.,* **42**, 2294-2320 (2013).

158.   N. S. Lewis Toward Cost-effective Solar Energy Use, *Science,* **315**, 798-801 (2007).

159.   M. Law, L. E. Greene, J. C. Johnson, R. Saykally, and P. D. Yang Nanowire Dye-sensitized Solar Cells, *Nature Materials,* **4**, 455-459 (2005).

160.   X. J. Feng, K. Shankar, O. K. Varghese, M. Paulose, T. J. Latempa, and C. A. Grimes Vertically Aligned Single Crystal TiO_2 Nanowire Arrays Grown Directly on Transparent

Conducting Oxide Coated Glass: Synthesis Details and Applications, *Nano Lett.,* **8**, 3781-3786 (2008).

161.   D. Lee, Y. Rho, F. I. Allen, A. M. Minor, S. H. Ko, and C. P. Grigoropoulos Synthesis of Hierarchical TiO$_2$ Nanowires with Densely-packed and Omnidirectional Branches, *Nanoscale,* **5**, 11147-11152 (2013).

162.   G. M. Wang, H. Y. Wang, Y. C. Ling, Y. C. Tang, X. Y. Yang, R. C. Fitzmorris, C. C. Wang, J. Z. Zhang, and Y. Li Hydrogen-Treated TiO$_2$ Nanowire Arrays for Photoelectrochemical Water Splitting, *Nano Lett.,* **11**, 3026-3033 (2011).

163.   X. Y. Yang, A. Wolcott, G. M. Wang, A. Sobo, R. C. Fitzmorris, F. Qian, J. Z. Zhang, and Y. Li Nitrogen-Doped ZnO Nanowire Arrays for Photoelectrochemical Water Splitting, *Nano Lett.,* **9**, 2331-2336 (2009).

164.   H. M. Chen, C. K. Chen, Y. C. Chang, C. W. Tsai, R. S. Liu, S. F. Hu, W. S. Chang, and K. H. Chen Quantum Dot Monolayer Sensitized ZnO Nanowire-Array Photoelectrodes: True Efficiency for Water Splitting, *Angew. Chem. Int. Edit.,* **49**, 5966-5969 (2010).

165.   H. M. Chen, C. K. Chen, C. C. Lin, R. S. Liu, H. Yang, W. S. Chang, K. H. Chen, T. S. Chan, J. F. Lee, and D. P. Tsai Multi-Bandgap-Sensitized ZnO Nanorod Photoelectrode Arrays for Water Splitting: An X-ray Absorption Spectroscopy Approach for the Electronic Evolution under Solar Illumination, *J. Phys. Chem. C,* **115**, 21971-21980 (2011).

166.   Y. F. Wei, L. Ke, J. H. Kong, H. Liu, Z. H. Jiao, X. H. Lu, H. J. Du, and X. W. Sun Enhanced Photoelectrochemical Water-splitting Effect with a Bent ZnO Nanorod Photoanode Decorated with Ag Nanoparticles, *Nanotechnology,* **23**, (2012).

167.   D. K. Bora, A. Braun, and E. C. Constable "In Rust We Trust". Hematite - the Prospective Inorganic Backbone for Artificial Photosynthesis, *Energ. Environ. Sci.,* **6**, 407-425 (2013).

168.   S. Agarwala, Z. H. Lim, E. Nicholson, and G. W. Ho Probing the Morphology-device Relation of Fe$_2$O$_3$ Nanostructures towards Photovoltaic and Sensing Applications, *Nanoscale,* **4**, 194-205 (2012).

169.   B. D. Chernomordik, H. B. Russell, U. Cvelbar, J. B. Jasinski, V. Kumar, T. Deutsch, and M. K. Sunkara Photoelectrochemical Activity of As-grown, Alpha-Fe$_2$O$_3$ Nanowire Array Electrodes for Water Splitting, *Nanotechnology,* **23**, (2012).

170.	J. T. Li, S. K. Cushing, P. Zheng, F. K. Meng, D. Chu, and N. Q. Wu Plasmon-induced Photonic and Energy-transfer Enhancement of Solar Water Splitting by a Hematite Nanorod Array, *Nat. Commun.,* **4**, (2013).

171.	J. Z. Su, L. J. Guo, S. Yoriya, and C. A. Grimes Aqueous Growth of Pyramidal-Shaped $BiVO_4$ Nanowire Arrays and Structural Characterization: Application to Photoelectrochemical Water Splitting, *Cryst. Growth Des.,* **10**, 856-861 (2010).

172.	L. Ren, L. Jin, J. B. Wang, F. Yang, M. Q. Qiu, and Y. Yu Template-free Synthesis of $BiVO_4$ Nanostructures: I. Nanotubes with Hexagonal Cross Sections by Oriented Attachment and their Photocatalytic Property for Water Splitting under Visible Light, *Nanotechnology,* **20**, (2009).

173.	J. Z. Su, X. J. Feng, J. D. Sloppy, L. J. Guo, and C. A. Grimes Vertically Aligned WO3 Nanowire Arrays Grown Directly on Transparent Conducting Oxide Coated Glass: Synthesis and Photoelectrochemical Properties, *Nano Lett.,* **11**, 203-208 (2011).

174.	X. L. Li, J. F. Liu, and Y. D. Li Large-scale Synthesis of Tungsten Oxide Nanowires with High Aspect Ratio, *Inorg. Chem.,* **42**, 921-924 (2003).

175.	V. Chakrapani, J. Thangala, and M. K. Sunkara WO_3 and W_2N Nanowire Arrays for Photoelectrochemical Hydrogen Production, *Int. J. Hydrogen Energ.,* **34**, 9050-9059 (2009).

176.	A. Wolcott, W. A. Smith, T. R. Kuykendall, Y. P. Zhao, and J. Z. Zhang Photoelectrochemical Study of Nanostructured ZnO Thin Films for Hydrogen Generation from Water Splitting, *Adv. Funct. Mater.,* **19**, 1849-1856 (2009).

177.	N. Beermann, L. Vayssieres, S. E. Lindquist, and A. Hagfeldt Photoelectrochemical Studies of Oriented Nanorod Thin Films of Hematite, *J. Electrochem. Soc.,* **147**, 2456-2461 (2000).

178.	I. S. Cho, Z. B. Chen, A. J. Forman, D. R. Kim, P. M. Rao, T. F. Jaramillo, and X. L. Zheng Branched TiO_2 Nanorods for Photoelectrochemical Hydrogen Production, *Nano Lett.,* **11**, 4978-4984 (2011).

179.	W. Q. Wu, B. X. Lei, H. S. Rao, Y. F. Xu, Y. F. Wang, C. Y. Su, and D. B. Kuang Hydrothermal Fabrication of Hierarchically Anatase TiO_2 Nanowire arrays on FTO Glass for Dye-sensitized Solar Cells, *Sci. Rep.,* **3**, (2013).

180.   G. X. Zhang, S. H. Sun, M. Cai, Y. Zhang, R. Y. Li, and X. L. Sun Porous Dendritic Platinum Nanotubes with Extremely High Activity and Stability for Oxygen Reduction Reaction, *Sci. Rep.,* **3**, (2013).

181.   H. Q. Yan, R. R. He, J. Johnson, M. Law, R. J. Saykally, and P. D. Yang Dendritic Nanowire Ultraviolet Laser Array, *J. Am. Chem. Soc.,* **125**, 4728-4729 (2003).

182.   R. F. Zhuo, H. T. Feng, J. T. Chen, D. Yan, J. J. Feng, H. J. Li, B. S. Geng, S. Cheng, X. Y. Xu, and P. X. Yan Multistep Synthesis, Growth Mechanism, Optical, and Microwave Absorption Properties of ZnO Dendritic Nanostructures, *J. Phys. Chem. C,* **112**, 11767-11775 (2008).

183.   C. Liu, X. B. Xu, A. J. E. Rettie, C. B. Mullins, and D. L. Fan One-step Waferscale Synthesis of 3-D ZnO Nanosuperstructures by Designed Catalysts for Substantial Improvement of Solar Water Oxidation Efficiency, *J. Mater. Chem. A,* **1**, 8111-8117 (2013).

184.   L. Manna, D. J. Milliron, A. Meisel, E. C. Scher, and A. P. Alivisatos Controlled Growth of Tetrapod-branched Inorganic Nanocrystals, *Nature Materials,* **2**, 382-385 (2003).

185.   T. L. Sounart, J. Liu, J. A. Voigt, M. Huo, E. D. Spoerke, and B. McKenzie Secondary Nucleation and Growth of ZnO, *J. Am. Chem. Soc.,* **129**, 15786-15793 (2007).

186.   Q. L. Ma, J. X. Wang, X. T. Dong, W. S. Yu, G. X. Liu, and J. Xu Electrospinning Preparation and Properties of Magnetic-photoluminescent Bifunctional Coaxial Nanofibers, *J. Mater. Chem.,* **22**, 14438-14442 (2012).

187.   Z. W. Pan, Z. R. Dai, and Z. L. Wang Nanobelts of Semiconducting Oxides, *Science,* **291**, 1947-1949 (2001).

188.   T. J. Athauda, J. G. Neff, L. Sutherlin, U. Butt, and R. R. Ozer Systematic Study of the Structure-Property Relationships of Branched Hierarchical TiO$_2$/ZnO Nanostructures, *ACS Appl. Mater. Inter.,* **4**, 6916-6925 (2012).

189.   Q. Li, K. Lozano, Y. N. Lü, and Y. B. Mao Heterogeneous Manganese Oxide-Encased Carbon Nanocomposite Fibers for High Performance Pseudocapacitors, *Ceramic Engineering and Science Proceedings* **34**, (2013).

190.   B. C. Weng, F. H. Xu, and K. Lozano Mass Production of Carbon Nanotube-reinforced Polyacrylonitrile Fine Composite Fibers, *J. Appl. Polym. Sci.*, (2014).

191.   S. Kumar, S. Basu, B. Rana, A. Barman, S. Chatterjee, S. N. Jha, D. Bhattacharyya, N. K. Sahoo, and A. K. Ghosh Structural, Optical and Magnetic Properties of Sol-gel Derived ZnO:Co

Diluted Magnetic Semiconductor Nanocrystals: an EXAFS Study, *J. Mater. Chem. C,* **2**, 481-495 (2014).

192.   G. Xia, D. Li, X. Chen, Y. Tan, Z. Tang, Z. Guo, H. Liu, Z. Liu, and X. Yu Carbon-Coated Li$_3$N Nanofibers for Advanced Hydrogen Storage, *Adv. Mater.,* **25**, 6238-44 (2013).

193.   L. Y. Chen, Y. T. Yin, C. H. Chen, and J. W. Chiou Influence of Polyethyleneimine and Ammonium on the Growth of ZnO Nanowires by Hydrothermal Method, *J Phys. Chem. C,* **115**, 20913-20919 (2011).

194.   K. S. Kim, H. Jeong, M. S. Jeong, and G. Y. Jung Polymer-Templated Hydrothermal Growth of Vertically Aligned Single-Crystal ZnO Nanorods and Morphological Transformations Using Structural Polarity, *Adv. Funct. Mater.,* **20**, 3055-3063 (2010).

195.   M. McCune, W. Zhang, and Y. L. Deng High Efficiency Dye-Sensitized Solar Cells Based on Three-Dimensional Multilayered ZnO Nanowire Arrays with "Caterpillarlike" Structure, *Nano Lett.,* **12**, 3656-3662 (2012).

196.   A. Sinno, P. Ruaux, L. Chassagne, S. Topcu, Y. Alayli, G. Lerondel, S. Blaize, A. Bruyant, and P. Royer Enlarged Atomic Force Microscopy Scanning Scope: Novel Sample-holder Device with Millimeter Range, *Rev. Sci. Instrum.,* **78**, (2007).

BIOGRAPHICAL SKETCH

Qiang Li, was born in 1984 in Qinhuangdao City, China. He obtained his high school degree from Bohai Private High School in 2003. Then he was granted the bachelor of engineering degree in Materials Science and Engineering department of the Nanjing University of Technology in 2007, where he had served as an undergraduate research assistant under the supervision of Dr. Zisheng Guan. He attempted to pursue overseas education in the US and he was accepted to the University of Texas-Pan American (UTPA) in 2012 in order for a master of engineering degree in Mechanical engineering. There he started to work as a graduate research assistant in Partnership for Research and Education in Materials (PREM) program while engaging in his research with Dr. Yuanbing Mao and Dr. Karen Lozano on the thesis topic, nanostructured transition metal oxides for energy storage and conversion. He finished his studies in May 2014.

His permanent address is:

Qiang Li

5-1-12 Jian'an Quarter

Nanhai West Road

Qinhuangdao City

Hebei Province

P.R.China